Microstructure Characterization of Hafnium-Modified Polymer-Derived SiOC and SiCN Ceramics

Vom Fachbereich Material- und Geowissenschaften der Technischen Universität Darmstadt zur Erlangung des Grades eines Doktors der Naturwissenschaften (Dr. rer. nat.) genehmigte Dissertation von Katharina Nonnenmacher, M. Sc., aus Berlin
Darmstadt 2016 (D 17)

TECHNISCHE UNIVERSITÄT DARMSTADT

Gutachter:	1. Prof. Dr. Hans-Joachim Kleebe
	2. Prof. Dr. Dr. h. c. Ralf Riedel
Tag der Einreichung	20. Juni 2016
Tag der Disputation	18. November 2016

Erklärung der Urheberschaft

Hiermit versichere ich, die vorliegende Arbeit ohne Hilfe Dritter und ohne Benutzung anderer als der angegebenen Hilfsmittel angefertigt zu haben. Die aus fremden Quellen direkt oder indirekt übernommenen Gedanken sind als solche kenntlich gemacht. Die Arbeit wurde bisher keiner anderen Prüfungsbehörde in gleicher oder ähnlicher Form vorgelegt.

Darmstadt, den 20. Juni 2016

Katharina Nonnenmacher

Table of Contents

1 Abstract / Zusammenfassung

To feature the development of innovative technologies and efficient usage of conventional energy sources, the application of advanced structural und functional ceramics is indispensable. In search of advanced ceramic materials with high thermo-mechanical performance for high temperature structural applications, research activities in Materials Science have explored thermolytic decomposition (pyrolysis) of organosilicon polymers as a novel process for the manufacturing of nanostructured silicon-based ceramic materials (polymer-derived ceramics, PDCs). Starting from synthetic polymeric organosilicon compounds, cross-linking and a subsequent annealing process, which leads to ceramization, yield the conversion into an amorphous silicon-based ceramic network. The underlying synthesis approach is a “bottom-up” approach which aims at linking organic components to inorganic structures. One of the key questions related to PDCs is whether nano- and microstructure can be tailored in order to achieve attractive structural and functional properties inaccessible by conventional powder-based sintered ceramics.

The motivation of the present work was to gather a thorough understanding of the thermal stability of polymer-derived hafnium-modified silicon oxycarbide (SiOC) and silicon carbonitride (SiCN) ceramics. Starting from as-received polymer-derived hafnium-modified SiOC- and SiCN-based ceramic nanocomposites, isothermal annealing experiments were carried out under the same conditions for both material systems. Upon annealing, the development of the local microstructure of both materials was investigated via conventional transmission electron microscopy (CTEM) in conjunction with energy-dispersive X-ray spectrometry (EDS) allowing for parallel microchemical analysis.

Placing particular emphasis on the local variation in average hafnia (HfO_2) crystallite size observed in a preliminary study using CTEM, gradual variations in average size were typically observed in close proximity to cracks and open pore channels in both materials and are shown to be related to an outward zoning to a carbon-depleted (and nitrogen-depleted) matrix composition.

In both materials, HfO_2 crystallite growth is time-dependent and proceeds via a coarsening process. The theory derived by Lifshitz, Slyozov and Wagner (LSW theory) for volume diffusion-controlled coarsening, which is based on thermodynamical considerations according to the Gibbs-Thomson equation, was

applied to the observed particle coarsening upon annealing in order to calculate the volume diffusion coefficient of hafnium in the host matrix. As it turned out, particle coarsening proceeds at a higher rate in close proximity to internal surfaces as compared to regions closer towards the bulk, which is typically a result of the increased hafnium volume diffusivity in the carbon-depleted (and nitrogen-depleted) matrix within the surface-near regions. As a general trend, in close proximity to internal surfaces, the volume diffusion coefficient of hafnium in the matrix is by three orders of magnitude larger as compared to values derived from regions closer towards the bulk. In the case of the SiOC-based material, bulk regions generally show a narrow particle size distribution of nano-sized HfO_2 precipitates. In contrast, HfO_2 precipitates were not observed via TEM, even at high resolution, in the bulk volume of the SiCN-based ceramic samples. Here, the local nitrogen content of the bulk matrix is assumed to be beyond a critical value, and may be dominant in determining HfO_2 precipitation since the ability of hafnium to diffuse through the SiCN matrix is diminished.

Furthermore, for gathering a better understanding of carbon transport in surface-near areas of the ceramic samples, diffusion modelling of measured carbon profiles using an analytical method was carried out for the SiOC-based system. Our modelling results suggest that carbon diffusion stagnates in surface-near areas after surface crystallization of cristobalite since it acts as a diffusion barrier for carbon, according to diffusion data reported in the literature.

This surface modification can also be applied to all other PDC material systems, considering their high-temperature stability, and is expected to lend inadequate overall thermo-mechanical and thermo-chemical properties to PDC materials.

Nanoskalige keramische Materialien mit geeigneten strukturellen und funktionalen Eigenschaften sind für den Einsatz in energie-effizienten Technologien unverzichtbar geworden. Molekularer Design mittels Silizium-basierter metallorganischer Vorstufen eröffnet den Zugang zu neuartigen amorphen Silizium-basierten Nichtoxid-Keramiken mit maßgeschneidertem nanoskaligem Aufbau. Über die so genannte bottom-up-Strategie werden spezifische molekulare Bausteine über Kondensations- und Polymerisationsvorgänge zu höheren molekularen Netzwerken und Festkörperstrukturen geordnet. Auf diese Weise können organische Komponenten

mit anorganischen Strukturen verknüpft werden, wodurch keramische Materialien entstehen, die durch pulvermetallurgische Sintertechniken nicht zugänglich sind.

Das Forschungsvorhaben der vorliegenden Arbeit gilt der Charakterisierung der Mikrostrukturen und lokalen Zusammensetzung von keramischen Hafnium-modifzierten Siliciumoxycarbid (SiOC) und Siliciumcarbonitrid (SiCN) Nanokompositen hinsichtlich ihrer Hochtemperaturstabilität, um deren Potential für den Einsatz in Hochtemperaturanwendungen bemessen zu können. Von Precursormaterial mit einer für beide Systeme jeweils festgelegten chemischen Zusammensetzung ausgehend wurden isothermale Auslagerungsversuche bei erhöhter Temperatur durchgeführt und der erreichte Grad an mikrostruktureller und chemischer Homogenität als Funktion der Zeit untersucht. Für beide Systeme erlaubt die Transmissionselektronenmikroskopie (TEM) mit integrierter energie-dispersiver Röntgenspektroskopie (EDS) die Beobachtung und quantitative Beschreibung einer graduellen Variation der Wachstumsrate der Sekundärphase Hafniumdioxid (HfO_2) als Funktion des lokalen Gehaltes an den leichten Matrixelementen Stickstoff (im Fall des SiCN-basierten Systems) und Kohlenstoff (im Fall beider Systeme) in oberflächennahen Probenbereichen (Probenoberflächen, Risse und offene Porenkanäle). Das Wachstumsverhalten der Sekundärphase bei erhöhter Temperatur kann mit einem diffusions-kontrollierten Vergröberungsmodel nach Lifshitz, Slyozov und Wagner (LSW-Theorie) beschrieben werden, mithilfe dessen der Diffusionskoeffizient von Hafnium in der Matrix berechnet werden konnte. Wie sich herausstellte, erhöht sich für beide untersuchten Systeme der Volumendiffusionskoeffizient von Hafnium in Bereichen mit niedrigen Gehalten an den leichten Matrixelementen Stickstoff und Kohlenstoff nahe Rissen und Porenkanälen um drei Größenordnungen relativ zu Probenbereichen mit höheren Gehalten an Kohlenstoff und Stickstoff in der Matrix.

Darüberhinaus zeigt das untersuchte HfO_2/SiHfCNO Nano-Kompositmaterial keine HfO_2 Ausscheidungen in Probenbereichen mit Sauerstoffgehalten in der Matrix unterhalb eines charakteristischen Schwellenwertes, was auf eine kinetische Hemmung der Ausscheidung durch Einbringung von Stickstoff bei gleichzeitiger Reduktion von Sauerstoff in der amorphen Glasmatrix zurückgeführt wird.

Um ein theoretisches Verständnis der beobachteten Kohlenstoffverarmung nahe inneren Oberflächen zu erhalten, wurden die für das System HfO_2/SiHfOC mittels EDS gemessenen Kohlenstoffprofile an ein klassisches Diffusionsmodel analytisch

angenähert und ein effektiver Diffusionskoeffizient der mobilen Kohlenstoffspezies berechnet. Der effektive Diffusionskoeffizient der Kohlenstoffspezies sinkt von einem bei kurzen Auslagerungszeiten relativ hohen Wert nach längerer Auslagerungszeit um mehrere Größenordnungen. Parallel zur beobachteten Verlangsamung der oberflächennahen Kohlenstoffdiffusion trit nahe den Oberflächen lokal die Bildung von Cristobalit in der Matrix über homogene Keimbildung auf. Literaturdaten belegen, dass Cristobalit als Diffusionsbarriere für Kohlenstoff wirkt. Die Bildung von Cristobalit in oberflächennahen Bereichen wird als Ursache für die verlangsamte Kohlenstoffdiffusion gesehen.

Die vorliegende Arbeit zeigt, dass keine adäquate Homogenität der Kompositmaterialien in oberflächennahen Bereichen erzeugt werden konnte, da die Matrixkonstituenten Stickstoff und Kohlenstoff mobile Spezies bilden. Aufgrund dieser Oberflächenmodifikation, die bereits nach der Pyrolyse vorhanden ist, sind insgesamt ungünstige thermomechanische und thermochemische Materialeigenschaften zu erwarten. Die in dieser Arbeit herausgestellte inadequate Hochtemperaturstabilität der untersuchten Materialien kann auf alle anderen polymer abgeleiteten Keramiksysteme übertragen werden.

2 Literature Review

2.1 Advanced Ceramics by Molecular Design

According to Niihara, the incorporation of nano-sized secondary phases in non-oxidic and oxidic ceramics leads to improved macroscopic high-temperature mechanical properties (such as hardness, toughness, strength and fracture resistance for creep and fatigue, as well as thermal shock resistance or even superplastic behavior) of the final ceramics, referred to “ceramic nanocomposites” [1-10]. Since the early work of Niihara, numerous studies in the field related to ceramic science have been focusing on the synthesis of novel advanced nano-structured ceramics and the correlation of their mechanical, physical and chemical properties to microstructure.

A new class of ceramic composites has been derived from modified or functionalized organosilicon polymeric precursors via thermal conversion, and their physical, chemical and mechanical properties have been studied to exploit their potential as materials for structural applications or applications in various functional devices [11-25]. Such organosilicon precursors are single-source silicon-based polymers with tailorable compositions that contain varying amounts of Si, H, C, O, N and small amounts of other elements such as B or transition metals [12-16,26,27]. Selected organosilicon precursors have been used and evaluated for processing protective coatings [28-30], fibres [31-33], ceramic-matrix cornposites [34], monolithic material [35], and porous catalyst support and membranes [36].

A key argument in the literature is the strong relationship between the molecular structure and composition of preceramic polymers and the nano/microstructure of the final ceramic products. The following two sections present a basis of knowledge with respect to the stepwise structural evolution of common polymeric precursors including transition metal modified precursors to the two major PDC systems namely SiOC (section 1.2) and SiCN (section 1.3) upon processing and pyrolysis.

2.2 The SiOC System

Silicon oxycarbide (SiOC)-based ceramics are typically obtained via pyrolysis of poly(organosiloxanes) in an inert gas atmosphere around 1000°C. Preceramic precursors for SiOC-based materials can be synthesized by sol–gel techniques starting from various substituted alkoxysilanes [37,38]. Likewise, commercially available poly(organosiloxanes) can be used [21,22,39]. The sol–gel technique

allows for chemical modification of functional organosilanes (siloxanes) or hydroxyl terminated polysiloxanes with transition metal alkoxides [13]**.** Babonneau et al. (1994) started from mixtures of such sol-gel precursors and zirconium n-propoxide and obtained so-called hybrid gels upon the hydrolysis and condensation process [40]. As pointed out by Ionescu et al. (2012) [13], the ceramization process of alkoxide-modified polysiloxanes is intrinsically complex. According to Babonneau et al. (1994), the metal alkoxide promoted the condensation of the silane precursor via formation of an intermediate phase containing Si-O-M (M= Ti, Zr) bonds [40]. Results obtained using X-ray absorption techniques indicate the presence of zirconia nanoparticles produced in the gel [41]. Dirè et al. (1998) [41] found during the pyrolytic conversion of zirconium alkoxide modified polysiloxane gels a pronounced evolution of methane at quite low temperature (at 275°C and above) that was attributed to Si-C cleavage due to the reaction between the Zr-oxide based phase and the siloxane chains at $Si\text{-}CH_3$ sites, being consistent with FTIR results. In the same reference, methane evolution was also detected at higher temperature (around 500°C), which is typically a result of Si-C bond cleavage associated with the usual polymer-to-ceramic transformation reactions of the polysiloxane, as revealed via FTIR analysis. However, in the case of unmodified polysiloxanes, these transformation reactions typically occur above 600°C [42,43]. Dirè et al. (1998) [41] noted that in the case of the zirconium alkoxide modified gels, the extent of methane evolution, which seemed to be correlated with the Zr content of the gels, was seen an indication for macromolecular structural arrangements of polysiloxane chains and the presence of the zirconia-based phase. Apart from methane evolution, volatile siloxane oligomers can typically be detected during pyrolysis of polysiloxanes, which were attributed to rearrangements within the polysiloxane network that involve Si–C and Si–O bond cleavages [13,41-43]. However, according to Dirè et al. (1998) [41], this typically occurred at lower temperature (around 500°C) in the case of the zirconium alkoxide modified gels as compared to unmodified polysiloxanes. While during Si-O/Si-O bond exchange, the silicon functionality is maintained, Si-O/Si-C bond exchange typically generates a different silicon unit and a more cross-linked network which, upon pyrolysis at the usual temperature (1000°C), entails an amorphous oxycarbide phase that contains mixed silicon units ($SiC_xO_{4-x}^{4-}$) [41] (and residual free carbon), similar to unmodified polysiloxanes [13,34,44-46]. Furthermore, the network modification that was clearly detected via FTIR at 600°C and above, can

in part be attributed to the evolution of a zirconia phase [41]. Upon pyrolysis at 1000°C, a crystalline ZrO_2 phase embedded in a SiOC glass matrix was detected [47].

Commercially available polysiloxanes having suitable functional groups (such as hydroxyl or alkoxy) can be chemically modified upon sol–gel-like processes via the reaction with transition metal alkoxides [13]. Recently, ceramic materials were prepared from a mixture of a polymethylsilsesquioxane (PMS) and hafnium n-butoxide [22]. Likewise, PMS has also been modified with zirconium n-propoxide [21]. Ionescu et al. (2010) stated that, while unmodified PMS contains hydroxyl groups, no hydroxyl groups were detected via FTIR spectroscopy upon modification with hafnium alkoxide [22]. Furthermore, in the case of hafnium alkoxide-modified polysiloxane, Si–O–Hf bonds were detected in the FTIR spectra, which was seen to point toward a substitution reaction (condensation reaction) of hafnium butoxide at the hydroxyl moieties of PMS with concomitant release of butanol, which was detected via mass-spectrometry [22], which is consistent with results of the aforementioned study of Dirè et al. (1998) [27]. According to Ionescu et al. (2010), hafnium alkoxide modification induces that the cross-linking processes occur at lower temperatures than in the case of unmodified PMS, consistent with results of Dirè et al. (1998). The final ceramization step was found to occur in the same temperature range for unmodified PMS and of the alkoxide modified PMS [22].

Upon thermal treatment at 600°C, major changes in the molecular structure can be detected in all unmodified polysiloxanes (see e.g. [39] and also in the case of hafnium alkoxide modified PMS [22]). At 600°C, backbone rearrangements are in progress (formation of methylene bridges, Si-C-Si bond increase, Si-C cleavage) [39]. Between 600 and 800°C, the transition between a hydrocarbon-containing polymeric compound and an inorganic glassy network occurs [39]. ^{29}Si spectra at 800°C typically indicated a glassy SiOC disordered structure with broad peaks due to the distribution of silicon sites, namely SiC_3O^{4-}, $SiC_2O_2^{4-}$, $SiCO_3^{4-}$ and SiO_4^{4-} [22,39]. In the case of a ceramic pyrolyzed at 800°C derived from hafnium alkoxide-modified PMS, the ^{29}Si MAS NMR signal of the tetrahedral SiO_4^{4-} units exhibited a downfield shift of about 4 ppm with respect to the value obtained for unmodified silicon oxycarbide ceramics (at the same temperature), which is an indication of the presence of hafnium (formation of Si-O-Hf heterometallic bonds) [22]. The amount of SiO_4^{4-} and SiC_4^{4-} units in ^{29}Si NMR spectra significantly increased upon annealing at

1000°C, revealing the formation of Si-O rich and Si-C rich domains due to molecular bond restructuring [39]. ^{29}Si NMR analysis indicated the change from C-H to C-Si bonds via restructuring at Si-CH_3 groups, consistent and associated with concomitant hydrogen evolution [39].

As for all SiOC materials, in the temperature range between 1000 and 1500°C, redistribution of the silicon sites continues with the increase of SiO_4^{4-} and SiC_4^{4-} units, while, concomitantly, mixed $SiC_xO_{4-x}^{4-}$ (x = 1, 2 or 3) sites are either hardly detectable or completely disappear, depending on temperature and the value x, respectively, indicating the onset of the molecular phase segregation, typical to SiOC materials [22,39,48].

Two-dimensional (2D) ^{29}Si correlation NMR spectroscopy (COSY) and double quantum (DQ) NMR spectroscopy, performed on a polysiloxane-derived SiOC PDC pyrolyzed at 1100°C, indicated connectivity between SiO_4^{4-}–SiO_3C^{4-} and SiO_4^{4-}–$SiO_2C_2^{4-}$ units through Si–O–Si linkages and the absence of bonding between SiO_4^{4-} and SiC_4^{4-} units, consistent with their spatial isolation and the lack of C–O bonding [17]. Widgeon et al. (2010) proposed a structural model for the SiOC PDC material investigated that suggests local confinement of Si-C rich units at the interface between a segregated sp^2-hybridized graphitic carbon phase and the Si-O rich units forming a “continuous mass fractal backbone of corner-shared mixed-bonds-tetrahedral units” [48].

Electron energy-loss spectroscopy (EELS) also allowed for the detection of phase separation indicated by Si–O bonding in amorphous SiOC materials [49,50]. Gregori et al. (2006) showed that, beside Raman, ^{13}C and ^{29}Si NMR spectroscopy, EELS and electron diffraction (ED) pattern analysis are highly sensitive analytical tools to allow for the detection of the phase separation process and the evolution of the free carbon in SiOC materials; they yielded results that were in good agreement with the ^{13}C and ^{29}Si NMR data [50]. In one carbon-rich SiOC material, sp^2 carbon sites were already detected at 800°C via ^{13}C NMR that can be assigned to a separate aromatic carbon phase [50]. This formulation, upon pyrolysis at 1000°C, exhibited distinct structural features due to a high number of sp^2 carbon (graphitic) sites, according to EELS, while little differences among the EELS spectra from 1000 to 1450°C were recognized. Notably, upon exposure to 1200°C, the ED pattern of this material showed distinct though weak graphite-like features due to the growth of graphene layer stacks [50]. In addition, upon exposure to 1450°C, the ED pattern clearly

showed SiC signals and graphitic carbon features. High-resolution (HR) imaging consequently revealed for this formulation a high fraction of turbostratic features assigned to the free carbon phase, homogeneously dispersed within an amorphous matrix upon annealing at 1450°C [50]. For the other carbon-rich SiOC formulation investigated in [50], exposure to 1450°C resulted in a first modification of the corresponding EELS fine structure of the C-K edge, as the sp^2 features assigned to graphite-like carbon now revealed an incremental increase as compared to the spectra derived at lower temperatures due to a proceeding growth of sp^2 carbon sites during heat treatment from 1000 to 1450°C. In addition, at 1450°C, in the ED pattern a signal though being weak can be assigned to graphene clusters, as also evidenced by the EELS technique. Diffusely scattered electron rings in the ED pattern gained in intensity from 1000 to 1450°C, which were assigned to SiC and SiO_2 amorphous domains, which underlines a proceeding rearrangement process around silicon in this material not affected by the sp^2 carbon formation, which is in good agreement with ^{29}Si NMR results. The HRTEM image, at 1450°C, showed only very few turbostratic carbon clusters, while the Fast-Fourier-Transform (FFT)-filtered HRTEM image revealed the presence of SiC nanocrystals. According to Gregori et al. (2006), the distinct structural evolution of the Si sites and free carbon phase with increasing temperature for the one SiOC formulation, according to ^{13}C NMR, EELS, ED and HRTEM imaging, is directly related to the high content of aromatic carbon sites in the starting precursor [50]. Furthermore, energy-filtered (EF) TEM elemental ratio profiles of bulk regions suggested that the evolution of carbon-rich domains and in parallel the phase separation of the matrix was characteristic for the entire bulk [50]. Note that the organization and growth of the graphene layers observed and characterized in this study imply a locally enhanced mobility of carbon at elevated temperatures. Yet, the mobility of carbon in SiOC as in all other PDC systems is still not well understood.

In the case of a ceramic material prepared from hafnium alkoxide modified PMS and pyrolyzed at 1300°C, leading to novel HfO_2/SiHfCO nanocomposites, the SiO_4^{4-} signal dominates in the ^{29}Si MAS NMR spectrum, and the SiC_4^{4-} signal can also clearly be detected [22]. The SiO_4^{4-} signal in the ^{29}Si MAS NMR spectra derived from pyrolyzed samples (in the range between 600 and 900°C) reveal a proceeding high-field shift with increasing temperature that was seen as a consequence of the precipitation process of hafnia [22]. The as-received ceramic product upon pyrolysis

at a rather low pyrolysis temperature (900°C) was analyzed by HRTEM imaging and electron diffraction revealing an overall amorphous microstructure with local enrichment of Hf-oxide precipitates less than 5 nanometers in lateral size. It should be noted that here only samples that were thermally treated at 900°C and above were characterized, since as-prepared polymers are typically unstable under the incident electron beam in the TEM and, hence, the preceramic material was not included in the microstructure characterization. Upon pyrolysis at 1100°C, a quite homogeneous dispersion of hafnia nanocrystals in an amorphous SiHfOC matrix was locally monitored via HRTEM. These findings, according to Ionescu et al. (2010), suggest a homogeneous nucleation mechanism for the oxide phase [22].

Ionescu (2014) reported an improved oxidation resistance of HfO_2/SiHfOC nanocomposites with respect to that of a hafnia-free SiOC material (at 1300 and 1400°C annealed for 50 h, respectively) [1]. Interestingly, the significant difference between the performance of the SiOC and HfO_2/SiHfOC materials in oxidative environment is, according to [1], not related to the presence of hafnia nanoparticles in the HfO_2/SiHfOC sample, but is thought to be a consequence of the formation of hafnon at the surface of the HfO_2/SiHfOC sample studied, according to XRD data, because the oxygen diffusivity in hafnon is expected to be several orders of magnitude lower than in vitreous silica.

HfO_2/SiHfOC nanocomposites resisted exposure to even 1600°C under argon (5 h) without significant weight loss, in contrast to a hafnia-free sample showing nearly 50% weight loss upon annealing at 1600°C for 5 h due to decomposition by the carbothermal reduction reaction [23]. In the case of the former material, strong X-ray diffraction signals were observed that were assigned to hafnon, cristobalite, monoclinic and tetragonal hafnia, as well as silicon carbide [23]. The presence of silicon carbide was assigned to the phase separation-crystallization process of SiOC PDCs, which leads to the formation of SiO_2, SiC and free carbon, but not to carbothermal reduction reactivity [23]. The origin of the improved thermal stability of HfO_2/SiHfOC nanocomposites as compared to that of the hafnia-free material remains still unclear. In [23], it was speculated that the silica phase present in the bulk matrix is consumed by a solid-state reaction with hafnia nanocrystals forming hafnon [51,52] competing effectively with the carbothermal reduction of silica, which is at least consistent with the observed only slight weight loss during exposure to 1600°C [23]. An additional systematic investigation utilizing TEM of hafnon formation

in this and additional HfO_2/SiHfOC samples annealed at various temperatures in the range between 1450 to 1600°C under the same conditions confirmed the presence of hafnon in the bulk of the material annealed at 1600°C, consistent with XRD results.[1] However, its presence was always related to SiO_2-rich, impurity-like inclusions dispersed in the bulk matrix of this material (1600°C), meaning that hafnon was located at HfO_2/SiO_2 interfaces, but, notably, was not a characteristic feature of the entire bulk material, showing the presence of tetragonal and monoclinic hafnia crystallites only.[2]

2.3 The SiCN System

Bill et al. (1998) investigated the reactions during pyrolysis, i.e., the ceramization process, in particular, the possible effect of the presence of methyl and vinyl functional groups in the precursor, using different starting precursors, namely polyhydridomethylsilazane (PHMS) and polyvinylsilazane (PVS) [53]. PHMS consists of crosslinked six-membered rings constituted form Si-N bonds. At 550°C, a first modification of the environment of Si was detected via ^{13}C and ^{29}Si NMR analysis and IR spectroscopy. In the temperature range between 400 and 800°C, methane evolution, and, between 350 and 1050°C, hydrogen evolution was detected via TG/MS investigations, respectively. Si-N environments were clearly detected via ^{29}Si NMR at 625°C attributed to crosslinking reactions. Si-C environments were clearly detected upon pyrolysis at 625°C proposed to be a result of addition reactions. Such addition reactions as well as crosslinking reactions continued with increasing temperature. The authors concluded that ceramization is associated with a “short-range ordering” within the precursor network leading to a short-range phase separation into Si-C-rich and Si-N-rich areas. Furthermore, neutron scattering analysis observed in the as-pyrolyzed material (1050°C) revealed the presence of amorphous “graphite-like” carbon. High-resolution transmission electron microscopy investigations showed that despite the observed short-range ordering during pyrolysis (NMR data), the as-pyrolyzed PHMS derived material was fully amorphous. In the case of PVS, ceramization has been shown to be completely different [53]. Low-temperature crosslinking reactions such as vinyl group polymerization were

[1] Unpublished results.

[2] Unpublished results. The origin of such inclusions is not yet known. Figure 35 and 36 in the Appendix depict the observed microstructure around single hafnon crystals within the bulk of this material, as evidenced by SEM (Figure 35) and TEM (Figure 36).

observed. Early formation of a separate sp^2 hybridized carbon phase (around 625°C) was promoted by the loss of molecular hydrogen, as revealed via MS and ^{13}C NMR. At 550°C, Si-N environments were clearly detected via ^{29}Si NMR proposed to form via transamination reactions. Evaporation of a small amount of ammonia between 700 and 800°C was detected via MS. Thus, a low-temperature phase separation of Si_3N_4-like domains dispersed in a sp^2 hybridized carbon phase was proposed in the case of PVS-derived ceramics. These results are consistent with results reported in [54,55] revealing that the structure of the SiCN PDC glass and the amount of the segregated free carbon phase are correlated with the starting polymer chemistry. Bill et al. (1998) also reported that additional heat treatment of the PHMS- and PVS-derived materials entailed different final phase compositions above the carbothermal reduction temperature (1500°C) [53].

According to Kleebe et al. (2009) [56], the process of phase separation due to structural rearrangements in the amorphous network with increasing pyrolysis temperature clearly below initial crystallization is characteristic for the SiCN system. In this context, NMR results are consistent with results obtained via SAXS [57] and energy-filtered selected area electron diffraction technique during TEM imaging [58]**,** but not with HRTEM imaging, since the latter technique does not allow for the detection of phase separation within the amorphous stage [56]. Energy-filtered selected area electron diffraction (EF-SAED) analysis allowed for a distinction between the glass networks in two SiCN ceramics with only slightly different composition derived from two precursors of very different polymer architecture [58]. The materials annealed at 1000°C already revealed slightly different ring intensities in the corresponding electron diffraction patterns in both cases [58]. Upon thermal treatment at 1400°C, the SAED intensity profile analysis allowed for an even more pronounced distinction between the two glass networks that were attributed to a proceeding structural rearrangement in the amorphous networks of these two materials studied [58]. Beside SAED pattern analysis, EELS was also shown to be particularly useful in monitoring the local bonding of silicon and carbon (near-edge fine structure of Si-L edge and C-K edge) in polymer-derived SiCN ceramic materials and to characterize the free carbon phase [59]. For two different SiCN materials, Si-N bonding was detected beside a contribution of Si-C bonding upon pyrolysis at 1000°C. Annealing at 1400°C did not induce any significant modification on the near-edge fine structure of the Si-L edge [50]. This finding allowed for the conclusion that

neither additional incorporation of carbon into the Si-based network nor expulsion of carbon from this network occurred during the subsequent heat treatment [59]. Furthermore, upon annealing at 1400°C, a clear modification of the near-edge structure of the carbon-K edge was observed with respect to that observed in the case of the sample pyrolyzed at 1000°C, which can be assigned to the evolution of the amorphous free carbon phase towards a graphite-like structure [59]. Kleebe and coworkers showed that the initial organization of the free carbon phase can be imaging via HRTEM using different defocus settings of the objective lens (underfocus, overfocus) [50,60]. The exceptional properties of amorphous SiCN PDCs, such as high chemical durability in aggressive media and their resistance to crystallization, are attributed to the presence of the dispersed ‘‘free’’ carbon phase [13].

Recently, polysilazane HTT1800 that exhibits methyl and vinyl functional groups attached to a (R_2Si-NH) linear backbone, a molecular built-up that contains in part the same units as in PHMS and PVS [61], was modified with hafnium-n-butoxide and converted to HfO_2/SiHfCNO ceramic nanocomposites [62]. In the temperature range from ambient temperature to 350–400°C, cross-linking of the precursor occurred via hydrosilylation and vinyl polymerization processes [62], which were also observed in the case of PHMS and PVS [53]. Early upon pyrolysis at 400°C, a minor fraction of Si-N environments can be detected via ^{29}Si NMR and was attributed to transamination reactions beside mainly mixed SiCN environments attributed to vinyl polymerization and hydrosilylation of vinyl groups, as confirmed via ^{13}C NMR [62]. Besides mixed SiCN environments, the sample pyrolyzed at 400°C showed an additional signal in the ^{29}Si NMR spectrum, which was assigned to an Si-O environment. The presence of the Si-O environment was shown to rely on the reaction of hafnium alkoxy end groups within the polymeric precursor leading to Si-O-Hf bonds with concomitant evolution of volatile amines [62]. With increasing pyrolysis temperature (700°C), Si-N and mixed SiCN environments can clearly be seen in the ^{29}Si NMR spectrum, beside Si-O environments. Hafnium is second nearest neighbor of Si in SiO_4^{4-} sites as deduced from the downfield shift of the ^{29}Si NMR signal assigned to SiO_4^{4-} (at 700°C) [62]. Si-O environments were proposed to form due to rearrangement reactions of ≡Si−N= and butoxide groups present within the cross-linked polymer, as consistent with the detection of amines [62]. Papendorf et al. (2011) [63] showed that the reaction of HTT1800 with the hafnium alkoxide entails a

homogeneous dispersion of the metal within the final ceramic upon pyrolysis at 1100°C, as further confirmed on samples pyrolyzed at 1300°C using TEM-EDS (see chapter 6). At temperatures from 500 to ca. 750°C, hydrogen evolution takes place as a result of dehydrocoupling reactions or decomposition processes of hydrocarbon substituents [62]. Within the same temperature range, strong evolution of ammonia and methane was detected by MS [62]. Furthermore, at temperatures of 450 to 750°C, butene and water evolved assigned to the decomposition of butoxy end groups at hafnium sites [62]. Upon pyrolysis at 900°C and 1100°C, respectively, the trend towards the dominant evolution of Si-N environments was supported by ^{29}Si NMR analysis, which was not reported for unmodified polysilazanes and, therefore, was thought to be related to the modification with the hafnium alkoxide [62]. Interestingly, Ionescu et al. (2011) [62] observed a strong decrease of oxygen containing environments in the ^{29}Si NMR spectrum at 900°C, while, at 1100°C, oxygen containing environments again were clearly detected via ^{29}Si NMR. TG analysis showed no mass loss at temperatures beyond 750°C consistent with elemental analysis showing similar oxygen and nitrogen contents for the as-pyrolyzed samples pyrolyzed at 700 and 900°C, respectively [62]. At 700°C, a sp^2 hybridized carbon phase was detected in the corresponding ^{13}C NMR spectrum [62]. Only upon pyrolysis at 1300°C, a minor signal assigned to Si-C environments was detected via ^{29}Si NMR [62], which is consistent with the proceeding structural modifications in PDC glass networks during thermal treatment [56]. According to Ionescu et al. (2011) [62], the reduction of Si-O environments (at 700°C), as indicated by ^{29}Si NMR data, is a consequence of molecular rearrangements in the glass network due to hafnia precipitation occurring at approximately this temperature, although an indication for local formation of hafnia was not observed using HRTEM in a sample pyrolyzed at 800°C. However, upon pyrolysis at 900°C, the precipitation of hafnia was supported by HRTEM imaging [62]. The experimental feasibility to introduce a dispersed nanosized oxide phase into a polymer-derived SiCN matrix, which can be considered a multiphase oxide/non-oxide composite at the nanometer scale has already been demonstrated earlier by Saha et al. (2005) [64].

Improved thermal stability with respect to carbothermal reduction reactivity (according to the reaction $Si_3N_4 + 3\ C \rightarrow 3\ SiC + 2\ N_2$ was shown for a Hf-modified material exposed to 1600°C [63]. Additional TEM confirmed the presence of turbostratic carbon and Si_3N_4, consistent with XRD [63] and Raman data [61, p. 61], apart from

residual closed porosity. While TEM-EDS analysis revealed a homogeneous incorporation of Hf in dense regions of this sample, locally pronounced microstructural variations related to compositional variations were also observed. In fact, the crystallization of Si_3N_4 was only observed locally. Furthermore, the presence of HfO_2 crystallites was confirmed via SEM and TEM, consistent with XRD data [63], which, however, was unexpectedly always related to an oxygen-rich, carbon- and nitrogen-depleted matrix. The origin of the compositional variations observed in this sample using EDS is not yet known. This finding (the occurrence of HfO_2 precipitates related to an oxygen-rich SiHfO(C,N) matrix) is, however, consistent with results of the present work presented in chapter 6.2 and 6.3. The reason for the stabilization of Si_3N_4 reported in [63] can be rationalized assuming that the escape of molecular nitrogen is hindered within the central region of the monolithic sample, leading to a local built-up of a high nitrogen partial pressure. An increased nitrogen partial pressure (1 bar) is reported in the literature to stabilize Si_3N_4 against carbothermal reduction up to an equilibrium reaction temperature of 1484°C [65]. However, in [66], Si_3N_4 was stable at even higher temperatures (1600°C), which was attributed to the embedment of Si_3N_4 in an amorphous matrix locally hindering the reaction between Si_3N_4 and carbon.

2.4 References

[1] K. Niihara (1991). New design concept of structural ceramics: Ceramic nanocomposites. *J. Ceram. Soc. Jpn.*, 99(1154), 974-982.

[2] M. Sternitzke (1997). Structural ceramic nanocomposites. *J. Eur. Ceram. Soc.*, 17(9), 1061-1082.

[3] B. Derby (1998). Ceramic nanocomposites: mechanical properties. *Curr. Opin. Solid St. M.*, 3(5), 490-495.

[4] F. Wakai, Y. Kodama, S. Sakaguchi, N. Murayama, K. Izaki, and K. Niihara (1990). A superplastic covalent crystal composite. *Nature*, 344(6265), 421-423.

[5] K. Niihara, K. Suganuma, A. Nakahira, and K. Izaki (1990). Interfaces in Si_3N_4-SiC nano-nomposite. *J. Mater. Sci. Lett.*, 9(5), 598-599.

[6] K. Niihara, K. Izaki, and T. Kawakami (1991). Hot-pressed Si_3N_4-32% SiC nanocomposite from amorphous Si-C-N powder with improved strength above 1200 °C. *J. Mater. Sci. Lett.*, 10(2), 112-114.

[7] A. Sawaguchi, K. Toda, and K. Niihara (1991). Mechanical and electrical properties of Al_2O_3/SiC nanocomposites. *J. Ceram. Soc. Jpn.*, 99(6), 523-526.

[8] G. Sasaki, H. Nakase, K. Suganuma, T. Fujita, and K. Niihara (1992). Mechanical properties and microstructure of Si_3N_4 matrix composite with nanometer scale SiC particles. *J. Ceram. Soc. Jpn.*, 100(4), 536-540.

[9] J. R. Zeng, I. Tanaka, Y. Miyamoto, O. Yamada, and K. Niihara (1992). High-temperature strength and cavitation threshold of silicon-nitride silica ceramics. *J. Am. Ceram. Soc.*, 75(1), 195-200.

[10] J. R. Zeng, I. Tanaka, Y. Miyamoto, O. Yamada, and K. Niihara (1992). Densification and microstructural development of silicon-nitride silica during hot isostatic pressing. *J. Am. Ceram. Soc.*, 75(1), 148-152.

[11] E. Ionescu (2014). *Ceramic nanocomposites with advanced structural and functional properties.* (Habilitation Thesis.) Technische Universität Darmstadt, Darmstadt, Germany.

[12] R. Riedel (2012). Nanoscaled inorganic materials by molecular design. *Chem. Soc. Rev.*, 41, 5029-5031.

[13] E. Ionescu, H.-J. Kleebe, and R. Riedel (2012). Silicon-containing polymer-derived ceramic nanocomposites (PDC-NCs): preparative approaches and properties. *Chem. Soc. Rev.*, 41(15), 5032-5052.

[14] P. Colombo, G. Mera, R. Riedel, and G. D. Sorarù (2010). Polymer-derived ceramics: 40 years of research and innovation in advanced ceramics. *J. Am. Ceram. Soc.*, 93, 1805–1837.

[15] P. Colombo, R. Riedel, G. D. Sorarù, and H.-J. Kleebe (Eds.) (2010). *Polymer derived ceramics: from nanostructure to applications*. Lancaster, PA: DEStech Publications.

[16] R. Riedel, G. Mera, R. Hauser, and A. Klonczynski (2006). Silicon-based polymer-derived ceramics: synthesis properties and applications - a review. *J. Ceram. Soc. Jpn.*, 114, 425–444.

[17] G. Mera, A. Navrotsky, S. Sen, H.-J. Kleebe, and R. Riedel (2013). Polymer-derived SiCN and SiOC ceramics – structure and energetics at the nanoscale. *J. Mater. Chem. A*, 1, 3826-3836.

[18] S. Martinez-Crespiera, E. Ionescu, M. Schlosser, K. Flittner, G. Mistura, R. Riedel, and H. F. Schlaak (2011). Fabrication of silicon oxycarbide-based microcomponents via photolithographic and soft lithography approaches. *Sensor Actuat. A-Phys.*, 169(1), 242–249.

[19] S. Martinez-Crespiera, G. Mera, and R. Riedel (2012). In S. Bernard (Ed.), *Design, processing and properties of ceramic materials from preceramic precursors* (pp. 37-72). New York, NY: Nova Science Publishers.

[20] C. Linck, E. Ionescu, B. Papendorf, D. Galuskova, D. Galusek, P. Sajgalik, R. Riedel (2012). Corrosion behavior of silicon oxycarbide-based ceramic nanocomposites under hydrothermal conditions. *Int. J. Mater. Res.*, 103, 31–39.

[21] E. Ionescu, C. Linck, C. Fasel, M. Müller, H.-J. Kleebe, and R. Riedel (2010). Polymer-derived SiOC/ZrO_2 ceramic nanocomposites with excellent high-temperature stability. *J. Am. Ceram. Soc.*, 93, 241–250.

[22] E. Ionescu, B. Papendorf, H.-J. Kleebe, F. Poli, K. Müller, and R. Riedel (2010). Polymer-derived silicon oxycarbide/hafnia ceramic nanocomposites. Part I: Phase and microstructure evolution during the ceramization process. *J. Am. Ceram. Soc.*, 93(6), 1774-1782.

[23] E. Ionescu, B. Papendorf, H.-J. Kleebe, and R. Riedel (2010). Polymer-derived silicon oxycarbide/hafnia ceramic nanocomposites. Part II: Stability toward decomposition and microstructure evolution at T>>1000°C. *J. Am. Ceram. Soc.*, 93(6), 1783-1789.

[24] J. Kaspar, C. Terzioglu, E. Ionescu, M. Graczyk-Zajac, and R. Riedel (2014). A novel preparative approach towards stable tin-containing anodes for lithium-ion batteries with outstanding cycling stability: SiOC/Sn nanocomposites. *Adv. Funct. Mater.*, 24, 4097-4104.

[25] M. Reinold, M. Graczyk-Zajac, Y. Gao, G. Mera, and R. Riedel (2013). Carbon-rich SiCN ceramics as high capacity/high stability anode material for lithium-ion batteries. *J. Power Sources*, 236, 224-229.

[26] G. Mera and E. Ionescu (2013). Silicon-containing preceramic polymers. *Encyclopedia of polymer science and technology* (4th ed.). Wiley Online Library.

[27] G. Mera and R. Riedel (2009). Organosilicon-based polymers as precursors for ceramics. In P. Colombo, R. Riedel, G. D. Sorarù, and H.-J. Kleebe (Eds.), *Polymer derived ceramics: from nanostructure to applications* (pp. 51-89). Lancaster, PA: DEStech Publications.

[28] M. Ducarroir, W. Zhang, and R. Berjoan (1993). SiCN coatings prepared by PACVD from TMS-NH_3-Ar system on steel. *J. Phys. IV* France 03 C3-247-C3-254.

[29] S. R. Shah and R. Raj (2007). Multilayer design and evaluation of a high temperature environmental barrier coating for Si-Based ceramics. *J. Am. Ceram. Soc.*, 90(2), 516–22.

[30] K. Terauds, D. B. Marshall, and R. Raj (2013). Oxidation of polymer-derived HfSiCNO up to 1600°C. *J. Am. Ceram. Soc.*, 96(4), 1278-1284.

[31] J. Lipowitz (1991). Polymer-derived ceramic fibers. *Ceramic Bulletin*, 70, 1888-1894.

[32] A. Saha, S. Shah, and R. Raj (2003). Amorphous silicon carbonitride fibers drawn from alkoxide modified Ceraset (TM). *J. Am. Ceram. Soc*., 86(8), 1443–1445.

[33] A. Saha, S. Shah, and R. Raj (2004). Oxidation behavior of SiCN-ZrO_2 fiber prepared from alkoxide-modified silazane. *J. Am. Ceram. Soc.*, 87(8), 1556–1558.

[34] H. Zhang and C. G. Patano (1990). Synthesis and characterization of silicon oxycarbide glasses. *J. Am. Ceram. Soc*., 73(4), 958-963.

[35] R. Riedel, G. Passing, H. Schönfelder, and R. J. Brook (1992). Synthesis of dense silicon-based ceramics at low temperatures. *Nature*, 355, 714-716.

[36] R. M. Prasad, G. Mera, K. Morita, M. Müller, H.-J. Kleebe, A. Gurlo, C. Fasel, and R. Riedel (2012). Thermal decomposition of carbon-rich polymer-derived silicon carbonitrides leading to ceramics with high specific surface area and tunable micro- and mesoporosity. *J. Eur. Ceram. Soc*., 32(2), 477-484.

[37] G. D. Sorarù (1994). Silicon oxycarbide glasses from gels. *J. Sol-Gel Sci. Technol.*, 2(1-3), 843-848.

[38] F. Babonneau, G. D. Sorarù, G. D'Andrea, S. Dirè, and L. Bois (1992). Silicon oxycarbide glasses from sol-gel precursors. *Mater. Res. Soc. Proc.*, 271, 789-794.

[39] H.-J. Kleebe, G. Gregori, F. Babonneau, Y. D. Blum, and D. B. MacQueen (2006). Evolution of C-rich SiOC ceramics: Part I. Characterization by integral spectrocopic techniques: solid state NMR and Raman spectroscopy. *Int. J. Mater. Res.*, 97(6), 699-709.

[40] F. Babonneau (1994). Hybrid siloxane-oxide materials via sol-gel processing. Structural characterization. *Polyhedron*, 13(8), 1123-1130.

[41] S. Dirè, R. Campostrini, and R. Ceccato (1998). Pyrolysis chemistry of sol-gel-derived poly(dimethylsiloxane)-zirconia nanocomposites. Influence of zirconium on polymer-to-ceramic conversion. *Chem. Mater.*, 10(1), 268-278.

[42] L. Bois, J. Maquet, F. Babonneau, H. Mutin, and D. Bahloul (1994). Structural chararacterization of sol-gel derived oxycarbide glasses. Part I Study of the pyrolysis process. *Chem. Mater.*, 6(6), 796-802.

[43] V. Belot, R. J. P. Corriu, D. Leclerq, P. H. Mutin, and A. Vioux (1992). Thermal redistribution reactions in cross-linked polysiloxanes. *J. Polym. Sci. A*, 30(4), 613-623.

[44] R. J. P. Corriu, D. Leclercq, P. H. Mutin, and A. Vioux (1995). ^{29}Si nuclear magnetic resonance study of the structure of silicon oxycarbide glasses derived from organosilicon precursors. *J. Mater. Sci.*, 30(9), 2313-2318.

[45] C. G. Pantano, A. K. Singh, and H. X. Zhang (1999). Silicon oxycarbide glasses. *J. Sol-Gel Sci.Technol*., 14(1), 7–25.

[46] M. Monthioux and O. Delverdier (1996). Thermal behavior of (organosilicon) polymer-derived ceramics. V: Main facts and trends. *J. Eur. Ceram. Soc.*, 16, 721-737.

[47] S. Dirè, R. Ceccato, S. Gialanella, and F. Babonneau (1999). Thermal evolution and crystallisation of polydimethylsiloxane-zirconia nanocomposites prepared by the sol-gel method. *J. Eur. Ceram. Soc.*, 19(16), 2849-2858.

[48] S. J. Widgeon, S. Sen, G. Mera, E. Ionescu, R. Riedel, and A. Navrotsky (2010). ^{29}Si and ^{13}C solid-state NMR spectroscopic study of nanometer-scale structure and mass fractal characteristics of amorphous polymer derived silicon oxycarbide ceramics. *Chem. Mater.*, 22, 6221-6228.

[49] H.-J. Kleebe, C. Turquat, and G. D. Sorarù (2001). Phase separation in a SiOC glass studied by transmission electron microscopy and electron energy-loss spectroscopy. *J. Am. Ceram. Soc.*, 84(5), 1073–1080.

[50] G. Gregori, H.-J. Kleebe, Y. D. Blum, and F. Babonneau (2006). Evolution of C-rich SiOC ceramics: Part II. Characterization by high lateral resolution technique: electron energy loss spectroscopy. High-resolution TEM and energy-filtered TEM. *Int. J. Mater. Res.*, 97(6), 710-720.

[51] C. E. Curtis, L. M. Doney, and J. R. Johnson (1954). Some properties of hafnium oxide, hafnium silicate, calcium hafnate and hafnium carbide. *J. Am. Ceram. Soc.*, 37(10), 458-465.

[52] D. J. Salt and G. Hornung (1967). Synthesis and X-ray study of hafnium silicates. *J. Am. Ceram. Soc.*, 50(10), 549–550.

[53] J. Bill, J. Seitz, G. Thurn, J. Dürr, J. Canel, B. Z. Janos, A. Jalowiecki, D. Sauter, S. Schempp, H. P. Lamparter, J. Mayer, and F. Aldinger (1998). Structure analysis and properties of Si–C–N ceramics derived from polysilazanes. *Phys. Status Solidi A*, 166(1), 269-296.

[54] J. Seitz, J. Bill, N. Eggert, and F. Aldinger (1996). Structural investigations of Si/C/N-ceramics from polysilazane precursors by nuclear magnetic resonance. *J. Eur. Ceram. Soc.*, 16, 885-891.

[55] S. Traßl, D. Suttor, G. Motz, E. Rössler, and G. Ziegler (2000). Structural characterisation of silicon carbonitride ceramics derived from polymeric precursors. *J. Eur. Ceram. Soc.*, 20(2), 215–225.

[56] H.-J. Kleebe, G. Gregori, M. Weinmann, and P. Kroll (2010). Microstructure evolution and characterization. In P. Colombo, R. Riedel, G.-D. Sorarù, and H.-J. Kleebe (Eds.), *Polymer derived ceramics: from nanostructure to applications* (pp. 127-209). Lancaster, PA: DEStech Publications.

[57] G. Mera, A. Tamayo, H. Nguyen, S. Sen, and R. Riedel (2010). Nanodomain structure of carbon-rich silicon carbonitride polymer-derived ceramics. *J. Am. Ceram. Soc.*, 93(4), 1169–1175.

[58] H. Störmer, H.-J. Kleebe, and G. Ziegler (2007). Metastable SiCN glass matrices studied by energy-filtered electron diffraction pattern analysis. *J. Non-Cryst. Solids*, 353(30-31), 2867–2877.

[59] G. Gregori, H.-J. Kleebe, H. Brequel, S. Enzo, and G. Ziegler (2005). Microstructure evolution of precursors-derived SiCN ceramics upon thermal treatment between 1000 and 1400°C. *J. Non-Cryst. Sol.*, 351(16-17), 1393-1402.

[60] Y. Gao, G. Mera, H. Nguyen, K. Morita, H.-J. Kleebe, and R. Riedel (2012). Processing route dramatically influencing the nanostructure of carbon-rich SiCN and SiBCN polymer-derived ceramics. Part I: Low temperature thermal transformation. *J. Eur. Ceram. Soc.*, 32, 1857–1866.

[61] B. Papendorf (2012). *Keramische Nanokomposite auf Basis von SiOC/HfO_2 und SiCN/HfO_2: Herstellung und Untersuchungen zum Hochtemperaturverhalten.* (Unpublished doctoral dissertation.) Technische Universität Darmstadt, Darmstadt, Germany.

[62] E. Ionescu, B. Papendorf, H.-J. Kleebe, H. Breitzke, K. Nonnenmacher, G. Buntkowsky, and R. Riedel (2012). Phase separation of a hafnium alkoxide-modified polysilazane upon polymer-to-ceramic transformation – a case study. *J. Eur. Ceram. Soc.*, 32(9), 1873–1881.

[63] B. Papendorf, K. Nonnenmacher, E. Ionescu, H.-J. Kleebe, and R. Riedel (2011). Strong influence of polymer architecture on the microstructural evolution of hafnium-alkoxide-modified silazanes upon ceramization. *Small*, 7(7), 970-978.

[64] A. Saha, R. Raj, D. L. Williamson, and H.-J. Kleebe (2005). Characterization of nanodomains in polymer-derived SiCN ceramics employing multiple techniques. *J. Am. Ceram. Soc.*, 88(1), 232-234.

[65] H. J. Seifert, H. L. Lukas, and F. Aldinger (1998). Development of Si-B-C-N ceramics supported by phase diagrams and thermochemistry. *Berich. Bunsen. Gesell.*, 102(9), 1309-1313.

[66] H. Schmidt and W. Gruber (2010). Crystallisation kinetics of amorphous Si–C–N ceramics: Dependence on nitrogen partial pressure. *Philos. Mag.*, 90(11), 1485-1493.

3 Analytical Methods

3.1 Scanning Electron Microscopy

Figure 1 shows a schematic representation of the parts of a scanning electron microscope. The electron column of the SEM is the hearth of the instrument, where the electrons are generated, focused to a small spot, and scanned across the specimen surface (see **Figure 1**) [1, pp. 3-5]. In the electron gun, at the top of the column, electrons are emitted from either a tungsten or LaB_6 filament (older instruments) or via field emission (field emission gun, FEG) [1, pp. 3-5].

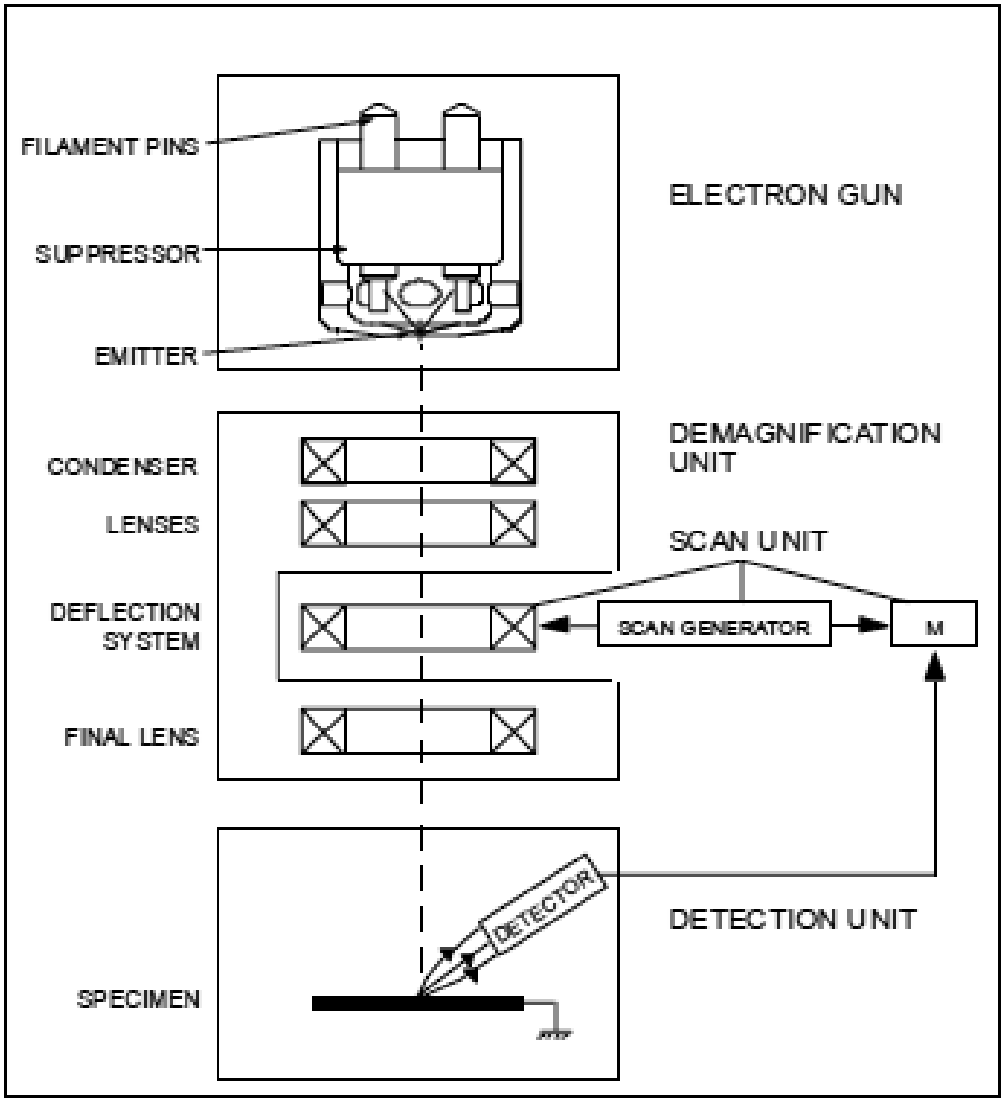

Figure 1: Schematic diagram of the parts of a scanning electron microscope (after http://fy.chalmers.se/~f10mh/Halvarsson/EM_intro_course_files/User_Manual_ESEM.pdf).

The critical parameters of the generated electron beam (energy, diameter, current, and divergence) are controlled utilizing electrical fields in the gun (Wehnelt cylinder

and an anode), magnetic fields in the condenser and objective lenses and stigmators, and apertures [1, pp. 8-15]. The electrons accelerated to a voltage in the range from 1 to 30 kV in the anode inside the gun enter the condenser lenses that focus the electron beam to a small spot. The final lens, the objective lens, creates the smallest cross-section of the beam with sizes in the range from micrometers to a few nanometers, depending on the type of electron source and its brightness (controlled via beam energy), onto the specimen surface which is located at a specific vertical distance from the objective lens (the so-called working distance). The function of the scanning system that consists of scan coils is to deflect the beam across the specimen. The image is formed by scanning the beam across the specimen in synchronism with the signal from a selected detector (usually Everhart-Thornley or solid-state detector). The electrons entering the specimen have nearly identical energy.

A beam limiting aperture inside the objective lens limits the beam convergence angle of the electron beam in order to reduce lens aberration effects and to improve the depth-of-field in the final image. The depth-of-field is defined as the vertical distance above and beneath the plane of optimum focus where every detail of the specimen in the image appears sharp [1, pp. 192-193]. It can be calculated from the ratio of the effective beam diameter at a small distance from the plane of optimum focus and the beam convergence angle and thus depends on both the beam convergence and the magnification. Increasing the working distance decreases the convergence angle and therefore increases the depth-of-field. Long working distances are usually used together with a small objective aperture in order to achieve the best depth-of-field. For example, an aperture size of 100 μm and a working distance of 5 mm results in a depth-of-field of 4 μm at a magnification of 5000x [1, p.193], while, in comparison, in light microscopy, the depth-of-field is typically about approximately 0.2 μm [2].

Specimen charging in the SEM can be overcome by slight specimen coating with a conducting material (usually carbon or gold). This is the case for operation in the high vacuum mode associated with all SEMs. Imaging of highly charging materials is a specific capability of the dedicated environmental SEM (ESEM). In this mode, a water vapour or auxiliary gas atmosphere is maintained in the specimen chamber leading to a pressure in the range range of 0.1 to 30 Torr (15 to 4000 Pa), while the electron gun and column are under higher vacuum.

Particularly relevant for SEM imaging are the detection of elastically and inelastically scattered electrons [3, pp. 200-203]. The energy distribution of all electrons that can be detected is dominated by a broad high-energy peak, spanning over the range from the incident beam energy down to 50 eV and is due to electron backscattering [4, p. 82]. The detection of electrons with energies less than 50 eV, designated as secondary electrons (SE), leads to a further narrow peak in the entire energy distribution in the range 2-5 eV [4, p. 91]. A relatively small fraction of backscattered electrons (BSE) is also included in this energy region.

Since in SEM bulk specimens are used, part of the incident electrons penetrate to a large depth in the specimen (interaction volume) with dimensions strongly dependent on beam energy and composition of the specimen, being typically in the μm range [4, pp. 65-70]. The so-called electron range, a single parameter, has been described in the literature and used as a simple measure of the interaction volume [4, p. 72].

Secondary electrons are created in the entire interaction volume as a result of inelastic scattering of the energetic beam electrons (on the order of 10-30 keV) at weakly bound conduction band or outer shell valence electrons (of energies in the eV range) that thereby receive sufficient energy to be ejected [4, p. 88]. The maximum depth of detectable SEs, designated as SE1s [1, p. 62], is very shallow (about 1 nm for metals and up to 10 nm for insulators) due to their low energy (only a few eV of energy) [4, pp. 91-92]. The emitted current of SE1s is measured by the so-called Everhart-Thornley (ET) detector. The SE1 signal is inherently a high-resolution signal that reflects both the lateral spatial resolution of the incident beam (i.e. beam size) and the shallow depth at which the SE is created. SE1s are therefore particularly suited for high-magnification surface imaging. A smaller probe gives a better resolution of SE images. Secondary electrons produced by the primary electrons in the interaction volume beneath the surface are designated SE2 [1, p. 62].

When the incident beam electron passes close to an atomic nucleus within the interaction volume, the electron is deflected by a large angle (backscattered electron, BSE) [3, p. 147]. Such large-angle electron deflections are elastic in origin [3, p. 200] and are the reason for beam broadening. Rutherford derived an expression for high-angle high-energy Coulomb scattering of an energetic He nucleus by an atomic nucleus [3, p. 147] that is useful for understanding large-angle electron scattering in the SEM. According to [3, p. 147], the Rutherford scattering cross-section, $d\sigma/d\Omega$, and thus “the probability” that an incident electron is scattered at a large angle

depends on the charge of the nucleus, Z, and the kinetic energy of the incident electron, E, as:

$$\frac{d\sigma}{d\Omega} = \frac{Z^2 e^4}{16E^2} \frac{1}{sin^4\left(\frac{\phi}{2}\right)}.$$

Here ϕ is the total scattering angle.

The above relationship, in particular the factor Z^2, also forms the basis for a contrast mechanism which is referred to as “atomic number contrast” (Z contrast). The sampling depth for BSEs is nearly in the order of the electron range that depends on both specimen composition and beam parameters (incident angle, energy) [4, pp. 86-87]. Therefore, the BSE signal cannot resolve features associated with the specimen surface at increased beam energies larger than 10 keV, increasing the electron range. Thus, the depth of emission for BSEs carrying information on composition is significantly larger than that for SEs. Because BSE have lower energy than incident beam electrons, BSEs have relatively great efficiency to transfer energy to weakly bound electrons of the specimen generating SE2. For the detection of BSEs, a dedicated solid-state detector is commonly used [1, p. 51].

The emission of characteristic X-ray photons with discrete energies characteristic of the element (as an example of inelastic electron scattering) can be analyzed via energy dispersive X-ray spectrometry (EDS) allowing for microchemical analysis. The emission of a characteristic X-ray is a result of a primary ionization by an energetic electron (i.e., a core electron is ejected from the atom and subsequently filling the resulting core hole by an outer electron of higher energy than the core electron ejected) [3, pp. 13-14]. The disposal of the excess energy occurs via X-ray photon emission. For X-ray microanalysis, i.e., EDS, usually high probe currents are used (and thus large probe sizes) [1, p. 196]. Due to the deep and broadened penetration of the incident electrons in the bulk specimens used in SEM, the depth of X-ray emission is on the order of 1 μm [3, p. 201], defining the spatial resolution obtained in chemical analysis in SEM.

3.2 Transmission Electron Microscopy

Conventional transmission electron microscopy (CTEM), which was employed in the present work, is one of the two basic techniques in TEM beside scanning TEM (STEM) [5].

“The transmission electron microscope has become the premier tool for the microstructural characterization of materials”, according to Fultz and Howe (2008) [3, p. 61]. As compared with the most sophisticated X-ray scattering techniques, namely synchrotron-radiation experiments, TEM offers higher spatial resolution by several orders of magnitude. While structural investigations using X-ray scattering techniques yield diffraction patterns that are more quantitative than electron diffraction patterns, TEM uses an important advantage of electrons over X-rays: in the TEM, electrons can be focused [3, p. 62] due to the action of the Lorentz force on electrons in a magnetic field of a magnetic lens. By focusing the electron beam, diffraction patterns can be obtained from individual crystals of only a few nm in size. The optics can also be used to generate images of the electron intensity at the exit plane. Beside diffraction imaging, which measures the intensities of selected diffracted electron waves (amplitude contrast), a TEM has the capability to operate in the high-resolution mode. Fultz and Howe (2008) [3, p. 62] stated that, here, “the phase of the diffracted wave is preserved and interferes constructively or destructively with the phase of the transmitted wave” (phase contrast).

Besides diffraction and direct imaging, the energetic incident electrons cause core excitations of the atoms of the specimen, which forms the basis for microchemical analysis via energy-dispersive X-ray spectrometry (EDS), as a core excitation is often followed by the emission of a characteristic X-ray photon [3, p. 164]. In EDS, an X-ray spectrum is acquired from the illuminated region whose lateral size is determined by the spot size of the focused electron beam. As incident electrons of several hundred keV are used in TEM, Rutherford backscattering of the incident beam electrons is of less amount, according to Fultz and Howe (2008) [3, p. 200], resulting in higher spatial resolution of analytical TEM as compared to a conventional electron microprobe, using bulk specimens [3, p. 201]. The probe size is determined by the current through the first condenser lens in the electron-beam forming system, while the convergence angle is determined by the size of the second aperture both affecting the intensity of X-ray emission in addition to the choice of probe current [11]. When spatial resolution is not the major goal, a large probe size and a high probe current provide the best counting statistics [1, p. 196]. The characteristic X-rays from the elemental constituents of the specimen can be used to determine the concentrations of the constituents on the basis of the thin-foil approximation approach, derived by Cliff and Lorimer (1975) [6].

Figure 2 shows a schematic representation of the parts of a TEM. The electron source is commonly provided by either a thermionic tungsten or LaB_6 filament (older instruments), or a cold or thermal field emission gun (FEG). In the case of a thermionic electron gun, the subsequent first condenser lens further demagnifies the first beam crossover from the Wehnelt electrode inside the electron gun [3, p. 87]. According to Fultz and Howe (2008) [3, p. 86], a cold FEG provides “a point source of illumination, and may not require the demagnification action of the first condenser lens.” In contrast to a thermionic electron source, thermal energy spread is absent in a cold FEG, which yields a highly monochromatic “point source of illumination” [3, p. 86].

The function of the second condenser lens is to control the convergence angle of the beam incident on the specimen and the electron beam current [3, p. 88]. In conventional TEM, the specimen (i.e., a thin foil) is illuminated by a near-parallel bundle of electrons, and the image is formed by the action of magnetic lenses around the specimen (objective lens) and subsequent to the specimen (intermediate lens).

The TEM has an objective aperture located in its back focal plane, which is used to select either the primary (transmitted) rays or the diffracted rays, forming the image. The back focal plane of the objective lens contains groupings of rays that have left the object at the same angle. It therefore contains the diffraction pattern of the illuminated object. In the image plane of the objective lens, all transmitted and diffracted rays leaving the object are combined to form an image. When the objective aperture selects the primary undiffracted beam (primary beam), a bright-field (BF) image of the object is projected on the fluorescent screen. The intermediate lens, subsequent to the objective lens, needs to be focused on the image plane of the objective lens. When the objective aperture selects at least one diffracted ray, a dark-field (DF) image of the object is formed. The BF/DF imaging modes yield complementary images. The diffraction contrast in the image is strongest when the image (BF and DF) is formed by selecting/omitting with the objective aperture a strong diffraction spot originating form a specimen area that has a specific crystallographic orientation relative to the incident beam. For imaging crystalline structures, therefore, both modes are often employed.

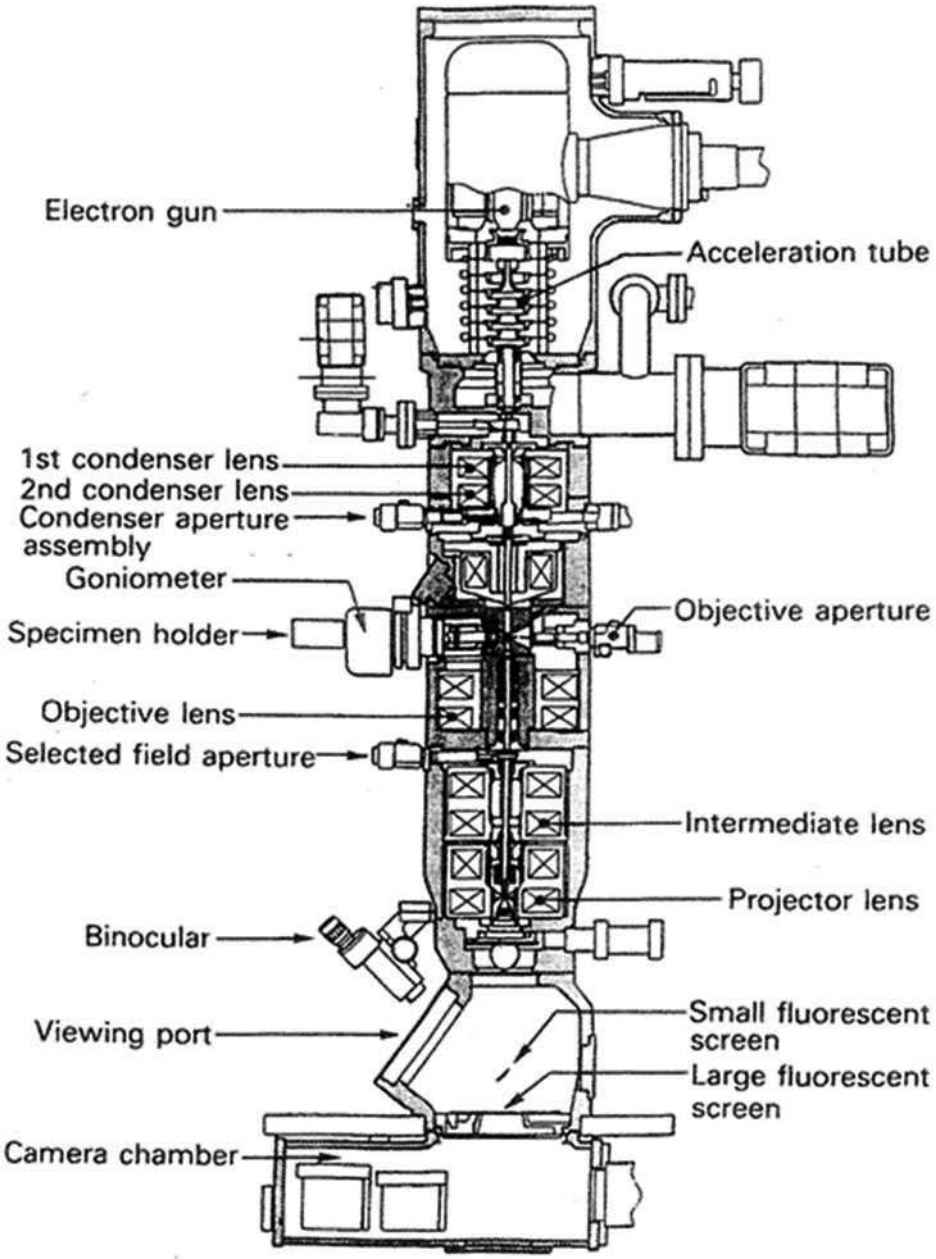

Figure 2: Schematic setup of a transmission electron microscope (after B. Fultz and J. Howe (2008) [3, p. 61]).

Without the objective aperture, a generic mass-thickness contrast can be detected, which originates from elastic scattering from individual atoms and therefore increases with atomic number and thickness of the illuminated specimen area [3, p. 73].

The diffraction pattern in the back focal plane of the objective lens can itself be imaged with the proper operation of the intermediate lens, which needs to be focused on the back focal plane of the objective lens. The transmitted and all of the diffracted beams are now imaged. A second aperture located in the image plane of the

objective lens is a means of confining the diffraction pattern to a selected area of the specimen with lateral size in the range of 1 μm (selected area electron diffraction, SAED). The SAED pattern obtained on the viewing screen originates from the selected area in the image mode. The convergent-beam electron diffraction (CBED) technique extends the diffraction analysis down to the nanoscale [3, p. 80] and also allows to obtain three-dimensional crystallographic information as well as the determination of local strain [5, pp. 319-338].

The TEM is also capable to operate in high-resolution mode, which is the niche technique for studying crystalline atomic structures in projection. In practice, the crystalline structure to be imaged is oriented in such a way that a major crystallographic axis is parallel to the direction of the incident electron beam, and the projected lateral atom arrangement extending along the viewing direction (i.e., along the incident beam direction) is imaged edge-on [7]. Fultz and Howe (2008) [3, p. 83] state that high-resolution imaging requires that the objective aperture in the back focal plane of the objective lens includes “both the transmitted beam and at least one diffracted beam.” The authors [3, p. 83] state further that “the transmitted (more precisely, forward-scattered) beam is needed to provide a reference phase of the electron wavefront” and that “high-resolution images are in fact interference patterns formed from the phase relationships of diffracted beams.” In high-resolution imaging, phase contrast in the image is dominating over amplitude contrast (that is caused by coherent elastic scattering as well as mass-thickness variations), and is achieved by “deliberately introducing particular phase shifts into the electron wave field by suitably defocusing the objective lens” [7, p. 507]. However, the objective lens aberrations limit the range of spatial frequencies (i.e., the point resolution of a TEM) usable for high-resolution imaging [8]. For example, the spherical aberration of the objective lens causes additional phase shifts of the electron waves which increase with increasing spatial frequency depending on the spherical aberration c_s of the objective lens [5, p. 463] and can be compensated in part by adjusting the focus of the lens [5, p. 465]. After the successful implementation of hexapole-type spherical aberration (C_s)-correctors in the late 1990s [8], which were designed based on a technique derived by Rose [9], transmission electron microscopy has taken a further “great step forward”, according to Urban (2008) [7, p. 506], and the value of the point resolution has now decreased to about 50-80 pm [7]. The implementation of chromatic in addition to spherical aberration correction was claimed in 2008 [7,10]. As pointed out

by Haider et al. (2008) [10, p. 168], “for the purpose of an improvement of the resolving power of a TEM, not only the correction of the chromatic aberration has to be considered but in almost the same manner (…) the careful setup of the base instrument is as important as the correction system”, which is accomplished by establishing an overall mechanical and electrical stability of the device. Urban (2008) [7, p. 508] stated further that “the accuracy at which the separation of well-isolated atoms can be measured” has been reported to be already in the range of only a few picometer. H. Rose, M. Haider and K. W. Urban were awarded the Wolf Prize in Physics in 2011 for their pioneering work regarding the development of probe correctors both for spherical and chromatic aberration. However, according to Haider et al. (2008) [10, p. 168], even with an advanced spherical-aberration corrector, “an aberration-free imaging (…) system does not exist”, and “at least residual [incoherent] parasitic aberrations are always present in real systems due to manufacturing tolerances of the optical elements and misalignments.”

The “useful” information of lattice images transferred by the TEM is limited to a certain high spatial frequency (i.e., small lattice distance), “where we can use nearly intuitive arguments to interpret what we see”, according to Williams and Carter (1996) [5, p. 465]. This spatial frequency is defined as the instrumental resolution limit (or point-to-point resolution) [5, p. 465]. This limitation arises because of the lens aberrations and the inadequate setup of the electron optical system resulting in imperfect alignment [10]. The point-to-point resolution of the instrument is defined as the spatial frequency of the first zero in the so-called contrast transfer function (CTF) [5, pp. 463-465].

3.3 References

[1] C. E. Lyman, D. E. Newbury, J. I. Goldstein, D. B. Williams, A D. Romig Jr., J. T. Armstrong, P. Echlin, C. E. Fiori, D. C. Joy, E. Lifshin, and K.-R. Peters (1990). *Scanning electron microscopy, X-ray microanalysis, and analytical electron microscopy: a laboratory workbook*. New York, NY: Plenum Press.

[2] G. Wagner (2006). *Rasterelektronenmikroskopie* [Lecture handout]. Leipzig: Department of Chemistry and Mineralogy, Universität Leipzig.

[3] B. Fultz and J. Howe (2008). *Transmission electron microscopy and diffractometry of materials* (4th ed.). Berlin: Springer.

[4] J. I. Goldstein, C. E. Lyman, D. E. Newbury, E. Lifshin, P. Echlin, L. Sawyer, D. C. Joy, and J. R. Michael (2003). *Scanning electron microscopy and X-ray microanalysis* (3rd ed.). New York, NY: Springer.

[5] D. B. Williams and C. B. Carter (1996). *Transmission electron microscopy: A textbook for materials science*. New York, NY: Plenum Press.

[6] G. Cliff and G. W. Lorimer (1975). Quantitative analysis of thin specimens. *J. Microsc.*, 103 [2], 203-207.

[7] K. W. Urban (2008). Studying atomic structures by aberration-corrected transmission electron microscopy. *Science*, 321, 506-510.

[8] M. Haider, S. Uhlemann, E. Schwan, H. Rose, B. Kabius, and K. Urban (1998). Electron microscopy image enhanced. *Nature*, 392, 768-769.

[9] H. Rose (1990). Outline of a spherically corrected semi-aplanatic medium-voltage TEM. *Optik*, 85, 19-24.

[10] M. Haider, H. Müller, S. Uhlemann, J. Zach, U. Loebau, and R. Hoeschen (2008). Prerequisites for a c_c/c_s-corrected ultrahigh-resolution TEM. *Ultramicroscopy*, 108, 167-178.

4 Experimental Procedure

4.1 Sample Preparation and Annealing

The ceramic samples investigated in the present work were prepared by Benjamin Papendorf in the laboratory of Prof. R. Riedel, Disperse Solids Department, Technische Universität Darmstadt. A number of synthesis papers [1-3] are available on the synthesis of these materials, including any necessary supplementary information such as chemicals that were purchased, vendors, and elemental analyses. In this chapter, however, a brief description of the synthetic procedure is given. Chemical analysis data is taken from the doctoral thesis of Benjamin Papendorf [4], where details regarding the experimental routines used for chemical analysis can also be found. Elemental analyses were performed by Benjamin Papendorf (carbon, nitrogen and oxygen) and by Pascher Laboratories (silicon and hafnium).

Preparation of silicon oxycarbide-HfO_2 nanocomposites (HfO_2/SiHfOC) and annealing [3]. All reactions were performed under argon. To a three-necked 500 mL round-bottomed flask equipped with a mechanical stirrer was added polymethylsilsesquioxane (PMS), previously dissolved in 2-propanol, and stirred for 0.5 h. The mixture was continuously cooled to -78°C. A solution of hafnium tert-butoxide) (Sigma Aldrich, USA) in 2-propanol was added dropwise. The total amount of the hafnium alkoxide added to PMS was 30% by volume. The mixture was stirred vigorously and warmed to room temperature and concentrated under vacuum in a rotary evaporator to give a solid precipitate, which was further evaporated under vacuum for 12 h. The product was ground, transferred into a sealed dessicator and left for 1 day. The dry powder was homogenized by milling for 3 h. For Shaping, samples of the powdery Hf-alkoxide modified polymer were warm-pressed at 180°C, 117 MPa. As-prepared monolithic greenbodies were pyrolyzed under flowing argon employing rather slow heating rates (100 K/h up to 300°C and half the initial value from 300 to 1300°C, just 50 K/h). In order to investigate the volume diffusion of Hf systematically, isothermal annealing experiments were run at 1300°C for 1, 3, 10, 100, and 200 hrs, respectively. Upon annealing, the oven was cooled to 600°C employing a cooling rate of 100 K/h, and slowly cooled to room temperature. An additional annealing experiment (1 h annealing) was run with a significantly higher

heating rate of 600 K/h to avoid prolonged heating times due to the slow heating rates affecting the diffusion of Hf; however, the sample fractured into many small fragments and could not be used for further TEM/EDS analysis. Weight losses upon annealing were calculated with the aid of the weight of a blank sample, prepared using the same procedure as for the annealed samples (3 h annealing). Quantitative analysis was done for a sample pyrolyzed at 1300°C for 3 h. For the SiHfOC ceramic material derived from PMS modified with 10 vol% Hf-tert-butoxide, the ceramic yield is around 81% upon pyrolysis at 1300°C for 3 h [4]. In [4], it is shown that the pyrolytic conversion of Hf-modified PMS is associated with the formation of volatile low-weight hydrocarbons generated upon the decomposition of the precursor promoted by cross linkage (between 127-461°C) as well as ceramization processes (between 650°C-850°C).

Preparation of silicon carbonitride-HfO_2 nanocomposites (HfO_2/SiHfCNO) and annealing [4]. Polysilazane HTT1800 was weighed in a flask and Hf(IV) n-butoxide (30 % by volume) was added under argon. The mixture was stirred at room temperature for 1 h under argon. The flask was placed in a Schlenk tube. The solution was heated to 250°C using a heating rate of 50 K/h and held at this temperature for 3 h. The resulting solid was finely ground and sieved. Powderous samples were warm-pressed into monolithic greenbodies at 41.7 MPa. The as-prepared monoliths were pyrolyzed under flowing argon employing rather slow heating rates, 100 K/h (up to 300°C) and 50 K/h (from 300 to 1300°C), respectively. Isothermal anneals were run under argon at 1300°C for 1, 3, 10, 50, 100, and 200 h, respectively. Upon annealing, the oven was cooled to 600°C employing a cooling rate of 100 K/h, and subsequently slowly cooled to room temperature. When this pyrolysis procedure is followed, pronounced formation of gaseous decomposition products due to cross linkage (between 150-200°C) and ceramization (between 400-750°C) determines the relatively low ceramic yield (53 %) [4].

4.2 Analytical Methods

4.2.1 Scanning Electron Microscopy

Backscattered electron (BSE) imaging was carried out using a Quanta 200F instrument (FEI, Eindhoven, The Netherlands) with field emission electron gun (FEG)

operated at 20 kV. For this purpose, freshly fractured cross sections were prepared and carbon sputtered prior to SEM analysis conducted in high-vacuum mode.

4.2.2 Analytical Transmission Electron Microscopy

Conventional transmission EM in conjunction with analytical EM were performed on a FEI CM20STEM microscope (FEI, Eindhoven, The Netherlands) equipped with a side-entry goniometer, a LaB_6-cathode operated at 200 kV, and an Oxford X-MAX 80 energy-dispersive X-ray spectrometer (EDS) with an ultra-thin window (Oxford Instruments Nanoanalysis, High Wycombe, United Kingdom). A low-background specimen holder with beryllium specimen cup was used.

Thin foils were fabricated by manual grinding, polishing and mounting on a molybdenum grid followed by argon ion sputtering. TEM foils were deliberately not coated with carbon for quantitative EDS analysis. However, prior to HRTEM imaging TEM foils were slightly coated with carbon to minimize charging.

For quantitative analysis by means of EDS, a low beam intensity was necessary to minimize electron beam damage and contamination, which precluded conventional high-resolution TEM investigation. With the specimen tilted about 20° toward the EDS detector, the following operating conditions were used: 200 kV (maximum kV); 300-nm probe size; medium C_2-aperture size (which determines the probe current); objective aperture out; 40 s counting time. Dead time was kept below 30 % for all collected X-ray spectra by exclusively analyzing thin regions of the specimen in close proximity to perforations. The thin foils were stable during irradiation although not coated with carbon.

Quantitative analysis of thin specimens utilized for TEM can be very straightforward, because of the lack of x-ray absorption and fluorescence. Cliff and Lorimer (1975) [5] developed a simple expression for quantitative analysis of thin foils without reference to standards at the time of analysis using k-factors (relative to silicon):

$$\frac{I_{Si}}{I_x} = k\frac{C_{Si}}{C_x} \quad eq.1$$

where I_{Si} and I_x are integrated characteristic X-ray peak intensities (with background subtracted), C_{Si} and C_x are weight fractions of the two relevant elements. The k value is set to 1 for silicon, by convention. K factors for any two elements may be obtained either by direct measurement on standards of known composition, or, in cases where standards are unavailable, by theoretical calculation. The latter method is used in the

quantitative software supplied with the EDS system used in the present work. For multielement quantification, the following integrated characteristic x-ray peaks collected from the specimen above background were used: *Kα* peaks for carbon, nitrogen, silicon and oxygen, and the *Mα* peak for hafnium. The Si*Kα1* peak (1.739 keV, intensity 100 %) and Si*Kα2* peak (1.828 keV, intensity 1.7 %) overlap with the Hf*Mα* peak (1.649 keV, 100%) and Hf*Mβ* peak (1.703 keV, 45%), respectively. The following theoretical k-factors were used: 2.504 (C*K*), 1.000 (Si*K,* by convention), 1.871 (O*K*), and 1.575 (Hf*M*). The given software used a modified version of the simple Cliff-Lorimer ratio method which corrects for absorption of characteristic X-rays.

The Cliff-Lorimer equation has to be corrected if characteristic X-rays are absorbed or fluoresced significantly, according to Lyman et al. (1990) [6, p. 378]. According to [6, p. 378], the equation of the absorption correction factor, ACF, for a simple binary sample AB is given in eq. 2.1 and 2.2:

$$\frac{C_A}{C_B} = k_{AB}\frac{I_A}{I_B}ACF \quad eq.2.1$$

where

$$ACF = \frac{\left[\frac{\mu}{\rho}\right]_A \left[1 - exp\left(\left[\frac{\mu}{\rho}\right]_B \rho t cosec\alpha\right)\right]}{\left[\frac{\mu}{\rho}\right]_B \left[1 - exp\left(\left[\frac{\mu}{\rho}\right]_A \rho t cosec\alpha\right)\right]} \quad eq.2.2$$

where ρ is the specimen density, t is the specimen thickness, α is the X-ray take-off angle, and μ/ρ are the mass absorption coefficients for element A and B X-rays, respectively, absorbed in the specimen. In the HfO_2/SiHfOC and HfO_2/SiHfCNO samples, C*K*, N*K*, and O*K* X-rays are strongly absorbed by silicon present in the samples investigated here and this is observable, since the Si/O X-ray peak area ratio increases as the thickness of the foil increases. Absorption correction was performed, although only very thin areas were chosen for EDS measurements. The absorption correction routine used requires knowledge of specimen thickness and density. For the specimen thickness, an estimated value of 100 nm was chosen (reasonable only in close proximity to perforations). For the density of the HfO_2/SiHfOC bulk material (MK Belsil PMS, Hf/Si ~ 0.06), the value of 2.3 g/cm^3 was utilized, derived from a similar sample (MK Belsil PMS, Hf/Si ~ 0.02 [7]) using the water immersion method (Archimedes` principle). For the density of the HfO_2/SiHfCNO bulk material (HTT 1800, Hf/Si ~ 0.07 [8]), the same value (2.3 g/cm^3)

was used as an estimate, since no experimental data was available in this case. This value is only slightly smaller than experimental densities for related materials (e.g., 2.9 g/cm^3 for HfO_2/SiHfCNO [9]; around 3.3 and 2.6 g/cm^3 for amorphous SiCN with a carbon content below 20 and of 35 at%, respectively [10]). It is important to note that for both investigated materials a general outward trend toward a SiO_2-rich composition (surface-near region) was observed (see chapter 5.3 and 6.3, respectively). The densities of amorphous SiO_2 and cristobalite are 2.1 and 2.3 g/cm^3, respectively [11, p. 156]). The value of 2.3 g/cm^3 is therefore thought to represent a reasonable estimate of the density for both surface-near and bulk regions of both materials investigated here.

4.2.3 Calculation of the Diffusion Coefficient of Hafnium

Wagner (1961) [12], Lifshitz and Slyozov (1961) [13] (LSW) developed a quantitative expression for the dependence of the average particle radius of a dispersed phase AB as a function of time in a multidispersed system of particles homogeneously distributed in a matrix, which often contains an excess of one constituent (A or B) of the dispersed phase AB. The LSW theory is based on thermodynamical considerations regarding the vapor pressure of small spherical particles suspended in a fluid matrix (Gibbs-Thomson equation). Their curvature induces a flux of atoms from the regions of strong curvature to plane surfaces leading to a recession of particles that exhibit a large ratio of surface area to radius. Less curved particles (i.e. larger spherical ones) therefore grow to large sizes. The temporal power-law exponent for the theoretical kinetic equation of LSW is three for volume diffusion-controlled growth [12,13]. Wagner (1961) [12] also published a solution for the other extreme case of interface reaction-controlled coarsening yielding a temporal exponent of 2, though he argued that a combination of both mechanisms is possible, in principle. White and Fisher (1978) [14] showed that for coarsening kinetics a time exponent varying between 2 and 3 can be expected, which was deduced from a theory that involves the transition between interface reaction and diffusion control. Ardell and Ozolins (2005) [15] revisited the problem of crystalline precipitates dispersed in a crystalline matrix when they observed a volume-fraction dependence of the rate constant in the kinetic equation of coarsening in Ni-Al alloys, which is unpredicted by the LSW theory. They stated that, in Ni-Al alloys, the temporal laws of the LSW theory are no longer obeyed.

Wagner (1961) [12] developed the following expression for diffusion-controlled mass transport, under the assumption of local equilibrium at the phase boundary (particle/matrix interface) and quasistationary conditions (i.e. with equilibrium concentration of the solved minor constituent of the dispersed phase and time-invariant particle size distribution):

$$r^3 - r_0^3 = \frac{8\mathrm{D}\gamma\mathrm{c}\Omega^2(t - t_0)}{9RT} \quad eq.3$$

where r is the average particle radius at time t, r_0 is the radius at t = 0 (onset of coarsening), D is the diffusion coefficient, γ is the matrix/HfO_2 interface energy, c is the equilibrium concentration of solved Hf (i.e. the minor constituent of HfO_2) in the volume host matrix, Ω is the molar volume of HfO_2, T is annealing time, R is the gas constant. The variable t_0, if not zero, accounts for establishing the equilibrium concentration. The diffusion coefficient of Hf, D_{Hf}, can be calculated when rearranging eq. 3:

$$D_{Hf} = \frac{9RT(r^3 - r_0^3)}{8c\gamma\Omega^2(t - t_0)}. \quad eq.4$$

The following values of the parameters required in eq. 3 are used: the gas constant R = 8.314 J(K mol)$^{-1}$; the annealing temperature T = 1573 K; a molar volume Ω of HfO_2 of 21.05 cm^3 mol^{-1}, determined from the ratio between the molar mass and the theoretical density of tetragonal-HfO_2 [16] (210.49 g mol^{-1}/10.01 g cm^{-3}). In estimating the interfacial energy for HfO_2/SiHfOC and HfO_2/SiHfCNO interfaces, we drew upon values for related systems. Ushakov et al. (2004) [17] reported an interfacial energy of 0.25 J/m^2 for tetragonal HfO_2/amorphous SiO_2, the value derived by calorimetry, while Varga et. al. (2007) [18] proposed an interfacial energy of approximately 0.5 J/m^2 for graphene/crystalline SiO_2 with constrained bonds at the interface. Shchipalov (2000) [19] reported a high surface energy of 1.56 J/m^2 for cristobalite/amorphous SiO_2. In accordance with the argumentation of Varga et al. (2007) [18], one might expect that cristobalite imposes constraints on the SiO_4^{4-} tetrahedra configuration at the crystalline/amorphous interface, which is consistent with the high interfacial energy reported by Shchipalov (2000) [19]. Accordingly, for internal surfaces that contained cristobalite upon annealing for 10 h in the case of the SiHfOC samples, the value of 0.25 J/m^2 reported for tetragonal HfO_2/amorphous SiO_2 [17] was used as an estimate, since no value for tetragonal/HfO_2/cristobalite was available, while a higher value of 0.5 J/m^2 [18] was used for HfO_2/SiHfOC interfaces

in the bulk with assumed constrained bonds at crystalline/amorphous interfaces. D_{Hf} was also calculated for SiHfCNO, however, in this case only for internal surfaces. As-pyrolyzed HfO_2/SiHfOC and HfO_2/SiHfCNO ceramic samples (i.e., annealed for 1 h at 1300°C) were considered as reference samples to determine r_0, the average particle radius at the onset of particle coarsening, since no major size variation of the HfO_2 precipitates was observed. Accordingly, for HfO_2/SiHfOC, r_0 was 1.5 nm (bulk regions) and 3.3 nm (in close proximity to surfaces). For HfO_2/SiHfCNO, r_0 was 0.8 nm and 2.6 nm near surfaces, respectively. The interface energy, γ, was 0.5 J/m^2 for coarsened HfO_2 particles within the SiHfO(C,N) matrix and 0.25 J/m^2 for coarsened HfO_2 when the matrix was composed of amorphous SiO_2 (in close proximity to surfaces). The concentration of hafnium in the matrix, c_{Hf}, required in eq. 4 was calculated for the two materials (HfO_2/SiHfOC and HfO_2/SiHfCNO) separately, using the corresponding chemical analysis data (see chapters 5.5 and 6.4).

4.2.4 Analytical Method for Modeling Carbon Diffusion Profiles

In collaboration with Dr. J. Rohrer, Department of Materials Science, Technische Universität Darmstadt, the extraction of a diffusion coefficient from measured carbon profiles near internal surfaces was performed here for the first time. This procedure is not yet standardized. Our experimental procedure to obtain a diffusion coefficient is to fit the measured concentration profiles c(x,t) at various times t to an analytical solution to the one-dimensional steady-state diffusion equation [20, p. 22] assuming a diffusion-couple geometry:

$$c(x,t) = \frac{c_{max} + c_{min}}{2} + \frac{c_{max} - c_{min}}{2} erf \frac{x - x_0}{2\sqrt{Dt}} \quad eq.5$$

with the given initial condition, c_{min} and c_{max}, corresponding to the initial concentrations of carbon at the bulk and the surface, respectively. The parameter x_0 denotes the inflection point of the profile. The carbon concentrations in the upper and lower halve of the diffusion couple, c_{min} and c_{max}, respectively, were obtained from mean values of the experimental data points. The parameter D, the diffusion coefficient of carbon, and the initial position of the interface between the diffusion couple, x_0, were optimized. It was also tried, however, to solve the diffusion equation numerically using the following diffusion equation:

$$\frac{\partial c(x,t)}{\partial t} = D(x) \frac{\partial^2 c(x,t)}{\partial x^2} + \frac{\partial D(x)}{\partial x} \frac{\partial c(x,t)}{\partial x} + \Gamma(x). \quad eq.6$$

Here, D is spatially dependent via c(x), and Γ is a localized term describing surface desorption. Using the experimental concentration profile measured after 1 h as initial c(x), this equation is solved numerically for various choices of D and Γ, as the numerical solution can accommodate cases in which D [via D(x)] in the investigated area depends on the local concentration of the diffusing species, or a growing cristobalite phase, or the boundary condition at the surface is a function of time (via Γ), due to a loss of the diffusing species via evaporation.

4.3 References

[1] E. Ionescu, H.-J. Kleebe, and R. Riedel (2012). Silicon-containing polymer-derived ceramic nanocomposites (PDC-NCs): Preparative approaches and properties. *Chem. Soc. Rev.*, 41 (15), 5032-5052.

[2] E. Ionescu, B. Papendorf, H.-J. Kleebe, F. Poli, K. Müller, and R. Riedel (2010). Polymer-derived silicon oxycarbide/hafnia ceramic nanocomposites. Part I: Phase and microstructure evolution during the ceramization process. *J. Am. Ceram. Soc.*, 93(6), 1774-1782.

[3] E. Ionescu, B. Papendorf, H.-J. Kleebe, H. Breitzke, K. Nonnenmacher, G. Buntkowsy, and R. Riedel (2012). Phase separation of a hafnium alkoxide-modified polysilazane upon polymer-to-ceramic transformation- A case study. *J. Eur. Ceram. Soc.*, 32(9), 1873-1881.

[4] B. Papendorf (2012). *Keramische Nanokomposite auf Basis von SiOC/HfO_2 und SiCN/HfO_2: Herstellung und Untersuchungen zum Hochtemperaturverhalten*. (Unpublished doctoral dissertation.) Technische Universität Darmstadt, Darmstadt, Germany.

[5] G. Cliff and G. W. Lorimer (1975). Quantitative analysis of thin specimens. *J. Microsc.*, 103 (2), 203-207.

[6] C. E. Lyman, D. E. Newbury, J. I. Goldstein, D. B. Williams, A. D. Romig Jr., J. T. Armstrong, P. Echlin, C. E. Fiori, D. C. Joy, E. Lifshin, and K.-R. Peters (1990). *Scanning electron microscopy, X-ray microanalysis, and analytical electron microscopy: a laboratory workbook*. New York, NY: Plenum Press.

[7] E. Ionescu, B. Papendorf, H.-J. Kleebe, F. Poli, K. Müller, and R. Riedel (2010). Polymer-derived silicon oxycarbide/hafnia ceramic nanocomposites. Part I: Phase and microstructure evolution during the ceramization process. *J. Am. Ceram. Soc.*, 93(6), 1774-1782.

[8] E. Ionescu, B. Papendorf, H.-J. Kleebe, H. Breitzke, K. Nonnenmacher, G. Buntkowsky, and R. Riedel (2012). Phase separation of a hafnium alkoxide-modified polysilazane upon polymer-to-ceramic transformation – A case study. *J. Eur. Ceram. Soc.*, 32(9), 1873-1881.

[9] K. Terauds, D. B. Marshall, and R. Raj (2013). Oxidation of polymer-derived HfSiCNO up to 1600°C. *J. Am. Ceram. Soc.*, 96(4), 1278-1284.

[10] S. Chattopadhyay, L. C. Chen, S. C. Chien, S. T. Lin, and K. H. Chen (2002). Bonding characterization, density measurement, and thermal diffusivity studies of amorphous silicon carbon nitride and boron carbon nitride thin films. *J. Appl. Phys.*, 92(9), 5150-5158.

[11] M. Okrusch and S. Matthes (2009). *Mineralogie* (8th ed.). Berlin, Germany: Springer.

[12] C. Wagner (1961). Theorie der Alterung von Niederschlägen durch Umlösen (Ostwald-Reifung). *Z. Elektrochem.*, 65, 581-591.

[13] M. Lifshitz and V. V. Slyozov (1961). The kinetics of precipitation from supersaturated solid solutions. *J. Phys. Chem. Solids*, 19(1-2), 35-50.

[14] R. J. White and S. B. Fisher (1978). The precipitation and growth kinetics of γ′ in Nimonic PE16. *Mater. Sci. Eng.*, 33(2), 149-157.

[15] A. J. Ardell and V. Ozolins (2005). Trans-interface diffusion-controlled coarsening. *Nat. Mater.*, 4, 309-316.

[16] C. E. Curtis, L. M. Doney, and J. R. Johnson (1954). Some properties of hafnium oxide, hafnium silicate, calcium hafnate and hafnium carbide. *J. Am. Ceram. Soc.*, 37(10), 458-465.

[17] S. V. Ushakov, A. Navrotsky, Y. Yang, S. Stemmer, K. Kukli, M. Ritala, M. A. Leskelä, P. Fejes, A. Demkov, C. Wang, B.-Y. Nguyen, D. Triyoso, and P. Tobin (2004). Crystallization in hafnia- and zirconia-based systems. *Phys. Stat. Sol. B*, 241(10), 2268-2278.

[18] T. Varga, A. Navrotsky, J. L. Moats, R. M. Morcos, F. Poli, K. Mueller, A. Saha, and R. Raj (2007). Thermodynamically stable SiOC polymer-like amorphous ceramics. *J. Am. Ceram. Soc.*, 90(10), 3213–3219.

[19] Y. K. Shchipalov (2000). Surface energy of crystalline and vitreous silica. *Glass Ceram.*, 57(11-12), 374-377.

[20] Y. Zhang (2010). Diffusion in minerals and melts: Theoretical background. In Y. Zhang and D. J. Cherniak (Eds.), *Diffusion in minerals and melts* (pp. 5-59). Chantilly, VA: The Mineralogical Society of America.

5 HfO_2/SiHfOC Ceramic Nanocomposites

5.1 Motivation

The HfO_2/SiHfOC samples studied in the present work are synthesized from mixtures of a hafnium alkoxide and a macromolecular precursor (PMS), the latter containing silicon-oxygen ring structures and additional functional carbohydrate groups. The precursor mixtures were cross-linked into polymers and converted into ceramics upon pyrolysis at temperatures between 900°C and 1300°C. A previous study [1] on these materials using FTIR and NMR provide insights into the reactions between the hafnium-alkoxide and the functional moieties of the Si-based precursor during processing and subsequent pyrolysis. In this study, the amount of hafnium alkoxide added to PMS ranged between 10 and 30 vol%. In particular, Si-O-Hf bonds were monitored in the hafnium-alkoxide modified precursor material. Furthermore, ^{29}Si- und ^{13}C NMR reveal the evolution of a quaternary SiHfOC amorphous network with no indication for phase separation upon pyrolysis at rather low temperatures (~800°C). At higher pyrolysis temperature, in the range between 900–1100°C, however, phase separation takes place, as indicated by ^{29}Si-NMR showing the evolution of binary phases, predominantly silica and silicon carbide. According to [1], silica forms as a result of structural rearrangement reactions and cross linking reactions within the alkoxide modified network that also promote the precipitation of hafnia (HfO_2). The later argument is promoted by HRTEM investigations on the material pyrolyzed at 900°C, showing strong variations in contrast which are attributed to the segregation of a Hf-containing phase (see Figure 3), although no clear evidence for the possible phase separation within the SiOC matrix can be drawn from these HRTEM images. As can be seen in Figure 3 (b), HRTEM imaging reveals the typical phase contrast of amorphous materials without distinction of the various amorphous domains, as indicated by NMR. Apart from binary phases, early formation of graphite-like carbon is observed in as-pyrolyzed samples, as detected by ^{13}C NMR, which was also noticed by the black colour of the materials upon thermal annealing. Upon pyrolysis at 1100°C, the presence of crystalline HfO_2 nanoparticles within the still amorphous SiCO matrix in the bulk of the sample is revealed by HRTEM (see Figure 4 (a)).

There remains some ambiguity regarding the crystallinity of the HfO_2 precipitates, as the HRTEM image shown in the inset in Figure 4 (a) reveals a few lattice fringes,

while in the corresponding electron Chemical analysis showed a total amount of hafnium of 13.7 wt% for this sample [1]. The HRTEM results are consistent with results of Ushakov et al. (2004) [2] who reported on the formation of the tetragonal hafnia polymorph from amorphous sol-gel derived hafnia/silica samples heat treated well below 1100°C. Ushakov et al. (2004) [2] also found that the crystallization temperature for hafnia increased from 743°C to 1006°C with crystallite size decreasing from 6 to 3 nm and increasing silica content in the matrix. It is important to note here that, apart from finely dispersed hafnia nanocrystals within the bulk SiHfOC matrix, an unexpected variation in the hafnia crystallite size was observed for the first time [3]. In Figure 4 (b), local coarsening of hafnia crystallites near an internal surface (arrow) generated upon cracking is shown. As can be seen here, coarsened hafnia particles are well-crystallized, as sharp diffraction spots are clearly observed in the corresponding electron diffraction pattern (inset in Figure 4 (b)). Preliminary EDS analysis showed that the observed coarsening of hafnia precipitates is related to a silica-rich matrix in close proximity to the cracks that formed within the interior of this sample during pyrolysis.

The bulk microstructure of an as-pyrolyzed HfO_2/SiHfOC material pyrolyzed at 1300°C, which had a similar composition (13.8 wt% hafnium [1]) relative to the sample pyrolyzed at 1100°C, is shown in Figure 5.

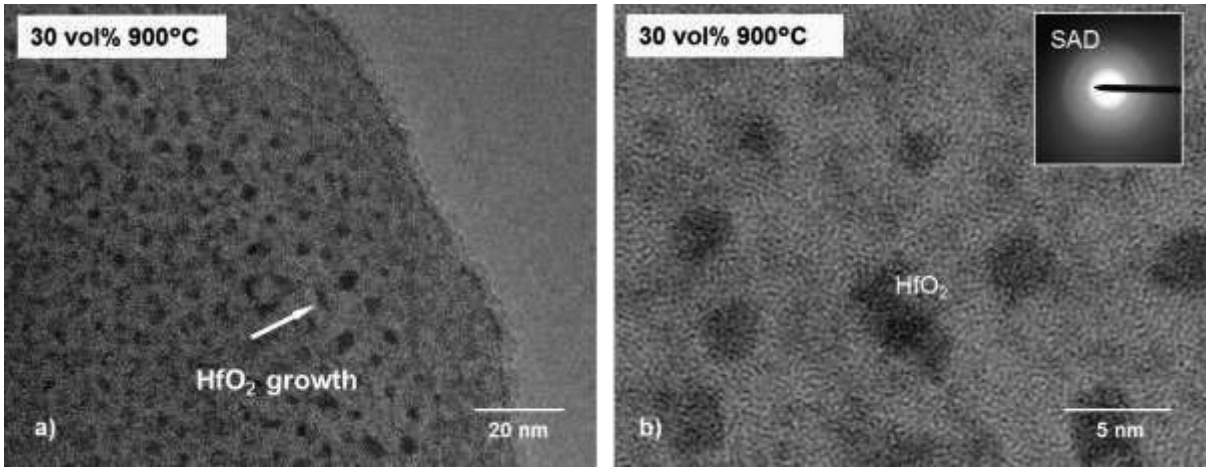

Figure 3: TEM bright-field image (a) and high-resolution TEM image (b) of Hf-rich regions within the amorphous matrix of the as-pyrolyzed HfO_2/SiHfOC material pyrolyzed at 900°C. Hf-rich regions appear darker due to the higher absorption contrast of Hf as compared with the silicon-based matrix. The proportion of Hf-alkoxide being added to the precursor was 30 % by volume. Images courtesy of H.-J. Kleebe [not published].

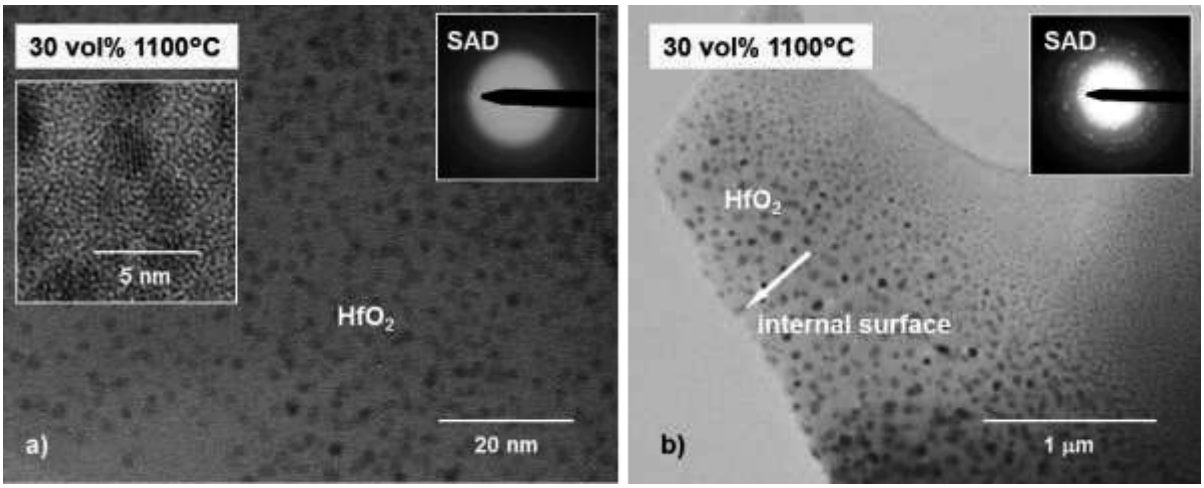

Figure 4: High-resolution TEM images of (a) nanocrystalline hafnia precipitates within the bulk of an as-pyrolyzed HfO_2/SiHfOC material pyrolyzed for 3 h at 1100°C, while in (b) the pronounced coarsening of hafnia precipitates within an area near a microcrack is shown. The marked increase of precipitate size when comparing bulk and surface-near regions is associated with an increase in crystallinity of the hafnia precipitates, as can be seen in the corresponding SAD patterns in (a) and (b), respectively. Images in (a) courtesy of H.-J. Kleebe [1].

The well crystallized tetragonal hafnia precipitates (t-HfO_2) dispersed within a homogeneous SiOC matrix are about 5 nm in diameter and obey spherical shape. Apart from hafnia nanoparticles, the HRTEM image in Figure 5 (b) shows a rather low phase contrast typical for amorphous materials. The TEM bright-field images shown in Figure 6 give a further example of the local particle size variation within a silica-rich matrix in surface-near regions, however, in this case, the sample was pyrolyzed at 1300°C. The precipitates reach an average size of 20 nm, as determined by TEM image analysis from a large number of particles (559), a factor of four larger as compared with the size of the precipitates within bulk regions.

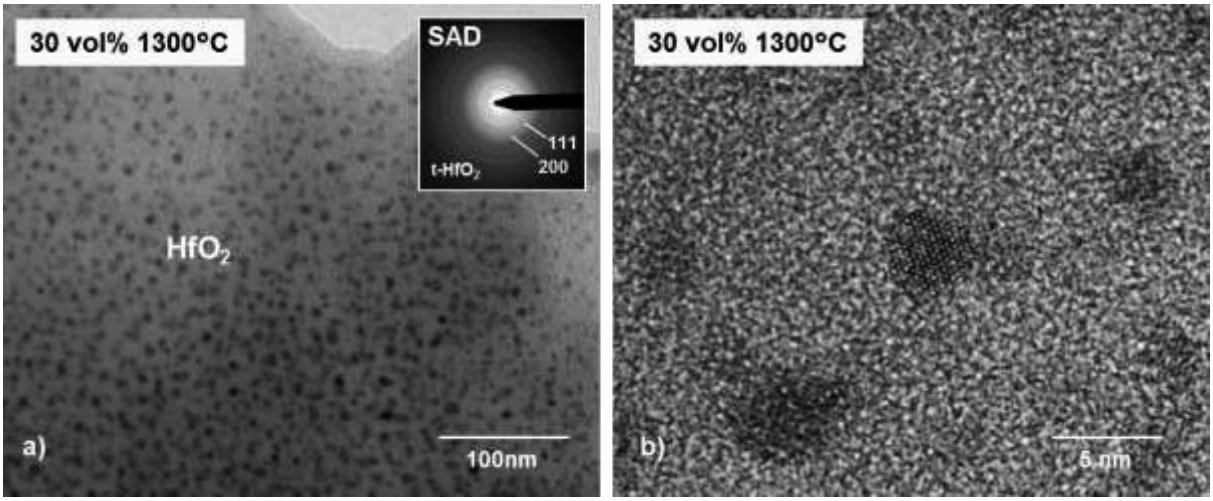

Figure 5: TEM bright-field image (a) and high-resolution TEM image (b) of the microstructure observed in the bulk of an as-pyrolyzed HfO_2/SiHfOC material pyrolyzed for 3 h at 1300°C. Well-crystalline precipitates of tetragonal hafnia are shown.

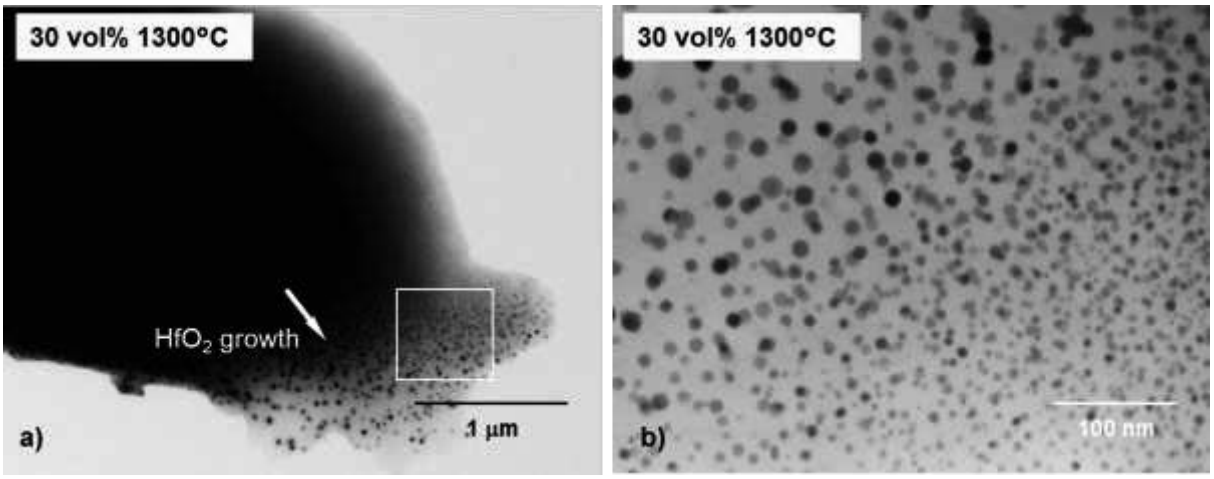

Figure 6: TEM bright-field images of the overall microstructure near an internal surface of an as-pyrolyzed HfO_2/SiHfOC ceramic. In (b), a magnified image of the boxed region shown in (a) is given which depicts a locally pronounced particle coarsening related to a silica-rich matrix.

The backscattered electron images of this sample shown in Figure 7 reveal such a variation in HfO_2 particle size near microcracks. It can be seen that, along the microcracks, channels are typically aligned. Note that the Z-contrast in Figure 7 (b) obtained from a thin foil prepared from the monolithic sample is slightly enhanced as compared to the image shown in (a) obtained on a fracture surface of the same sample, because, in the case of the thin TEM foil in the SEM, the BS electrons come only from the reduced sample volume, giving less remote scatter such as from the electron diffusion zone within a bulk specimen.

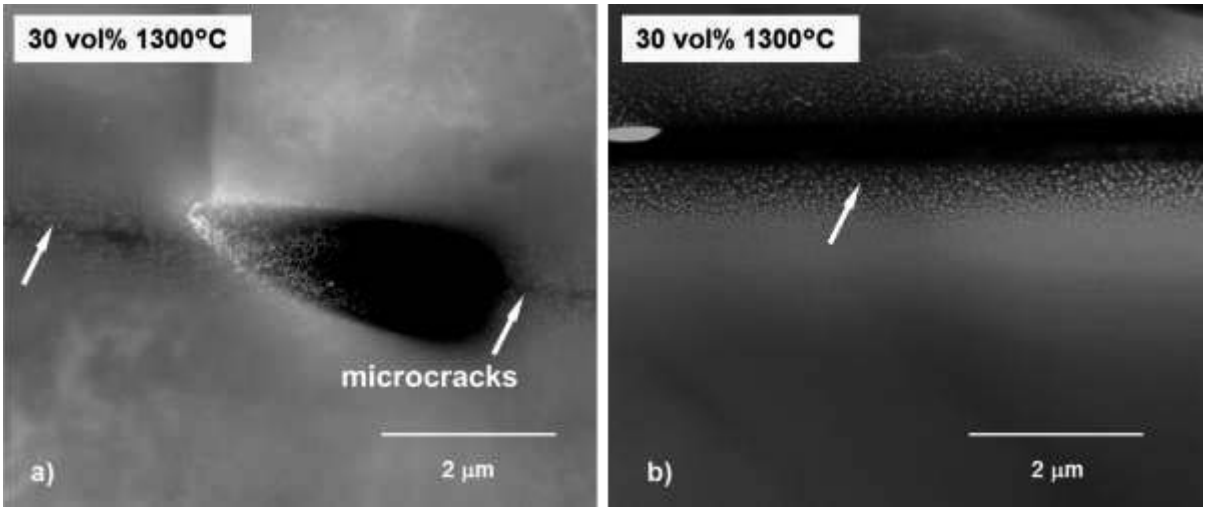

Figure 7: Backscattered electron micrographs (SEM) of a fracture surface of a monolithic HfO_2/SiHfOC nanocomposite pyrolyzed for 3 h at 1300°C that contains microcracks (arrows) which are typically associated with pore channels, while in (b) an area of a polished thin foil prepared from the same material is shown. The thin foil in (b) reveals the coarsening of hafnia precipitates near the crack.

In practice, processing of dense polymer-derived ceramic monoliths is in general difficult, owing to the high volume shrinkage and density change during pyrolytic conversion of the polymer precursor to a ceramic material [1,4-6]. Moreover, the typically pronounced evolution of gaseous decomposition products during pyrolysis can cause the built-up of high gas pressures within the bulk of the ceramics and thus may lead to local microcracking [5]. Apart from the internal surfaces related to microcracks and pore channels observed in the as-pyrolyzed samples, the formation of a continuous silica-rich outer surface layer was also typically observed. These findings point to the decomposition of the mixed precursor polymer during pyrolysis with concomitant degassing of decomposition products, which is consistent with the corresponding thermogravimetry data [1,7].

It is important to emphasize that this unexpected observation of a coarsening of HfO_2 precipitates was observed in all hafnium-modified samples, independent of annealing temperature. Understanding the evolution of this particular microstructure variation of annealed polymer-derived HfO_2/SiHfOC ceramic nanocomposites via transmission electron microscopic characterization is the main focus of the present work. In the following, the results obtained from local transmission electron microscopy (TEM) are presented and discussed. A series of annealed polymer-derived HfO_2/SiHfOC ceramic nanocomposites were systematically investigated**.**

5.2 Microstructure Characterization

Microstructure characterization of annealed HfO_2/SiHfOC ceramic nanocomposites was performed via transmission electron microscopy (TEM) in conjunction with scanning electron microscopy (SEM) and local chemical analysis via energy-dispersive X-ray spectroscopy (EDS). Figure 8 depicts high-resolution TEM images of HfO_2 particles observed within bulk regions of the samples annealed for 1 h at 1300°C, while in Figure 9, the microstructure near an internal surface is shown. In particular, no marked difference in size of the hafnia precipitates among bulk and surface is observed. Figure 9 (b) shows a high-resolution TEM image of nearly spherical hafnia precipitates with a diameter of approximately 7 nm, in this case close to an internal surface of the same sample (1 h). In bulk regions of the materials, the hafnia particle size did only increase by a factor of 1.8 after annealing for 200 h (see also Figure 31 in the Appendix).

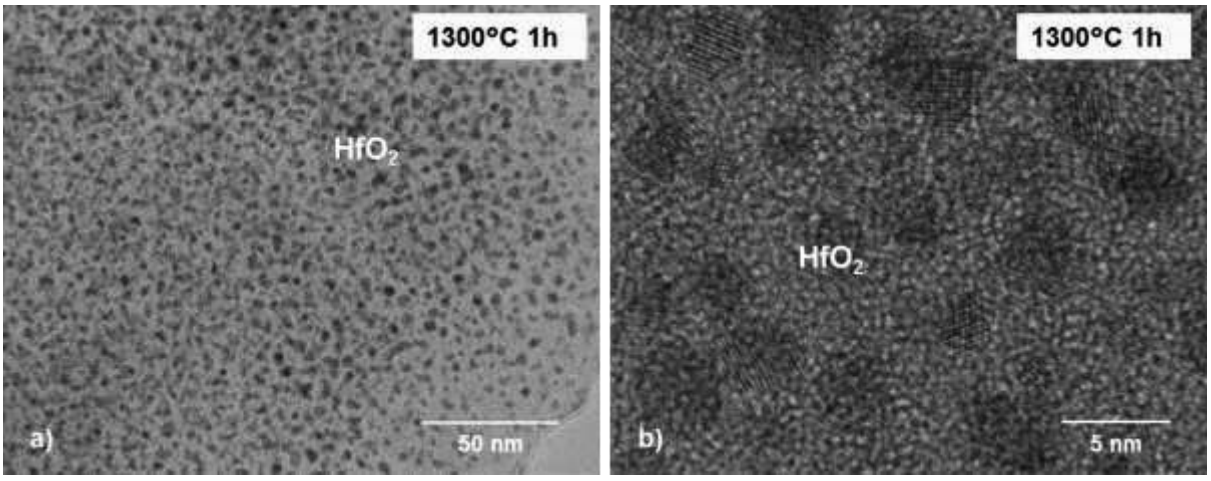

Figure 8: (a) Bright-field TEM and (b) high-resolution TEM images of crystalline hafnia precipitates within the bulk of the as-pyrolyzed HfO_2/SiHfOC sample. On average, the diameter of the precipitates is approximately 3 nm.

Therefore it can be concluded that the diffusion of hafnium throughout the amorphous bulk matrix is rather sluggish, as will also be addressed below in chapter 5.5. At the early stages of isothermal annealing (i.e., from 1 to approximately 5 h), the amorphous nature of the matrix is preserved. However, upon longer heat treatment exceeding 5-10 h, surface crystallization of cristobalite was observed in parallel with pronounced HfO_2 growth when moving from the bulk toward internal surfaces (see Figure 10). While the average particle size increases with annealing time, the particle volume fractions determined from the TEM images remain essentially constant (within the error) including bulk and surface-near regions (mean 2.6 vol%, Table 3). The error of the calculated volume fractions is related to the uncertainty in the assumed constant TEM foil thickness.

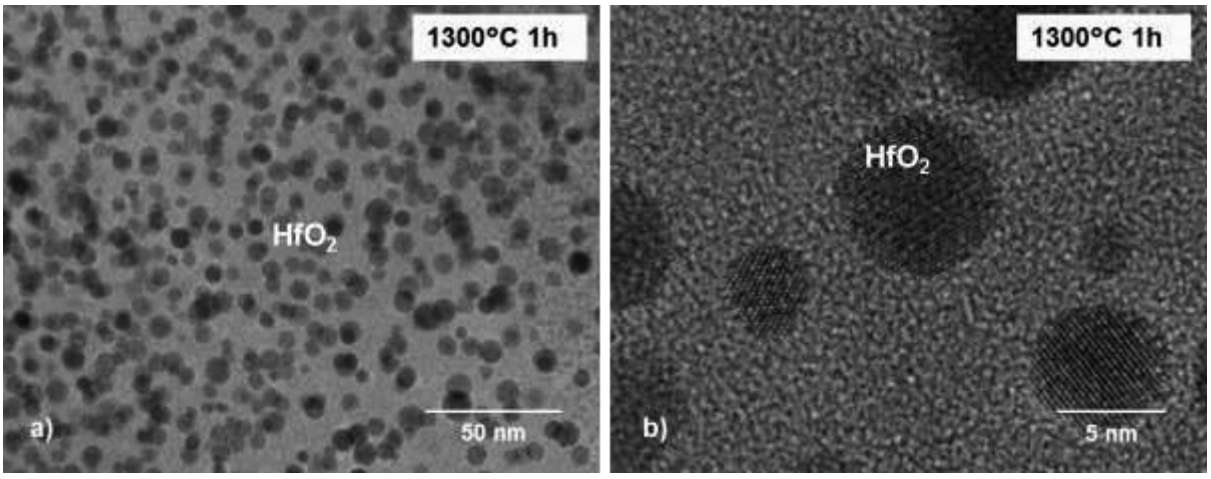

Figure 9: (a) Bright-field TEM and (b) high-resolution TEM images of the corresponding microstructure near a microcrack of the as-pyrolyzed HfO_2/SiHfOC sample with a mean diameter of approximately 7 nm.

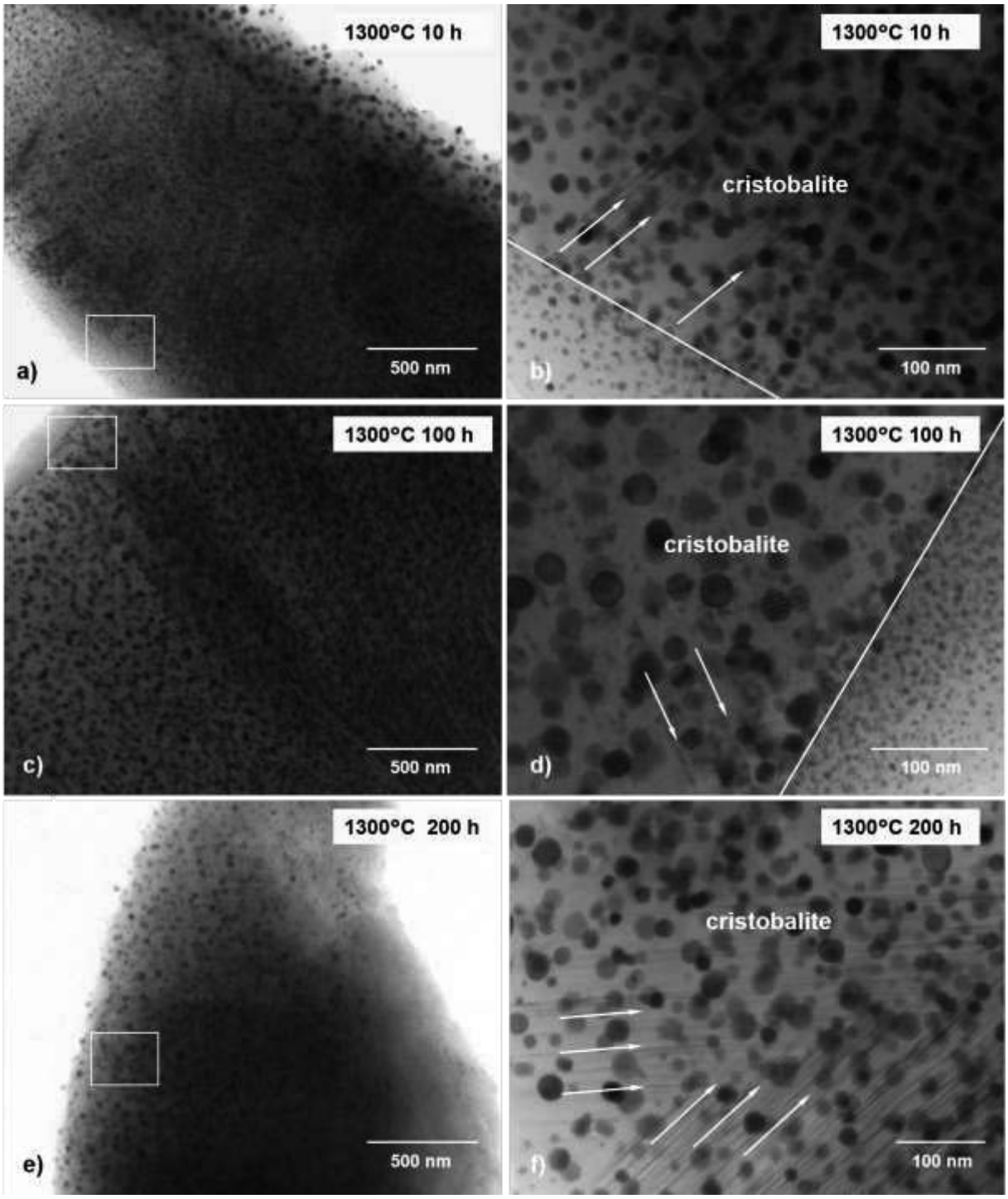

Figure 10: TEM bright-field images of (a), (c), (e) the overall microstructure of the annealed HfO_2/SiHfOC nanocomposites. In (b), (d), and (f), magnified images of areas within and close to the cristobalite growth zone are depicted. The faint lines in (b), (d), and (f) (indicated by arrow) originate from defects in cristobalite. Withers et al. (1989) [8] showed that edge-on planar defects in low-cristobalite are responsible for those characteristic striations in bright-field images. In (b) and (d), solid lines mark the location of the projected interface between the cristobalite growth zone and HfO_2/SiHfOC within the imaged areas.

Although the overall particle dispersion in bulk regions was rather homogeneous, the increase in HfO_2 particle size with time was quantified for both bulk and surface by measuring the size of the hafnia particles from numerous TEM images. To obtain the

mean particle size, between 200 and 450 particles were measured for each sample and each area (bulk versus internal surface). In Figure 11 and Figure 12, the corresponding particle size distributions (PSDs) for bulk and surface-near areas, respectively, are shown. The experimental PSDs for bulk regions are symmetrical, which is not in accordance with the theory of coarsening of Lifshitz and Slyozov (1961) [9] and Wagner (1961) [10]. A slight broadening of the distributions shown in Figure 11 was observed with time, which is also not predicted by LSW [9,10]. The LSW theory predicts time-invariant and asymmetric PSDs for both diffusion- and interface-controlled coarsening of spherical precipitates in an uniform fluid matrix after termination of the reaction that leads to the formation of the microstructure and assumes the ideal limit of zero volume fraction (see also chapter 4.2.3). It should be noted that Wagner (1961) [10] predicted a broader PSD, as compared to the case where coarsening is solely diffusion-controlled, for the case when the solubility of the particles into the matrix or the precipitation of the solute onto the particle surfaces is slower than diffusion through the matrix (interface reaction-controlled process). In an empirical study, Weinbruch et al. (2006) [11] reported that the experimentally observed PSDs of coarsened crystalline lamellae in clinopyroxene, which obeyed the prediction of time invariance, were broader and more symmetric than the theoretically predicted one derived by LSW. In the same study [11], it was shown that the data obeyed the predicted cubic dependence of the average radius on time (diffusion control), according to the classical LSW theory, while the broader size distribution was sufficiently described by the theory derived by Ardell (1972) [12], who investigated a volume fraction modification to the LSW theory for diffusion control. He predicted a broader size distribution for coarsening systems showing precipitate volume fractions in the range of 0.5 to 5%. In our case, the HfO_2 particle volume fraction is approximately 2.6% and, therefore, the finding is in accordance with the theoretical predictions of Ardell (1972) [12]. It should be noted that the theories of LSW [9,10] and Ardell [12] strictly apply only to the case of an isotropic matrix. However, in the HfO_2/SiHfOC samples investigated here, a graphite-like carbon phase evolves and segregates within the matrix upon annealing [1]. This segregated carbon phase is thought to cause local stagnation of the coarsening process of HfO_2 precipitates, since it acts as a diffusion barrier [13, p. 184]. Hence a change from diffusion control to interface control cannot be completely ruled out. Indeed, the broader size distribution observed upon extended annealing time (see Figure 11) is

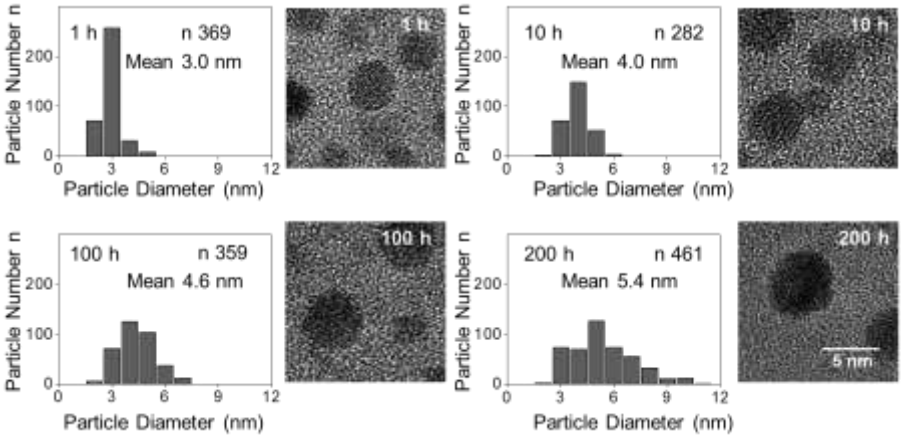

Figure 11: Particle size distributions (size interval: 1 nm, ordinate: particle number n is also indicated) and corresponding high-resolution TEM images of HfO_2 nanoparticles (right) in bulk regions of the HfO_2/SiHfOC nanocomposites annealed for 1 to 200 h.

in accordance with predictions of the classical LSW theory for interface-controlled coarsening [10]. Moreover, a pronounced variation of precipitate size up to one order of magnitude was observed upon extended annealing (i.e., from 10 to 200 h) within cristobalite typically in regions near the investigated internal surfaces and is reflected in the broad size distributions shown in Figure 12, which is not consistent with theoretical predictions for coarsening [10-12]. A possible explanation for this observed broadening might be fast diffusion along grain boundaries in cristobalite, which were typically observed via TEM (see the defect structure depicted in Figure 10 (b,d,f)). Grain boundary diffusion is generally by several orders of magnitude faster than diffusion in the lattice [14, p. 921] and hence would dominate the coarsening of HfO_2 in close vicinity to the grain boundaries in cristobalite.

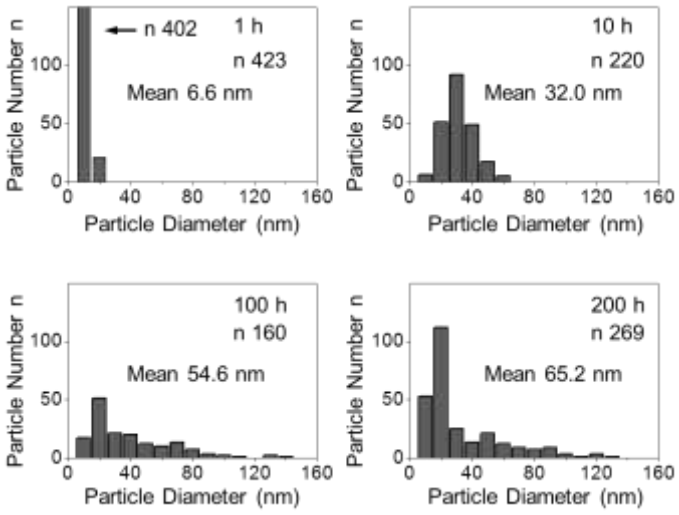

Figure 12: Particle size distributions for HfO_2 in close proximity to internal surfaces (total particle number, n, is indicated). Please note that in Figure 11 a size interval of only 1 nm was used, whereas a size interval of 10 nm is used here.

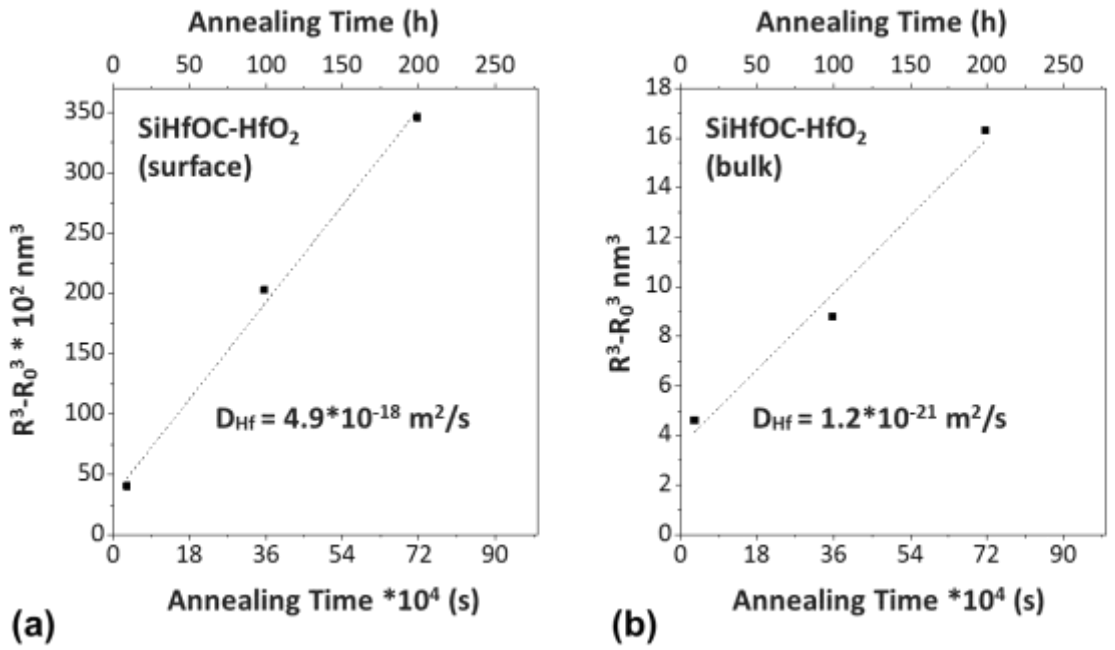

Figure 13: Diagram of the cubed average particle radius as a function of annealing time. Data to the left correspond to the internal surface, while the bulk radii are given on the right. The different slopes are a consequence of the variation in diffusion coefficient of Hf by three orders of magnitude (see also chapter 5.5).

Figure 13 reveals the corresponding graphic representation of the growth process via volume diffusion-controlled coarsening, according to Wagner (1961) [10], within (a) regions in close proximity to internal surfaces and (b) the bulk. In Figure 13, it becomes obvious that a linear dependence of the cubed average particle radius on time is generally obeyed. However, it should be noted that a change from diffusion control (cubed average particle radius, Figure 13) to interface control (squared average particle radius, not shown) with time can still not be excluded from the data.

5.3 Origin of the Pronounced HfO_2 Particle Size Variation

The observed variation in average HfO_2 particle size within bulk regions and surface-near regions was assumed to be a consequence of local chemical changes. Therefore, the relative local overall composition (in mole fractions) for bulk regions and areas close to internal surfaces were analysed by quantitative EDS analysis. As can be seen in Table 1, a pronounced overall difference in composition between bulk and surface is obtained, with the exception of a constant local hafnium content. In all samples, a pronounced drop in carbon content was monitored near internal surfaces, as depicted in the corresponding carbon profiles shown in Figure 14. Please note that the depth profiling (i.e. point-by-point measurements) on the TEM foils starting at

internal surfaces was performed on areas parallel to the irregular perforation edges in the foils generated during Ar thinning to avoid strong X-ray absorption effects with increasing specimen thickness. This irregular thin foil geometry as well as, in particular, the presence of cracks[3] underneath the cristobalite growth zone (shaded region in the profiles in Figure 14) often precluded a continuous depth profiling perpendicular to the edge into the bulk, which is responsible for the relatively large scatter among the data plotted in Figure 14. Note that within the C-depleted regions, a gradual growth of hafnia precipitates occurs being most pronounced in close proximity to the internal surfaces of the annealed HfO_2/SiHfOC samples (at zero in the graphs shown in Figure 14), due to the marked increase in Hf diffusivity, as is addressed below. Within the areas that contain a local carbon content of approximately half the amount of that in bulk regions (see Figure 14, the position of the inflection points of the carbon profiles, x_0), only a slight increase in mean precipitate size as compared with bulk regions is observed (see also Figure 31 in the Appendix).

Table 1: EDS/TEM compositions of annealed monolithic HfO_2/SiHfOC ceramics from X-ray peak intensities (Cliff-Lorimer method).

time (h)		C (at%)*	O (at%)*	Si (at%)*	Hf (at)*
1	surface (4)	2.4	67.5	28.7	1.4
	bulk (15)	22.4±1.5	53.2±1.5	23.3±0.6	1.1±0.1
3	surface (3)	1.9	66.2	30.6	1.4
	bulk (7)	21.8±1.5	53.9±1.2	23.2±0.6	1.1±0.1
10	surface# (4)	2.9±0.5	69.0±1.9	26.6±1.5	1.4±0.1
	bulk (16)	21.4±1.7	54.7±1.3	22.7±0.7	1.1±0.1
100	surface# (6)	2.7±0.4	64.9±3.1	30.8±2.8	1.6±0.3
	bulk (34)	27.7±2.5	47.8±2.1	22.7±0.9	1.8±0.2
200	surface# (9)	2.1±0.5	64.3±2.5	31.8±2.7	1.8±0.2
	bulk (11)	22.6±1.6	54.0±1.1	22.4±0.7	0.9±0.1

* All values are means calculated from multiple point analyses (±1 σ) with the number of single measurements indicated in parentheses.
# Measurements were performed within the cristobalite growth zone.

[3] Cracks underneath the cristobalite growth zones were most likely formed upon cooling after the annealing experiment due to the pronounced misfit of the thermal expansion coefficient among cristobalite [15] and SiHfOC [7].

Interestingly, a marked increase in the coarsening rate is observed where the local carbon content is below a threshold value of approximately 6 at% (denoted surface in Table 1), as deduced from the measured carbon profiles. EDS data reveal a small fraction of carbon even close to the internal surface (Table 1 and Figure 14). This residual carbon detected is thought to be a result of a two-step process: (i) the phase separation process of SiOC: 2 SiOC => SiO_2 + SiC + C followed by (ii) the reduction of silica (cristobalite) by carbon: SiO_2 + 3C => SiC + 2CO. Thus, the detected remaining low carbon volume fraction in proximity to internal surfaces is a consequence of the intrinsic C/SiC formation upon thermal anneal.

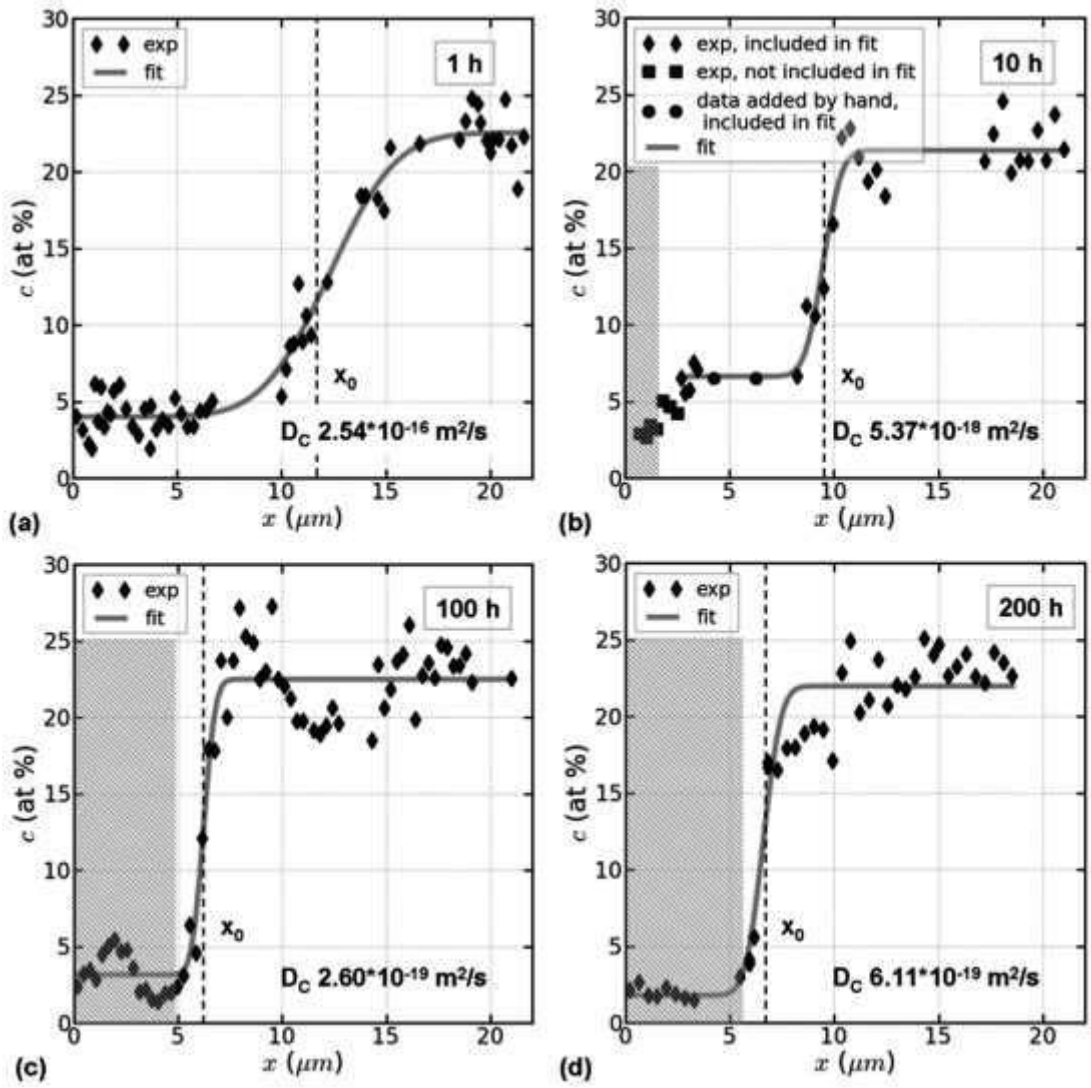

Figure 14: EDS data of the local carbon content in annealed HfO_2/SiHfOC nanocomposites (1300°C, annealing times indicated in insets). The data is fitted to an error function for the diffusion couple geometry, based on which D_C, the diffusion coefficient of carbon, was calculated. Note that x_0 refers to the inflection point of the diffusion couple. The shaded regions to the left indicate the thickness of the formed cristobalite layer. The overall contents for the other constituents (i.e. Si, O, Hf) are given in Table 1. Electron beam spot size for EDS measurements was 300 nm in diameter.

It can be excluded that the Hf-alkoxide-modification of the starting precursor is responsible for the C-depletion monitored in the SiOC matrix. HfO_2 precipitation is already completed at approximately 900°C. Therefore, the observed carbon depletion near internal surfaces is an independent process occurring parallel to the HfO_2 particle growth. Furthermore, the isothermal annealing experiments were performed in inert atmosphere and, therefore, the reaction of oxygen with the samples (oxidation) resulting in a silica-rich overgrowth can also be excluded. The growth of a silica layer during the oxidation of polymer-derived ceramics in general obeys a parabolic rate law [16] that can be ruled out in the case of the samples investigated.

Measured carbon concentration profiles near internal surfaces suggest the diffusion of C species out of the samples, generating the C-depleted SiHfO(C) surface layer. In addition, a continuous weight loss was monitored by weighing samples before and after annealing at 1300°C in argon, suggesting the loss of volatile species during annealing. The mass loss after 10 h was 18.3 % (relative to the warm-pressed green body). Further annealing at 1300°C resulted in an additional mass loss of 1.3 wt% after 100 h and 2.4 wt% after 200 h. The loss of organic volatiles is a possible (though hypothetical) explanation for the C-depletion of the amorphous matrix located near small pore channels and microcracks, which is consistent with the measured weight loss.

The mean bulk composition for all annealed samples from EDS/TEM measurements and the chemical analysis data for a sample pyrolyzed at 1300°C prepared from the same precursor material are given in Table 2. The total amount of carbon determined by chemical analysis does not agree with the local carbon content determined by EDS within experimental error. The quantification results obtained using EDS bear a systematic error for several reasons: (i) theoretical k-factors were employed which were fed into the computer, and (ii) the absorption correction applied (see Experimental Section) requires knowledge of the sample thickness and (iii) assumes a constant density of the specimen. The absorption correction is based on strong X-ray absorption by silicon depending on the thickness of the specimen. Hence, an overestimation of the specimen thickness would induce overestimated contents for carbon, nitrogen and oxygen, respectively, and vice versa. However, the discrepancy between the quantification results shown in Table 2, in particular for the amount of carbon, is also a consequence of the local vs. integral measurement rather than related to systematic errors. The chemical analysis routine yields an average overall

composition of the sample without distinction between surface and bulk regions. Given the pronounced depletion of carbon in regions near surfaces compared to bulk regions (see Table 1 and Figure 14), the data obtained by chemical analysis, given in Table 2, may underestimate the local carbon content of the investigated sample.

Table 2: Results of quantification using different methods.

method	**at% C**	**at% O**	**at% Si**	**at% Hf**
EDS-TEM (local)[#]	22.8±3.1	53.3±3.4	22.8±0.7	1.2±0.3
chemical analysis (integral) [1]*	14.8	53.2	30.2	1.8

[#] All values are means derived from bulk regions of 5 individual samples (1, 3, 10, 50, 200 h). The data of each individual sample used are given in Table 1.
* Single measurements were carried out on an as-pyrolyzed HfO_2/SiHfOC sample pyrolyzed for 3 h at 1300°C.

5.4 Calculation of the Diffusion Coefficient of Carbon

In order to estimate carbon diffusivities from the measured concentration profiles c(x,t) at various times t, the data were fitted to a diffusion couple using eq. 5, chapter 4.2.4. The solid lines in the graphs shown in Figure 14 (a) through (d) represent the fits to eq. 5, an error function, based on which the carbon diffusivity, D_C, was calculated. Please note that the approximate analytical solutions to the traditional diffusion couple equation assumes a couple of two amorphous phases on both sides (amorphous SiHfOC) but with initially different carbon content, which is satisfied for the data shown in Figure 14 (a), but not for the data in (b), (c), and (d), respectively. For the three later cases (i.e. the samples annealed for 10 h, 100 h, and 200 h), the analytical solution neglects the possible effect of the observed change in microstructure across the couple, with the advent of a cristobalite matrix in the surface-near region (left from the inflection point) for longer annealing times exceeding approximately 5 h.

It was also tried, however, to solve the diffusion equation numerically using eq. 6, chapter 4.2.4). The simulated profile always flattens, whereas the measured profiles remain steep (Figure 30, Appendix). Since the resulting simulated profiles did not even qualitatively agree with the measured ones, the diffusion couple (eq. 5) was used here for quantitative estimates of D_C. Although the more restrictive traditional analytical solution used here is also widely used in the literature, the simplifying assumptions of this analytical solution may result in a systematic error in the obtained diffusion coefficient [17, p. 65].

It should be noted that the thickness of the carbon-depleted zone (as indicated by the inflection point x_0 in Figure 14) decreases with increasing annealing time; a rather unexpected observation. This finding could be explained by varying onsets times of cracking determining the onset time of the subsequent degassing period during pyrolysis. Furthermore, the measured profiles remain steep even upon prolonged annealing. A reasonable qualitative assumption can be made that the outward diffusion (desorption) through the cristobalite layer of evolving CO (the decomposition product of the carbothermal reduction of cristobalite; $SiO_2 + 3C \Rightarrow SiC + 2CO$) is in fact slower than the overall carbon diffusion within the amorphous bulk, resulting in the observed shift of the inflection point, x_0, of the carbon profile.

While the calculated diffusion coefficients upon annealing for 10, 100, and 200 h are considered comparable, varying between $5.37*10^{-18}$ and $2.60*10^{-19}$ m^2/s, the value obtained for 1 h is much higher with $2.54*10^{-16}$ m^2/s. The reason for this discrepancy is still unknown. Initially it was assumed to be a consequence of the slow heating rate of 100 K/h employed. Heating with 100 K/h to 1300°C leaves the sample at temperatures, where diffusion starts to be effective (approximately above 800°C) not only for 1 h but for additional 5 h. Recalculating D_C (t_0 = 1h) with an “effective” annealing time of 6 h for this particular carbon diffusion profile did, however, not change the order of magnitude of the diffusion coefficient.

Most species in the ternary systems SiOC and SiCN show diffusivities on the order of 10^{-21} m^2/s [18-20]. The diffusivity of silicon is only moderately affected by carbon incorporation into SiO_2, since the diffusion coefficient of Si in amorphous Si-rich SiOC [18] was within the range of the Si diffusion measured for vitreous silica [19]. A similar behaviour was shown for SiCN with a nearly identical value for the Si diffusivity of $5*10^{-21}$ m^2/s [20]. Moreover, the diffusivity of Si in amorphous SiCN was close to the value of nitrogen diffusion in amorphous silicon nitride with $3*10^{-21}$ m^2/s [21]. It was concluded that phase separation in SiOC and/or SiCN leads to the formation of an interconnected network of amorphous SiO_2 or amorphous Si_3N_4, providing an interlinked diffusion path for both silicon and nitrogen [20].

The determined carbon mobility in the system studied here is approximately two orders of magnitude faster as compared for example to silicon. What is important to note is the initially fast diffusion of carbon with 10^{-16} m^2/s, which is considerably slowed down during the ongoing microstructure evolution. It is assumed that this variation in carbon diffusivity is a direct consequence of the formation of cristobalite

on the internal surfaces (see Figure 10). The diffusion coefficients obtained in this study are by several orders of magnitude lower as compared to for example carbon diffusion in silicon (10^{-14} m^2s^{-1} at 1300°C [22, p. 197]) and interstitial diffusion of carbon in iron ($6.2*10^{-10}$ m^2/s at 1000°C [23]). The calculated diffusion coefficients upon annealing for 10, 100 and 200 h differ not much from substitutional diffusion of carbon in GaAs ($7.8*10^{-19}$ m^2/s at 960°C [24]), being by one order of magnitude larger for 10 h, and by a factor of three smaller for 200 h, and almost identical for 100 h, respectively.

It should be noted that the carbon diffusion coefficients determined in this study are only seen as a first estimate. Nevertheless, the pronounced change in carbon content in close proximity to internal surfaces is seen as the driving force for a change in the hafnium diffusivity, which is the main focus of the present work and will be discussed in the following chapter.

5.5 Diffusion of Hafnium

In the following, the LSW theory is applied to the observed coarsening of the hafnia precipitates upon prolonged annealing times (i.e. 10, 100, and 200 h, respectively), in order to derive the volume diffusion coefficient of hafnium solved in the matrix using eq. 4 (chapter 4.2.3). The as-pyrolyzed HfO_2/SiHfOC material (i.e., the sample annealed for 1 h) shows no major variation among average HfO_2 precipitate sizes, comparing bulk regions with areas close to internal surfaces (see Figure 8 and Figure **9**). This sample was considered as the onset configuration for particle coarsening. In order to calculate the concentration of solved hafnium, we redraw on results from the chemical analysis of an as-pyrolyzed sample (1300°C), since EDS analysis is not able to detect the small Hf content in the amorphous matrix. The chemical data (17.3 wt% HfO_2 [1]) was converted to 4.6 vol% using the theoretical density for the tetragonal HfO_2 polymorph (10.01 g/cm^3 [25]) and the density for Hf-modified SiOC (2.3 g/cm^3 [1]), the latter being approximately the same as for low-cristobalite [26, p.156].[4] On average, the HfO_2 precipitate volume fraction in bulk and surface-near regions estimated to first approximation by TEM-image analysis is 2.6 vol% HfO_2 (see also Table 3). The difference (2.0 vol%) in HfO_2 volume fraction is the assumed

[4] Please note that the densities for Hf-modified SiOC and cristobalite, respectively, are considered estimates for the local density of the matrix in surface-near regions and in bulk regions, respectively.

fraction of solved HfO_2 in the SiHfOC bulk matrix used to calculate c_{Hf} amounting to 944.5 mol/m^3. With the parameters given in chapter 4.2.3, the calculated values for D_{Hf} derived from bulk regions for the different annealing times vary only slightly within one order of magnitude between 10^{-20} and 10^{-21} m^2s^{-1}, as shown in Table 3. Considering the sharp rise of the average particle size in surface-near regions, with the parameters given in chapter 4.2.3, the calculated values for D_{Hf} are three orders of magnitude higher as compared to those calculated for bulk regions being $1.8*10^{-17}$ m^2/s for 10 h, $8.0*10^{-18}$ m^2/s for 100 h, and $6.8*10^{-18}$ m^2/s for 200 h (see Table 3). The variation among these values is thought to be related to variations in the intrinsic local carbon content near the investigated internal surfaces of the individual samples (i.e., annealed for 10, 100, and 200 h), owing to the strong dependence of D_{Hf} on the carbon content.

Table 3: Calculated volume diffusion coefficient (D_{Hf}) on the basis of the LSW theory for bulk and surface of the annealed HfO_2/SiHfOC samples (1300°C) with the mean HfO_2 particle radius (r) and HfO_2 particle volume fraction (V) given here used for the calculation.

	bulk			**internal surface**		
time (h)	r (nm)	V (%)	D_{Hf} (m^2/s)	r (nm)	V (%)	D_{Hf} (m^2/s)
1	1.5±0.3	2.49		3.3±0.7	2.32	
10	2.0±0.3	2.91	$1.0*10^{-20}$	16.0±4.9	2.35	$1.8*10^{-17}$
100	2.3±0.6	2.55	$1.7*10^{-21}$	27.3±14.9	2.80	$8.0*10^{-18}$
200	2.7±0.9	2.63	$1.6*10^{-21}$	32.6±11.5	2.95	$6.8*10^{-18}$
Errors are ±1 σ.						

The possible effect of the matrix crystallization in the surface-near regions during the early stage of coarsening (1 - 5 h) on the effective diffusion coefficient of hafnium is thought to be comparably small [27]. Previously [3], we obtained a slightly smaller value for c_{Hf} calculated using a density of 2.2 g/cm^3. However, here, we recalculated c_{Hf} for internal surfaces in order to account for the presence of cristobalite constituting the major phase in the matrix near internal surfaces of the samples annealed for 10 h, 100 h, and 200 h, respectively. However, the value for D_{Hf} obtained here is in the same order of magnitude as compare with the previously reported one [3].

The value for D_{Hf} was recalculated according to [10]:

$$\frac{d(r^3)}{dt} = \frac{8Dc\gamma\Omega^2}{9RT} \quad eq.7$$

with the slope $d(r^3)/dt$ determined by fitting the experimental data for internal surface and bulk to linear functions. This procedure yields diffusion coefficients (see Figure 13) that are in good agreement with the data obtained from the calculation using eq. 4 (see Table 3).

It is interesting that the diffusivities of Hf in SiHfOC (bulk) obtained here (10^{-20} to 10^{-21} m^2s^{-1} at 1300°C) are within the experimental range of Hf cation diffusivities in silicates (zircon) [28] and oxides (rutile [29] and zirconia [30]) (see also Table 4). This is similar to what can be noted for diffusion of Si species in ionic silicates [31,32] or in covalent network structures such as amorphous silica [19], SiCN [33], SiBCN [33,34], and SiOC [18], diffusivities being on the same order of magnitude (see also Table 4). When comparing the Hf diffusivity in bulk regions ($2*10^{-21}$ m^2/s, this work) and the diffusivity of Si in Si-rich SiOC [18], the former is by a factor of 3.5 lower. Because a size dependence of cation diffusion in silicates [28] and oxides [29,30] was observed, we may not rule out a size dependence for the diffusivities among the tetravalent cations of Hf (Hf^{4+} 0.85 Å [35]) and Si (Si^{4+} 0.40 Å [35]) in an amorphous SiOC network structure that contains phase separated silicate apart from carbidic environments and varying amounts of a graphite-like carbon phase [36-38]. For instance, Cherniak et al. (1997) [28] reported diffusivities in zircon among the tetravalent cations of Hf and Th within the range of $4*10^{-22}$ m^2s^{-1} for Hf^{4+} and $8*10^{-23}$ m^2s^{-1} for the larger Th^{4+} cation, respectively. They stated, however, that beside cation size several other factors (such as ionic charge, lattice geometry, or charge compensating species) can also affect the cation diffusivity. The Hf diffusivity in surface-near regions reaches a value within the range of reported data for interstitial diffusion in covalent solids, which are the fastest diffusivities known for these materials except for hydrogen diffusion, e.g. Hf in Si [39], Au in amorphous Si_3N_4 [40], and Si in Si [41] (see also Table 4). The change in Hf diffusivity between SiOC bulk and C-depleted SiO_2-rich regions (this work) is also consistent with results reported by Ikarashi et al. (2006) [42], who performed diffusion experiments using HfO_2/a-SiO_2 and HfO_2/SiON thin films and stated that Hf diffusion in amorphous silicon oxynitride (SiON) films at 1000°C was slower than in pure silica films. Moreover, the trend of Hf diffusion in SiOC (bulk) vs. SiO_2 (internal surface) is consistent with the fact that the viscosity of SiOC is several orders of magnitude higher than that of amorphous silica, as shown by Rouxel et al. (2001) [43]. However,

an unequivocal relationship between the measured viscosity and the diffusion coefficient in amorphous solids could not be established within this study.

Table 4: Selected diffusion coefficients for various materials together with data of this work. Many studies give only the Arrhenius laws; here, D is calculated from the Arrhenius laws at the temperature indicated. For the crystalline materials given here, the lattice diffusion coefficient is given.

system	**element**	**D (m^2/s)**	**ref.**
SiOC	Hf	$2*10^{-21}$, $7*10^{-18}$ (1300°C)	this work
zircon	Hf	$8*10^{-23}$ (1400°C)	[28]
rutile	Hf	$3*10^{-21}$ (1000°C)	[29]
t-YTZ-3	Hf	$8*10^{-20}$ (1400°C)	[30]
olivine (along [001])	Si	$2*10^{-22}$ (1300°C)	[31]
quartz (parallel to c)	Si	$3*10^{-21}$ (1350°C)	[32]
quartz (parallel to c)	Ti	$7*10^{-18}$ (1150°C)	[44]
a-SiO_2	Si	$2*10^{-21}$ (1300°C)	[19]
a-SiCN	Si	$5*10^{-21}$ (1300°C)	[20]
a-SiBCN	Si	$6*10^{-22}$ (1300°C)	[33]
a-SiOC	Si	$7*10^{-21}$ (1300°C)	[18]
Si	Hf	$4*10^{-17}$ (1250°C)	[39]
a-Si_3N_4 (and in SiCN)	Au	$3*10^{-18}$ (1020°C)	[40]
Si	Si	$3*10^{-17}$ (1300°C)	[41]
Si	C	$1*10^{-14}$ (1300°C)	[22]
a-Si_3N_4	N	$3*10^{-21}$ (1300°C)	[21]

5.6 References

[1] E. Ionescu, B. Papendorf, H.-J. Kleebe, F. Poli, K. Müller, and R. Riedel (2010). Polymer-derived silicon oxycarbide/hafnia ceramic nanocomposites. Part I: Phase and microstructure evolution during the ceramization process. *J. Am. Ceram. Soc.*, 93(6), 1774-1782.

[2] S. V. Ushakov, A. Navrotsky, Y. Yang, S. Stemmer, K. Kukli, M. Ritala, M. A. Leskelä, P. Fejes, A. Demkov, C. Wang, B.-Y. Nguyen, D. Triyoso, and P. Tobin (2004). Crystallization in hafnia- and zirconia-based systems. *Phys. Stat. Sol. B*, 241(10), 2268-2278.

[3] H.-J. Kleebe, K. Nonnenmacher, E. Ionescu, and R. Riedel (2012). Decomposition-coarsening model of SiOC/HfO_2 ceramic nanocomposites upon isothermal anneal at 1300 °C. *J. Am. Ceram. Soc.*, 95(7), 2290-2297.

[4] H.-J. Kleebe (1998). Microstructure and stability of polymer-derived ceramics: the Si-C-N system. *Phys. Stat. Sol. A*, 166(1), 297-312.

[5] H.-J. Kleebe, D. Suttor, H. Müller, and G. Ziegler (1998). Decomposition-crystallization of polymer-derived Si-C-N ceramics. *J. Am. Ceram. Soc.*, 81(11), 2971-2977.

[6] M. Weinmann, E. Ionescu, R. Riedel, and F. Aldinger (2013). Precursor-derived ceramics. In S. Somiya, F. Aldinger, N. Clausen, R. M. Spriggs, K. Uchino, K. Koumoto, and M. Kaneno (Eds.), *Handbook of Advanced Ceramics* (2nd ed.) (pp. 1025-1101). Amsterdam, The Netherlands: Elsevier.

[7] B. Papendorf (2012). *Keramische Nanokomposite auf Basis von SiOC/HfO_2 und SiCN/HfO_2: Herstellung und Untersuchungen zum Hochtemperaturverhalten.* (Unpublished doctoral dissertation.) Technische Universität Darmstadt, Darmstadt, Germany.

[8] R. L. Withers, J. G. Thompson, and T. R. Welberry (1989). The structure and microstructure of α-cristobalite and its relationship to β-cristobalite. *Phys. Chem. Min.*, 16(6), 517-523.

[9] M. Lifshitz and V. V. Slyozov (1961). The kinetics of precipitation from supersaturated solid solutions. *J. Phys. Chem. Solids*, 19(1-2), 35-50.

[10] C. Wagner (1961). Theorie der Alterung von Niederschlägen durch Umlösen (Ostwald-Reifung). *Z. Elektrochem.*, 65(7-8), 581-591.

[11] S. Weinbruch, V. Styrsa, and T. Dirsch (2006). The size distribution of exsolution lamellae in iron-free clinopyroxene. *Am. Mineral.*, 91, 551-559.

[12] A. J. Ardell (1972). The effect of volume fraction on particle coarsening: theoretical considerations. *Acta Metall. Mater.*, 20(1), 61-71.

[13] H.-J. Kleebe, G. Gregori, M. Weinmann, and P. Kroll (2009). Microstructure evolution and characterization. In P. Colombo, R. Riedel, G.-D. Sorarù, and H.-J. Kleebe (Eds.), *Polymer derived ceramics: from nanostructure to applications* (pp. 127-209). Lancaster, PA: DEStech Publications.

[14] R. Dohmen and R. Milke (2010). Diffusion in polycrystalline materials: Grain boundaries, mathematical models, and experimental data. In Y. Zhang and D. J. Cherniak (Eds.), *Diffusion in Minerals and Melts*, (pp. 921-970). Chantilly, VA: The Mineralogical Society of America.

[15] F. Aumento (1966). Stability, lattice parameters, and thermal expansion of beta-cristobalite (high-cristobalite). *Am. Mineral.*, 51, 1167-1176.

[16] K. Terauds, D. B. Marshall, and R. Raj (2013). Oxidation of polymer-derived HfSiCNO up to 1600°C. *J. Am. Ceram. Soc.*, 96(4), 1278-1284.

[17] E. B. Watson and R. Dohmen (2010). Non-traditional and emerging methods for characterizing diffusion in minerals and mineral aggregates. In Y. Zhang and D. J. Cherniak (Eds.), *Diffusion in Minerals and Melts*, (pp. 61-105). Chantilly, VA: The Mineralogical Society of America.

[18] G. Gregori, H.-J. Kleebe, D. W. Readey, and G. D. Sorarù (2006). Energy-filtered TEM study of Ostwald ripening of Si nanocrystals in a SiOC glass. *J. Am. Ceram. Soc.*, 89(5), 1699-1703.

[19] G. Brebec, S. Seguin, G. Sella, J. Bevenot, and J.C. Martin (1980). Diffusion du silicium dans la silice amorphe. Acta Metall. Mater., 28(3), 327-333.

[20] E. Hüger, H. Schmidt, J. Stahn, B. Braunschweig, U. Geckle, M. Bruns, and A. Markwitz (2009). Atomic transport in metastable compounds: case study of self-diffusion in Si-C-N films using neutron reflectometry. *Phys. Rev. B*, 80, 220101(R).

[21] H. Schmidt, M. Gupta, and M. Bruns (2006). Nitrogen diffusion in amorphous silicon nitride isotope multilayers probed by neutron reflectometry. *Phys. Rev. Lett.*, 96(5), 055901.

[22] T. Y. Tan and U. Gösele (2005). Diffusion in semiconductors. In P. Heitjans and J. Kärger (Eds.), *Diffusion in Condensed Matter* (pp. 165-208). Berlin, Germany: Springer.

[23] J. Kucera and K. Stransky (1982). Diffusion in iron, iron solid solutions and steels. *Mater. Sci. Eng.*, 52(1), 1–38.

[24] H. M. You, T. Y. Tan, U. M. Gösele, S. T. Lee, G. E. Höfler, K. C. Hsieh, and N. Holonyak (1993). Al-Ga interdiffusion, carbon acceptor diffusion, and hole reduction in carbon-doped $Al_{0.4}Ga_{0.6}As$/GaAs superlattices: the As_4 pressure effect. *J. Appl. Phys.*, 74(4), 2450-2460.

[25] C. E. Curtis, L. M. Doney, and J. R. Johnson (1954). Some properties of hafnium oxide, hafnium silicate, calcium hafnate and hafnium carbide. *J. Am. Ceram. Soc.*, 37(10), 458-465.

[26] M. Okrusch and S. Matthes (2009). *Mineralogie* (8th ed.). Berlin, Germany: Springer.

[27] K. Marquardt, E. Petrishcheva, R. Abart, E. Gardés, R. Wirth, R. Dohmen, H.-W. Becker, and W. Heinrich (2010). Volume diffusion of Ytterbium in YAG: thin-film experiments and combined TEM-RBS analysis. *Phys. Chem. Miner.*, 37(10), 751-760.

[28] D. J. Cherniak, J. M. Hanchar, and E. B. Watson (1997). Diffusion of tetravalent cations in zircon. *Contrib. Mineral. Petrol.*, 127, 383-390.

[29] D. J. Cherniak, J. Manchester, and E. B. Watson (2007). Zr and Hf diffusion in rutile. *Earth Planet. S. Lett.*, 261(1-2), 267-279.

[30] S. Swaroop, M. Kilo, C. Argirusis, G. Borchardt, and A. H. Chokshi (2005). Lattice and grain boundary diffusion of cations in 3YTZ analyzed using SIMS. *Acta Mater.*, 53(19), 4975–4985.

[31] R. Dohmen, S. Chakraborty, and H. W. Becker (2002). Si and O diffusion in olivine and implications for characterizing plastic flow in the mantle. *Geophys. Res. Lett.*, 29(21), 26-1–26-4.

[32] O. Jaoul, F. Béjina, F. Élie, and F. Abel (1995). Silicon self-diffusion in quartz. *Phys. Rev. Lett.*, 74(11), 2038-2041.

[33] H. Schmidt, G. Borchardt, S. Weber, H. Scherrer, H. Baumann, A. Müller, and J. Bill (2002). Comparison of ^{30}Si diffusion in amorphous SiCN and SiBCN precursor-derived ceramics. *J. Non-Cryst. Sol.*, 298(2-3), 232-240.

[34] H. Schmidt, G. Borchardt, O. Kaitasov, and B. Lesage (2007). Atomic diffusion of boron and other constituents in amorphous SiBCN. *J. Non-Cryst. Sol.*, 353(52-54), 4801-4805.

[35] D. R. Lide (2008). Atomic Radii of the Elements. In D. R. Lide (Ed.), *CRC Handbook of Chemistry and Physics* (89th ed.) (pp. 9-49). Boca Raton, FL: CRC Press.

[36] H.-J. Kleebe, C. Turquat, and G. D. Sorarù (2001). Phase separation in a SiOC glass studied by transmission electron microscopy and electron energy-loss spectroscopy. *J. Am. Ceram. Soc.*, 84(5), 1073–1080.

[37] C. Turquat, H.-J. Kleebe, G. Gregori, S. Walter, and G. D. Sorarù (2001). Transmission electron microscopy and electron energy-loss spectroscopy study of nonstoichiometric silicon-carbon-oxygen glasses. *J. Am. Ceram. Soc.*, 84(10), 2189–2196.

[38] G. Gregori, H.-J. Kleebe, Y. D. Blum, and F. Babonneau (2006). Evolution of C-rich SiOC ceramics: Part II. Characterization by high lateral resolution technique: electron energy loss spectroscopy. High-resolution TEM and energy-filtered TEM. *Int. J. Mater. Res.*, 97(6), 710-720.

[39] R. Sachdeva, A.A. Istratov, P.N.K. Deenapanray, and E.R. Weber (2006). Electrical properties and diffusion behavior of hafnium in single crystal silicon. *Appl. Phys. A*, 84(4), 351-367.

[40] S. Matics and W. Frank (2001). Diffusion of gold in amorphous ceramic $Si_{28}C_{36}N_{36}$", *Defect. Diffus. Forum*, 194-199, 947-952.

[41] J. M. Fairfield and B. J. Masters (1967). Self-diffusion in intrinsic and extrinsic silicon. *J. Appl. Phys.*, 38 (8), 3148-3154.

[42] N. Ikarashi, K. Watanabe, K. Masuzaki, T. Nakagawa, and M. Miyamura (2006). The influence of incorporated nitrogen on the thermal stability of amorphous HfO_2 and Hf silicate. *J. Appl. Phys.*, 100, 063507-1-5.

[43] T. Rouxel, G. D. Sorarù, and J. Vicens (2001). Creep viscosity and stress relaxation of gel-derived oxycarbide glasses. *J. Am. Ceram. Soc.*, 84(5), 1052–1058.

[44] D. J. Cherniak, E. B. Watson, and D. A. Wark (2007). Ti diffusion in quartz. *Chem. Geol.*, 236, 65-74.

6 HfO_2/SiHfCNO Nanocomposites

6.1 Motivation

The backscattered scanning electron images of fracture surfaces shown in Figure 15 reveal the microstructure of an as-pyrolyzed SiHfCNO sample pyrolyzed at 1100°C (3 h) prepared from hafnium-alkoxide modified polysilazane. As can be seen in Figure 15 (a), the bulk appears rather featureless [1], while in (b), in close proximity to microsized cracks within the interior of the sample, an inhomogeneous distribution of hafnia is shown. In particular, a variation of the size of the hafnia precipitates is observed in this image. Local microcracking in polymer-derived ceramic monoliths is typically a consequence of the built-up of high gas pressures within the interior of the monoliths, owing to the pronounced formation of volatile decomposition products during the pyrolytic conversion [2].

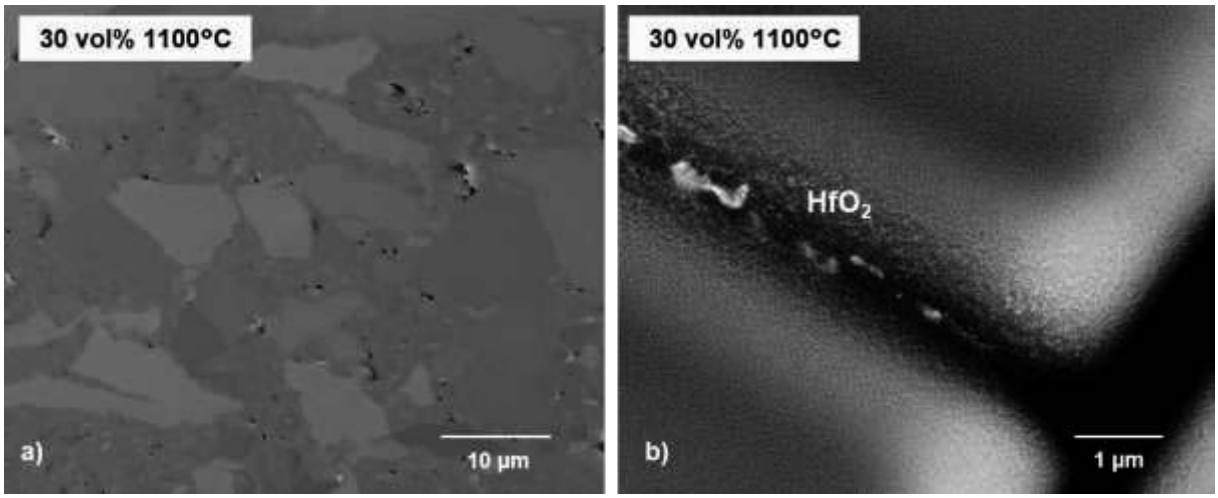

Figure 15: Backscattered electron images (SEM) of a fracture surface of an as-pyrolyzed monolithic SiHfCNO sample (1100°C). The overview in (a) reveals a rather dense bulk apart from a minor amount of closed porosity, while in (b) a microcrack within the interior of the sample is shown. In close proximity to the crack, the variation of the size of HfO_2 precipitates can also be seen. Images courtesy of H.-J. Kleebe.

The corresponding HRTEM results [1] for this material show an overall amorphous bulk matrix with no indication for the presence of HfO_2 precipitates, which was considered characteristic for the SiHfCNO material. These observations are consistent with the SEM results shown in Figure 15 (a) [1], but are not in accordance with the observation of a local variation of HfO_2 precipitate size within the interior of the same sample (Figure 15 (b)).

Such differences in the intrinsic microstructure depicted in Figure 15 between surface-near regions and bulk regions have also been reported for other polymer-derived ceramics. Recently, it was reported that polymer-derived HfSiCNO ceramic particles heat treated at 1500°C in ambient air showed an initial enhanced oxidation, which was related to a difference in the composition of regions near the surface prone to oxidation compared with the particle bulk, though not investigated in detail [3]. In the same reference [3], an unexpected marked growth of hafnia precipitates in the silica-rich overgrowth layer, as compared to the bulk of the sample, was observed.

In [4, p. 9745], a backscattered scanning electron image of ceramic SiHfCNO particles (heat treated at 1500°C in vacuum) is given which reveals an inhomogeneous distribution of hafnia particles near the particle boundaries, as deduced form the Z contrast, though not further discussed by the authors.

As shown in chapter 5.2 (this work), SiHfOC monoliths (approximately 14 wt% Hf content and deliberately annealed for various times under isothermal conditions at 1300°C for 1, 10, 100, and 200 h) revealed a local inhomogeneous hafnia (HfO_2) precipitate size near internal surfaces, which was shown to be related to an enhanced hafnium diffusion relative to bulk regions (chapter 5.5). One of the major results is that the diffusion coefficient of hafnium calculated based on the LSW theory [5,6] for Ostwald ripening varied by three orders of magnitude comparing surface and bulk [7].

In order to gain further information on the origin of such differences in the intrinsic microstructure of the SiHfCNO material between surface-near regions and bulk regions, an annealing experiment was performed at 1300°C in argon with annealing times of 1, 3, 10, 50, 100, and 200 h. TEM in conjunction with energy-dispersive X-ray spectroscopy (EDS) was used for local microstructure and compositional analysis. In order to make the two annealing experiments conducted on SiHfOC samples (chapter 5) and SiHfCNO samples (this chapter) comparable, the same conditions for EDS quantification were chosen as for the SiHfOC samples (see chapter 4.2.2). Based on the preliminary SEM investigation (see Figure 15) mentioned above, the aim was to verify as to what extent the local microstructure of the bulk of the annealed samples differs from that near microcracks (internal surfaces). In the following, the results of these annealing experiments will be presented.

6.2 Microstructure Characterization

The micro/nanostructure of an area within the bulk of the SiHfCNO sample annealed for 1 h at 1300°C is shown in Figure 16. A homogeneous amorphous matrix with quinary composition (SiHfCNO), as detected by EDS analysis, was observed. The overall amorphous nature of the bulk regions investigated is also indicated by the diffuse halo in the selected area electron diffraction pattern shown in the inset in Figure 16 (a). Neither the presence of hafnia precipitates nor silicon nitride, as both indicated by ^{29}Si-NMR [2], can be discerned in the high-resolution TEM image shown. At least, some evidence for the segregation of graphite-like turbostratic carbon is seen in Figure 16 (b), in accordance with ^{13}C-NMR [2] and Raman experiments [8, p. 61].

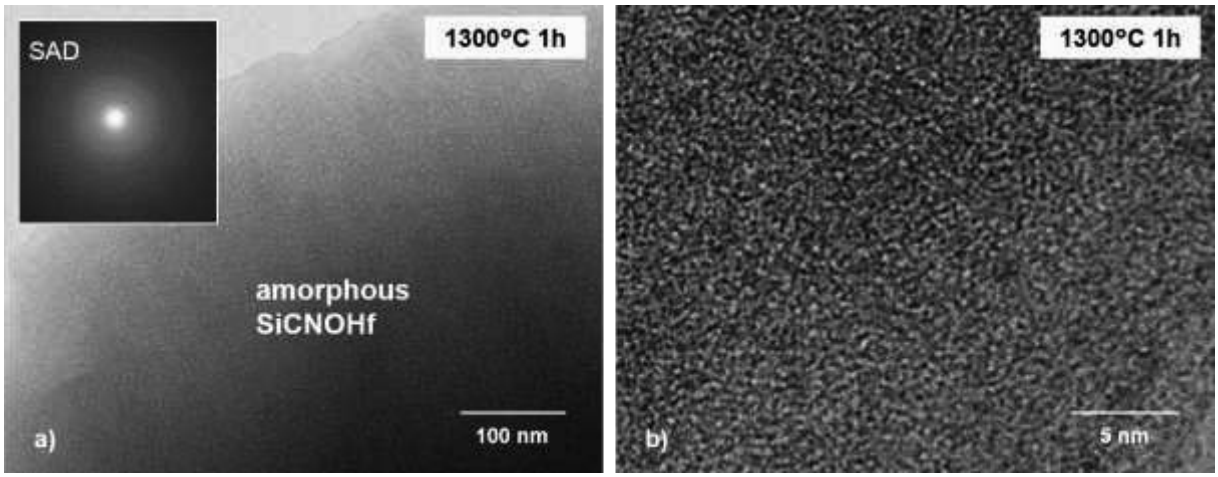

Figure 16: (a) TEM bright-field and (b) high-resolution TEM image of the bulk SiHfCNO sample annealed at 1300°C in argon for 1 h. In (b), no evidence for the phase separation-crystallization of hafnia and silicon nitride, as indicated by ^{29}Si NMR [2], is seen.

Ikarashi et al. (2006) [9] investigated the chemical distribution in amorphous hafnium silicate films upon nitrogen incorporation followed by annealing, as nitrogen was expected to have an influence on the phase separation and crystallization of hafnia. The authors proposed that Si-N bonding suppresses the precipitation of hafnia, but could not rule out a possible effect for Hf-N bonds on the phase separation of the hafnium silicate glass. In the same reference [9], a diffusion coefficient for Hf at 1000°C in an amorphous HfO_2/oxynitride (5 at% nitrogen) stacked layer was reported ($1*10^{-22}$ m^2/s) which was by a factor of 2.5 smaller as compared with the diffusivity of Hf in an amorphous HfO_2/SiO_2 layer structure ($2.5*10^{-22}$ m^2/s). The authors concluded, that the observed effect of nitrogen incorporation on phase separation within the amorphous hafnium-silicate film is related to the slower hafnium diffusion in

the nitrogen-modified silicate network structure as compared with the parent (i.e. nitrogen-free) silicate structure. It is important to note here that, apart from the rather featureless amorphous bulk, the same sample reveals a pronounced change in microstructure, however, only in the proximity to internal surfaces. Figure 17 depicts the rather abrupt local segregation of hafnia (HfO_2) in vicinity to an internal surface that is associated with a microcrack, which is consistent with (i) previous TEM observations obtained on a material pyrolyzed at 900°C, revealing a percolation network of an amorphous Hf-containing phase [2], and (ii) the XRD data obtained on a similar material pyrolyzed at 1300°C [8, p. 42].

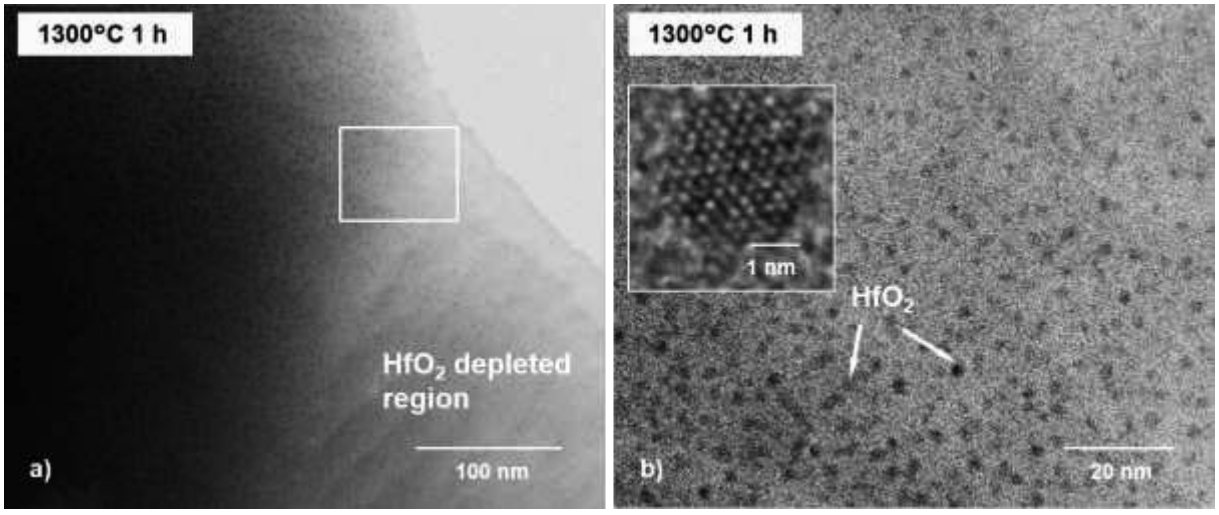

Figure 17: (a) Bright-field TEM image and (b) high-resolution TEM image (inset) of surface-near areas showing HfO_2 particles in a SiHfCNO sample annealed at 1300°C for 1 h. The HRTEM images in (b) are obtained on the boxed region shown in (a). In contrast to the amorphous bulk, here, the sample reveals the presence of crystalline and spherical HfO_2 nanoparticles.

In a recent study [10], using an amorphous as-pyrolyzed SiHfCNO material (1000°C) derived from a hafnium tert-butoxide-modified polysilazane, it was found that hafnium is totally solved in the matrix without precipitation as hafnia up to a Hf/Si ratio of about 0.2, according to XRD results. For compositions with a Hf/Si ratio larger than this threshold value, precipitation of HfO_2 at 1000°C was observed [10]. This finding is consistent with our results, at least with respect to the bulk microstructure of all samples investigated, as here the mean Hf/Si ratio within the overall amorphous matrix is well below 0.2 (approximately 0.06). However, in the samples investigated here, the precipitation of HfO_2 monitored typically in surface-near regions could not be related to any marked local change in the Hf/Si ratio using quantitative EDS, still being well below the threshold value for precipitation reported in [10].

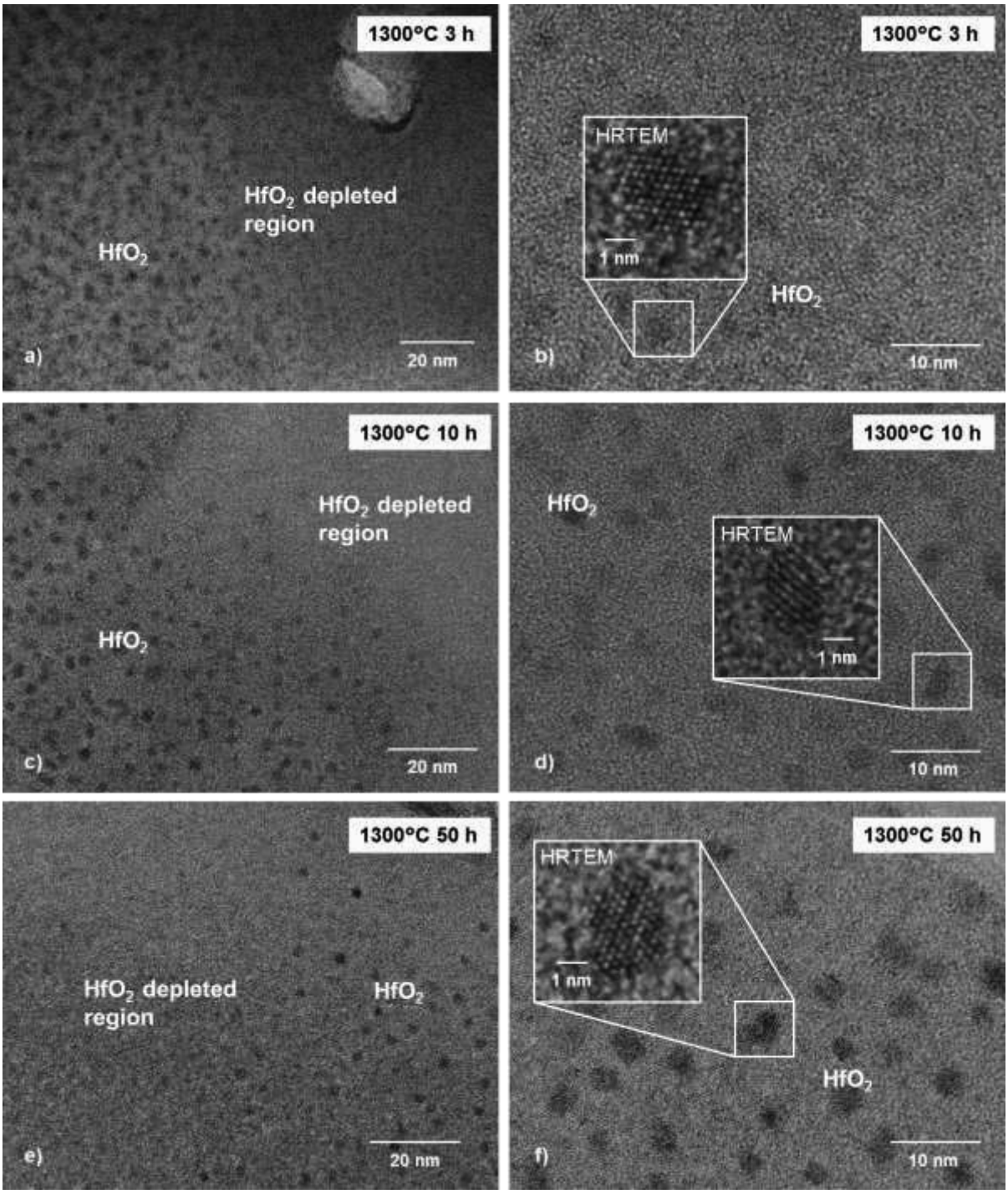

Figure 18: High-resolution TEM images (left: lower magnification, right: higher magnification) of HfO_2 particles within the SiHfCNO matrix in vicinity to internal surfaces of the samples annealed for various times indicated in the upper right corner of each image. The HRTEM images in (b), (d), and (f) only show a rather sluggish growth of the HfO_2 particles with time.

At longer isothermal annealing (i.e., from 3 to 200 h), the amorphous nature of the bulk of the samples is preserved, as revealed by HRTEM (see Figure 32 in the Appendix), except for the sample annealed for 100 h. The latter sample is, thus, excluded from further discussion and will be addressed separately in chapter 6.6. Similar to the sample annealed for 1 h, the samples annealed for 3, 10, and 50 h

reveal spherical nanosized HfO_2 precipitates that are already crystalline within an amorphous matrix, as can be seen in Figure 18. Representative particle size distributions (PSDs) of those as-precipitated HfO_2 nanoparticles for 1, 10, 50 and 200 h annealing time are shown in Figure 19. They were obtained from numerous TEM images of small HfO_2 crystallites. It is important to note that in these regions, the particle size of HfO_2 did only increase by a factor of 2.5, when comparing the samples annealed for 1 and 200 h (Figure 19). It is therefore concluded that the diffusion of hafnium in the amorphous matrix is rather sluggish, which will also be addressed below (chapter 6.4). At the early stage of annealing (i.e., from 1 to 10 h), rather narrow size distributions were obtained, although a small size interval of only 1 nm was used. A slight broadening of the distributions was observed with longer time (200 h). Broader and more symmetric size distributions than predicted by the classical LSW theory are often reported for real coarsening systems [11, p. 115] and are consistent with theoretical predictions of Ardell (1972) [12], who considered the effect of non-zero particle volume fractions on the size distribution in the case of diffusion-controlled coarsening. In our case, the mean volume fraction of small HfO_2 particles is approximately 0.3 % (see also Table 5). It is therefore assumed that, in our case, the non-zero particle volume fraction affects the width of the size distribution [12].

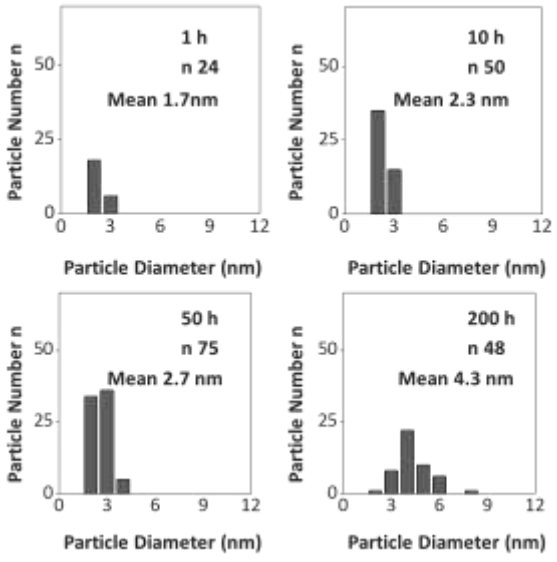

Figure 19: Particle size distributions of nanosized HfO_2 particles observed in vicinity to internal surfaces. Annealing times are indicated in the upper right corner of each graph. The data correspond to the TEM images depicted in Figure 17 (1 h), Figure 18 (10 and 50 h), and Figure 21 (f) (200 h), respectively. In addition, the total number, n, of the particles being measured and the mean diameter are indicated in each graph.

The mean diameter of the HfO_2 precipitates increases toward internal surfaces of the sample annealed for 1 h (see Figure 20), owing to the growth of the precipitates at a locally varying rate. The maximum particle size was observed in the outermost region of internal surfaces, the mean particle diameter being 5 nm after 1 h annealing (Figure 20 (b)). With increasing annealing time (i.e., from 3 to 200 h), the average particle size increases, as can be seen in the TEM bright-field images shown in Figure 21 (a-e) and is reflected in the corresponding PSDs shown in Figure 22, maximum means of the particle diameter being 3, 7, 18, and 22 nm for 3 (see Figure 33 in the Appendix), 10, 50, and 200 h, respectively, within the outermost area of the investigated internal surfaces. Less pronounced growth of HfO_2 was monitored for the sample annealed for 3 h (Figure 21 (b)), as compared to the sample annealed for only 1 h (Figure 21 (a)). A steep increase of the average HfO_2 particle diameter across the surface-near area by a factor of 5 upon annealing for 200 h was observed (Figure 21 (e,f), see also the corresponding PSDs in Figure 19 and Figure 22). These pronounced variations in the local growth rate of the HfO_2 precipitates between bulk and surface-near regions are thought to be related to intrinsic differences in the hafnium diffusivity within the matrix, which depends on the local composition of the respective host matrix (see chapter 6.3 for further details).

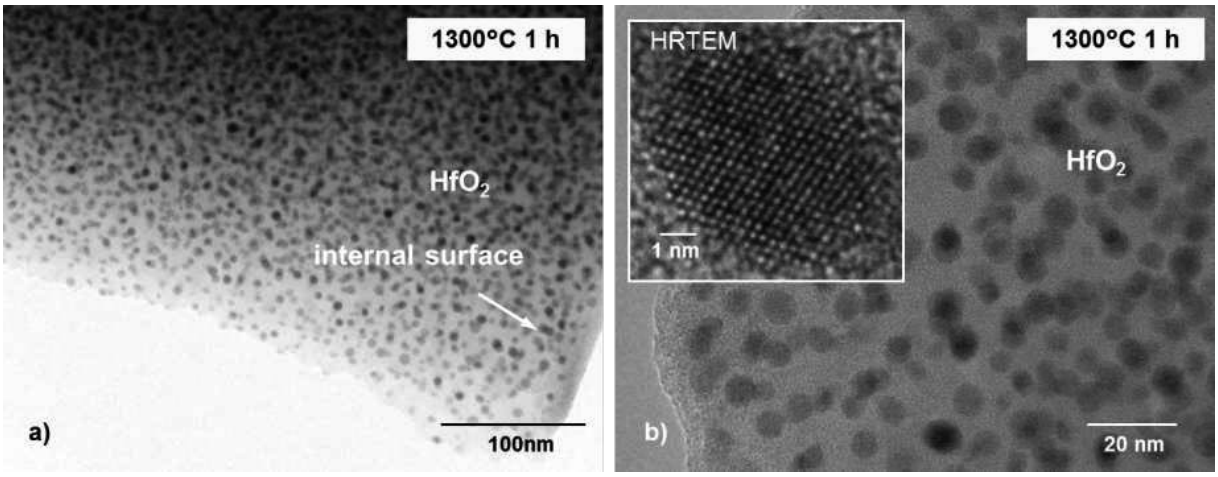

Figure 20: (a-b) TEM bright-field images of a surface-near region (internal surface associated with a microcrack, indicated arrow) after 1 h annealing. The area near a microcrack contains well-crystallized hafnia precipitates. Such surface-near regions are transparent in the light microscope due to the pronounced depletion in overall carbon content. The inset in (b) reveals a high-resolution TEM image of one nearly spherical hafnia precipitate within an amorphous SiHfO(C,N) matrix.

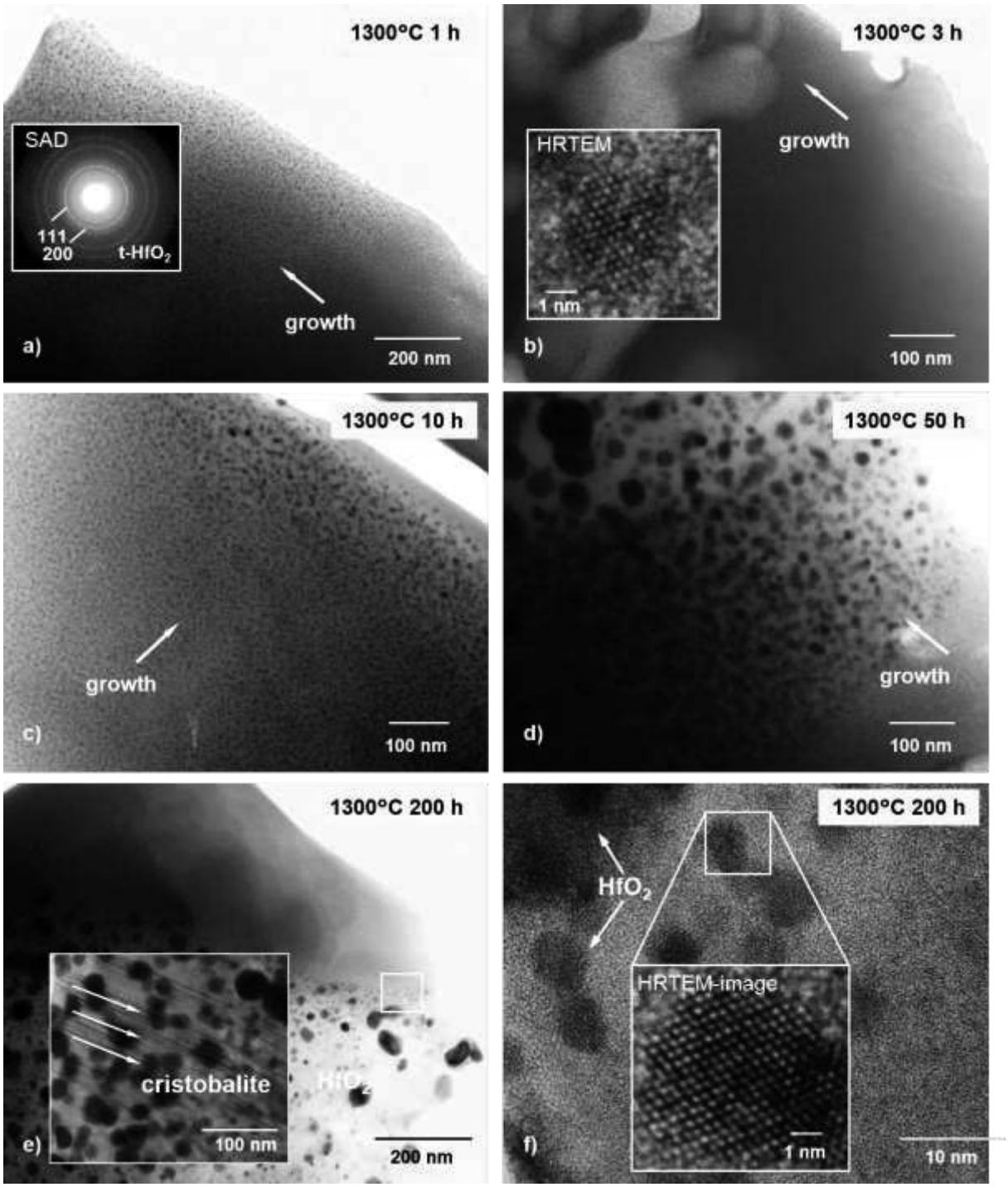

Figure 21: (a – e) TEM bright-field images of the microstructure evolution with increasing annealing time (indicated in the upper right corner of each image) in outermost areas of surface-near regions. Pronounced local growth of HfO_2 precipitates in surface-near regions was observed, except for the sample annealed for 3 h, where the growth is less pronounced, as depicted in the HRTEM image (inset) in (b). In (e), apart from the amorphous bulk (upper half of the image in (e)), a crystallized surface-near area (lower half) is shown. Faint striations in the inset in (e) (indicated by arrows) mark defects in cristobalite [13]. In (f), a HRTEM image of the boxed area in (e) is shown that reveals a relatively narrow zone between the featureless bulk matrix and the outermost cristobalite growth zone which is constituted of HfO_2 (see the HRTEM image in the inset in (f)) dispersed in an amorphous matrix.

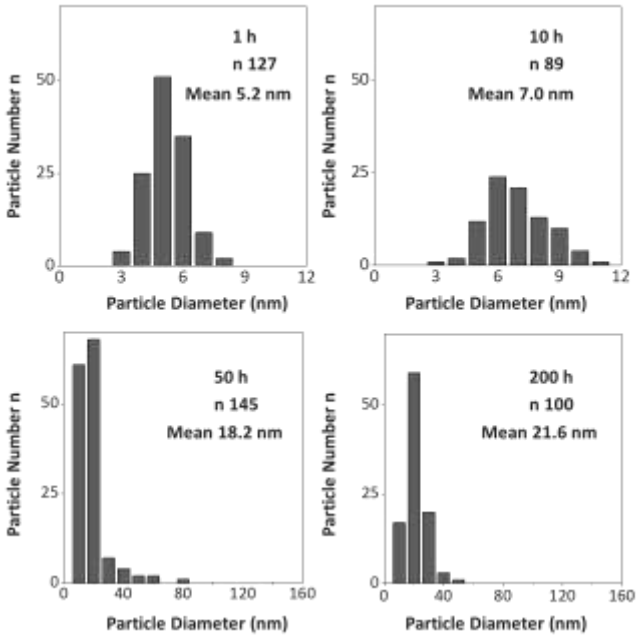

Figure 22: Particle-size distributions of HfO_2 in the outermost SiO_2-rich regions of internal surfaces of the samples annealed for 1, 10, 50, and 200 h. N is the total number of particles measured. The host matrices within the outermost regions are predominantly constituted of amorphous SiO_2, except for the case of the sample annealed for 200 h, showing the local formation of cristobalite within the investigated area. Please note that a larger size interval of 10 nm was used for 50 and 200 h, as compared to the size interval (1 nm) for 1 and 10 h.

In Figure 22, a pronounced broadening of the size distribution upon longer heat treatment exceeding 10 h can be observed. In addition to the significant role of the particle volume fraction for diffusion-controlled coarsening considering the width of the size distribution (see p. 74), according to Ardell (1972) [12], the surface-near nucleation of cristobalite should be taken into account. Defects in cristobalite (i.e., grain boundaries) were typically observed in the sample annealed for 200 h via TEM (see the defect structure depicted in the inset in Figure 21 (f)), which may provide a fast diffusion path. Grain boundary diffusion coefficients of oxygen and diverse cations in various silicates and calcite are typically by a factor of between 10^4 and 10^7 larger than the respective lattice diffusion coefficients [14, p. 964]); hence coarsening of HfO_2 in cristobalite is assumed to be dominated by grain boundary diffusion, which may explain the broad size distributions observed for the prolonged annealing times.

Please note that the SiHfCNO annealed for 1 h reveals approximately the same mean diameter of the HfO_2 precipitates near an internal surface (5 nm, Figure 20) as the corresponding SiHfOC sample (7 nm, Figure 9, chapter 5.2). This finding is most likely due to similar intrinsic chemical compositions of the host matrices within the

investigated areas of both samples, as is confirmed by quantitative EDS analyses (compare Tables 1, chapter 5.3, and 5, chapter 6.3, respectively).

6.3 Origin of the Pronounced HfO_2 Particle Size Variation

In the case of HfO_2/SiHfOC, quantitative EDS analysis shows that the presence of coarsened precipitates is typically related to a silica-rich host matrix. Therefore, the relative local overall composition (in mole fractions) was also analysed for the SiHfCNO samples, in particular, for internal surfaces and bulk regions.

Calculated element fractions (in at%) obtained therefrom are given in Table 5. As can be seen in Table 5, the EDS analysis showed no major relative variation in composition for bulk regions. However, near internal surfaces of the annealed SiHfCNO samples, the local content of carbon (with mean 30 at% in the bulk, see also Table 6) and nitrogen (mean 28 at% in the bulk), respectively, plummet to values below 2 at% (nitrogen) and 5 at% (carbon), which was also noticeable by a local color change from dark brown toward transparent using visible light microscopy. Please note that the EDS quantification routine sums element fractions to hundred % for a single measurement, which results in a complementary increase of the local content for oxygen, silicon and hafnium, respectively. A somewhat higher overall amount of both carbon and nitrogen near an internal surface is monitored after 3 h annealing as compared with those of the samples annealed for 1, 10, 50, and 200 h, respectively (see Figure 33 in the Appendix). We note a local nitrogen content of typically 14 at% (mean) in areas that contain only small HfO_2 crystallites (depicted in Figure 17 for 1 h, Figure 18 for 3 - 50 h, and Figure 21 (f) for 200 h, respectively). In Table 5, such areas are denoted precipitation. Annealing for 200 h, the overall nitrogen content in the areas that contain small HfO_2 (precipitation) appears the same as in areas containing larger ones (surface) (Table 5). The precipitation-coarsening region monitored for this sample (200 h) is rather narrow (approximately 800 nm in depth, see also Figure 21 (e-f)), so that the electron beam which was 300 nm in diameter may not resolve the local variation in both carbon and nitrogen content in this area; however, due to the pronounced precipitate size variation monitored for this region, such a variation is expected.

Table 5: Quantification results (normalized to 100 %) from EDS-TEM for the SiHfCNO samples annealed for various times (at 1300°C). The same operating conditions as for the EDS analyses of the annealed SiHfOC samples (Table 1) were employed.

time (h)	location	at% C	at% N	at% O	at% Si	at% Hf
1	bulk (41) [1]	31.0±3.3	29.8±2.4	16.3±2.2	21.1±1.0	1.8±0.2
	precipitation[2]	14.9	13.3	44.3	25.5	2.2
	surface[2]	5.3	1.4	62.4	28.3	2.7
3	bulk[1] (21)	28.7±2.5	29.0±1.9	18.3±3.3	22.7±1.2	1.3±0.1
	precipitation[2]	15.3	16.8	43.1	23.4	1.5
	surface[2]	11.3	10.9	47.7	28.5	1.6
10	bulk[1] (19)	27.7±3.2	25.6±2.9	21.3±4.4	23.9±1.7	1.5±0.2
	precipitation[2]	14.6	16.1	41.8	25.9	1.7
	surface[2]	2.1	0.6	67.3	28.6	1.5
50	bulk[1] (33)	29.5±3.2	28.0±3.2	15.1±1.9	25.8±2.0	1.6±0.2
	precipitation[2]	8.4	12.8	51.2	26.2	1.4
	surface[2]	1.6	1.3	69.3	26.1	1.8
200	bulk[1] (35)	32.9±2.6	28.4±3.1	14.3±1.3	23.1±0.8	1.4±0.1
	precipitation[2]	8.6	1.9	62.2	25.9	1.4
	surface[2]	6.6	0.9	65.9	25.5	1.0

[1] The values are means calculated from multiple point analyses (± 1 σ) with the number of single measurements indicated in parentheses. Precipitation refers to HfO_2.

[2] Single point measurements.

Table 6 gives the mean overall local bulk composition obtained from the EDS data shown in Table 5 (bulk) and the overall composition of an as-pyrolyzed SiHfCNO sample (1300°C) obtained by chemical analysis. In particular, the overall local amount of carbon obtained from EDS (30 at% carbon) is systematically higher than the corresponding apparent amount obtained from chemical analysis (17 at% carbon). The discrepancy between the results of EDS measurements and chemical analysis is not solely due to an expected systematic error in the EDS quantification routine which employs theoretical k-factors and an assumed constant sample thickness (100 nm) for absorption correction, but is to a major extent due to the local vs. integral measurement. A similar trend in the quantification results was observed for the SiHfOC samples (chapter 5.3).

Table 6: Comparison of the mean local bulk content of the SiHfCNO samples from EDS analysis and quantification results from chemical analysis both summed to hundred.

method	at% C	at% N	at% O	at% Si	at% Hf
EDS-TEM (local)[1]	29.5±2.5	28.2±1.6	17.3±3.0	23.5±1.7	1.5±0.2
chemical analysis (integral)[2]	17.3	34.3	14.8	31.4	2.2

[1] The mean is calculated from the data of Table 5 (5 samples); errors are ±1 σ.
[2] The data, which is taken from [2], is for an as-pyrolyzed SiHfCNO sample (1100°C) derived from the same precursor material.

Figure 23 depicts the pronounced drop in both the local carbon and nitrogen content between bulk regions and internal surfaces for all annealed SiHfCNO samples, except for 3 h annealing (see Figure 33 in the Appendix). Near internal surfaces, both the local carbon and nitrogen content decrease steeply over a range of only a few hundred nanometers and level out in proximity to the internal surfaces.

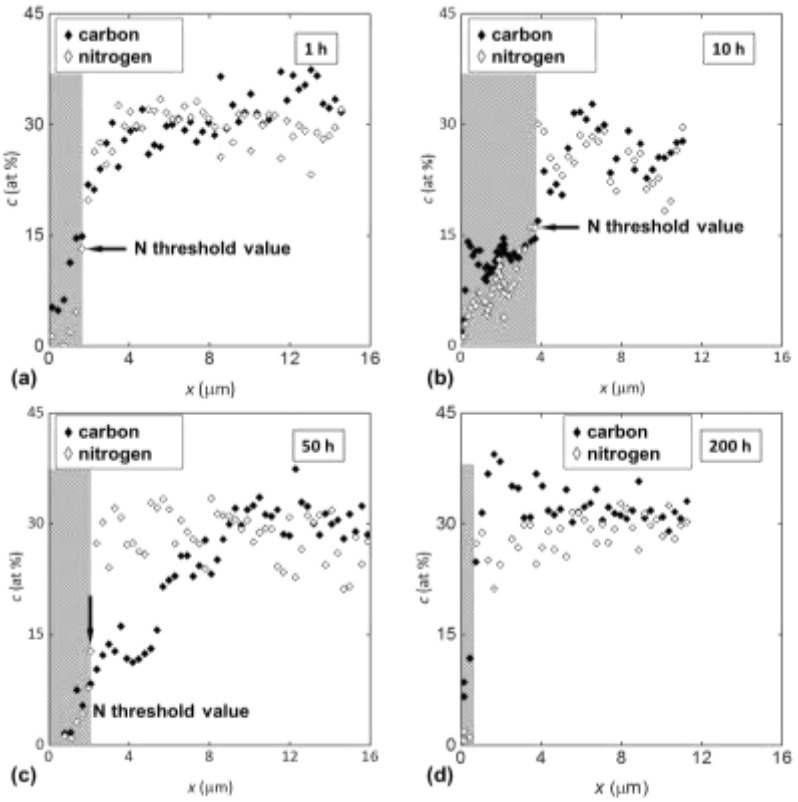

Figure 23: EDS quantification results for carbon and nitrogen as a function of distance from internal surface (at zero) of the samples annealed for 1, 10, 50, and 200 h, respectively. The shaded region in each graph between surface and the point where nitrogen is at a characteristic threshold value (appr. 14 at %) is associated with the presence of hafnia precipitates. In particular, when the local carbon content drops below a characteristic threshold value (approx. 5 at %), pronounced coarsening of the hafnia precipitates is observed.

Please note that the rather abrupt onset of the precipitation of HfO_2 monitored for all SiHfCNO samples is always related to nitrogen- and carbon-depleted matrices. In addition, the mean size of the HfO_2 precipitates increases gradually towards the surface as the local content of both nitrogen and carbon continue to decrease. In the EDS measurements (Table 5) two very characteristic points become obvious: (i) HfO_2 precipitation within the SiHfCNO matrix is always related to a local nitrogen content below a threshold value which amounts to approximately 14 at% (mean), while (ii) HfO_2 precipitate growth occurs only within areas with local carbon content below a threshold value of 5 at% carbon. The latter finding is consistent with the rather sluggish coarsening of HfO_2 observed in a surface-near area monitored for the sample annealed for 3h (with a mean size of only 2.5 nm) which reveals a somewhat higher amount of carbon (11.3 at%, Table 5) than the threshold value with respect to coarsening (5 at%). A similar threshold value for pronounced coarsening of HfO_2 was monitored for the HfO_2/SiHfOC samples (approximately 6 at%, chapter 5.3).

We recall here that in the case of HfO_2/SiHfOC a pronounced drop in the local carbon content near surfaces was observed, which is consistent with (i) the continuous weight-loss of the samples monitored after annealing and (ii) TG-MS data [2] that indicate the escape of low-weight molecules during pyrolysis. Hence, the escape of low-weight C species is proposed as the underlying process resulting in the surface-near depletion in carbon monitored after annealing. Here, we also relate the depletion in carbon and nitrogen observed for the SiHfCNO samples to a loss of volatile C and N species during annealing.

Very interesting is also the comparison between the profiles for 1 h and those for longer annealing times (i.e.10, 50 and 200 h). What can be noted for the profiles after 1 h annealing is the parallel and rather steep decrease in both the overall local carbon and nitrogen content near the surface, but the rather uncorrelated relative decrease in carbon and nitrogen content monitored in the profiles after annealing for 10, 50, and 200 h, respectively, which indicates locally varying mobilities for the involved mobile species.

Comparing the profiles for both carbon and nitrogen after 1 and 200 h annealing, a decrease of the thickness of the depleted zone can be seen. It is assumed that this observation is a direct consequence of the formation of cristobalite on the internal surface of the sample annealed for 200 h. A reasonable qualitative assumption is that the outward diffusion of the (though unknown) mobile species through the cristobalite

layer is in fact slower than the effective diffusion of carbon and nitrogen species within the amorphous bulk, resulting in the observed steep carbon and nitrogen profiles at the cristobalite/amorphous SiHf(C,N)O interface shown in Figure 23 (d). This explanation is consistent with results from CO_2 sorption experiments [15] that show that the mobility of CO_2 (dissolved as a molecule) in quartz is by several orders of magnitude slower than in silica glasses. (The diffusivity of CO_2 in silica is $1*10^{-13}$ m^2/s (at 1095°C) [16]). On the other hand, the variation of the thickness of the depleted zones among the profiles for 1, 10, and 50 h annealing (see Figure 23) can be rationalized by varying onset times of cracking that determine the onset time of the subsequent degassing period during pyrolysis/annealing.

As already noted, in the sample annealed for 3 h (see Figure 33 in the Appendix), the measured amount by which the local nitrogen and carbon contents decrease near the investigated internal surface is somewhat smaller, as compared to the reference sample (1 h). This finding might be explained by early closure of the initially open pore channel at some instance during pyrolysis/annealing that could prevent this particular sample region from further depletion. This sample was thus excluded from further discussion of the coarsening process which is addressed further in the following chapter.

6.4 Diffusion of Hafnium

In order to estimate hafnium diffusivities from the measured HfO_2 particle sizes at various times t, the diffusion coefficient (D_{Hf}) on the basis of the theoretical kinetic equation for volume diffusion-controlled growth derived by Wagner (1961) [6] (eq. 4, chapter 4.2.3) was calculated, though this equation is strictly speaking only valid for the ideal limit of zero volume fraction of the precipitated phase. The temporal power-law exponent in the kinetic equation for volume diffusion-controlled coarsening is three [6]. A rate exponent of three was also reported in many empirical studies on coarsening microstructures comprising precipitates of spherical or plate-like habits [17].

HfO_2 particle volume fractions given in Table 7 were determined on numerous TEM images of HfO_2 precipitates for all samples, except for the sample annealed for 100 h (see chapter 6.6), with particular emphasis being placed on areas in vicinity to the HfO_2 depleted bulk regions (SiHf(C,N)O matrix) and within the coarsened outermost regions near internal surfaces (SiO_2 matrix). The particle volume fractions are

considered comparable among the two distinct areas of similar composition, except for the samples annealed for 3 (SiO_2 matrix) and 200 h (SiHf(C,N)O matrix). Hence, the initial local value of the particle volume fraction is preserved for all samples, the value depending on the local composition of the matrix, which supports the proposed coarsening of HfO_2. The calculated local mean value of the hafnia particle volume fraction for small and larger particles, respectively (3.5 vol% for surface-near regions, and 0.3 vol% for regions with a nitrogen content of approximately 14 at% nitrogen), was used for the calculation of the concentration of solved hafnia within the matrix with an assumed constant density of the HfSi(C,N)O matrix of 2.3 g/cm^3. This is a simplifying assumption, as the density of the matrix varied locally, owing to the local variation in chemical composition and local crystallization of the matrix. The error related to the density and hence to the calculated concentration of solute hafnium, c_{Hf}, is, however, considered insignificant, since it does not affect the order of magnitude of D_{Hf}, which linearly depends on c_{Hf} in equation 4 (chapter 4.2.3). The amount of HfO_2 solved in the matrix is determined from the amount by which the value of the total fraction of HfO_2 (chemical analysis, 5.6 vol%) differed from the mean local value of the HfO_2 particle fraction (TEM imaging, 3.5 vol% and 0.3 vol%, respectively). These values were converted into the local concentration of hafnium solved in the matrix, c_{Hf}, which amounts to 983.0 mol/m^3 for the fraction of the large particles observed in the SiO_2-rich matrix near surfaces, while c_{Hf} is 2504.8 mol/m^3 for the small precipitates in the HfSi(C,N)O matrix, respectively. For the sample annealed for 200 h, where regions near internal surfaces were predominantly constituted of cristobalite inheriting coarsened hafnia precipitates, c_{Hf} also was 983.0 mol/m^3 using the density of low-cristobalite (2.3 g/cm^3 [18, p. 156]). With the parameters given in chapter 4.2.3, the calculated values for D_{Hf} derived for the fraction of small HfO_2 particles are considered comparable being within the same order of magnitude (10^{-22} m²s^{-1}, Table 7). The value for the sample annealed for 10 h is only slightly higher (by a factor of approximately 2) than that for 50 and 200 h annealing, respectively. Therefore, it is concluded that volume diffusion-controlled coarsening is the active growth mechanism for the HfO_2 precipitates. For surface-near regions, the calculated values for D_{Hf} are about three orders of magnitude higher ($1.1*10^{-19}$ m^2/s for 10 h, $5.7*10^{-19}$ m^2/s for 50 h, and $2.1*10^{-19}$ m^2/s for 200 h, see Table 7), as compared to those for regions that contain small HfO_2 (10^{-22} m^2/s). The obtained Hf diffusivities for the SiHf(C,N)O matrix near internal surfaces are very

slow (10^{-22} m^2/s at 1300°C), but by one order of magnitude faster than Hf cation diffusivities in silicates ($ZrSiO_4$ [19] and within the same order of magnitude with the Si cation diffusivity in olivine [20] and Si diffusivity in amorphous SiBCN (at 1300°C) [21] (see also Table 4, chapter 5.5). Interesting is the comparison between the Hf diffusivities for the SiHfCNO (this chapter) and SiHfOC materials (cfr. chapter 5.5), the D_{Hf} values in the surface-near depleted regions of both materials differing systematically by about one order of magnitude for all annealing times (compare Table 7, this chapter, and Table 3, chapter 5.5). Apparently, a residual amount of nitrogen in the surface-near regions of the SiHfCNO samples is sufficient to affect hafnium diffusion, leading to a drop in D_{Hf} by one order of magnitude for these samples, as compared to D_{Hf} for surface-near regions of the HfO_2/SiHfOC material. A similar compositional dependence (the Hf diffusion coefficient decreases with nitrogen incorporation) was found by Ikarashi et al. (2006) [9].

Table 7: Mean HfO_2 particle radius (r), particle volume fraction (V), and Hf diffusion coefficient (D_{Hf}) calculated on the basis of the LSW-theory for two very characteristic local matrix compositions, i.e., (left) SiHf(C,N)O and (right) SiO_2.

	SiHf(C,N)O matrix			**SiO_2 matrix**		
time (h)	**r (nm)**	**V (%)**	**D_{Hf} (m^2/s)**	**r (nm)**	**V (%)**	**D_{Hf} (m^2/s)**
1*	0.85±0.19	0.32		2.62±0.53	4.19	
3#	1.02±0.22	0.19		1.26±0.28	1.62	
10	1.15±0.23	0.20	$7.4*10^{-22}$	3.52±0.91	3.34	$1.1*10^{-19}$
50	1.35±0.27	0.48	$2.8*10^{-22}$	9.11±5.28	2.97	$5.7*10^{-19}$
200	2.17±0.55	1.01	$3.6*10^{-22}$	10.78±3.25	3.46	$2.1*10^{-19}$

* The sample annealed for 1 h is the reference sample.
# The sample annealed for 3 h was excluded (see text).

Our results are also in agreement with results of Schmidt et al. (2005) [22] who found the highest (lowest) coarsening rate of SiC nanocrystals in a SiBCN ceramic with a carbon-rich (nitrogen-rich) SiBCN formulation, which was related to the higher (lower) volume diffusion coefficient of the rate-controlling though unknown species, derived from the different formulations on the basis of the LSW theory. Unfortunately, this study [22] gained no further insight into the probably different nanostructures among the different SiBCN materials. The hafnium diffusivity in SiHf(C,N)O is by about one

order of magnitude lower than the diffusivity of Si in Si-rich SiOC [23]. Beside the effect of nitrogen on hafnium diffusion in SiHf(C,N)O, the difference in the size among the tetravalent Hf^{4+} and Si^{4+} ions may also be responsible for the different diffusivities [19]. Moreover, different diffusion paths for silicon and hafnium among both materials might also be a reasonable explanation for the difference in the respective diffusivities of hafnium and silicon. Schmidt and coworkers determined tracer diffusivities for nitrogen, silicon, and carbon (a single value) [24], as well as for boron in phase separated amorphous SiBCN [25]. These authors found that the nitrogen and carbon tracer diffusivities and activation enthalpies determined were comparable to diffusion data in crystalline single-phase compounds reported in the literature, namely carbon diffusion in SiC (as compared to the ^{13}C tracer diffusion data) and nitrogen diffusion in Si_3N_4 (as compared to the ^{15}N tracer diffusion data), respectively [24]. It was therefore proposed, though still a hypothesis, that diffusional transport of nitrogen and carbon occurs within distinct and different percolation paths of the segregated phases present in the SiBCN material investigated, according to small angle neutron and x-ray scattering, namely within Si_3N_4 and SiC percolation networks, respectively [25]. In [25], analogous considerations were made for boron diffusion.

6.5 The Outer Surface

Apart from internal surfaces, the samples also reveal an outer surface layer that is rich in vitreous silica. The TEM image in Figure 24 shows a region within the outer surface layer of the sample annealed for 1 h that contains a homogeneous dispersion of HfO_2 precipitates hosted in an amorphous SiO_2-rich matrix. Form Figure 24 (a), approximately the same mean diameter of the hafnia precipitates (4.7 ± 1.1 (±1 σ) nm, n = 145) as compared with that for an internal surface (5 nm, see Figure 20 (a)) of the same sample is inferred, which is consistent with the observation that both outer and internal surface are pronouncedly depleted in nitrogen and carbon. It is interesting from a mineralogical point of view that a few euhedral larger crystals are also observed in this layer (see Figure 24 (b)), one of which was identified as hafnon ($HfSiO_4$) using selected area electron diffraction. The rather large crystals are located at the rim of a spherical inclusion of several hundreds of nanometer in diameter that contains pure vitreous SiO_2. However, this is not unusual since an as-pyrolyzed (1300°C) sample also revealed euhedral hafnon crystals embedded in a pure SiO_2

matrix of a spherical inclusion typically observed near surfaces of this sample (see SEM image in the inset in Figure 24 (b)). It is well known that hafnia and vitreous silica (or its crystalline polymorphs, i.e., cristobalite and quartz) in the solid state react at rather high temperatures (e.g., at 1550°C [26]) to a single compound, hafnon ($HfSiO_4$). Hafnon synthesis via chemical transport reactions [27] at even lower temperatures (1000°C) and sol–gel methods (in air) at temperatures between 1100 and 1400°C [28] is also possible. However, unravelling the mechanism that leads to the formation of hafnon in the SiHfCNO samples heat treated at 1300°C is beyond the scope of the present work.

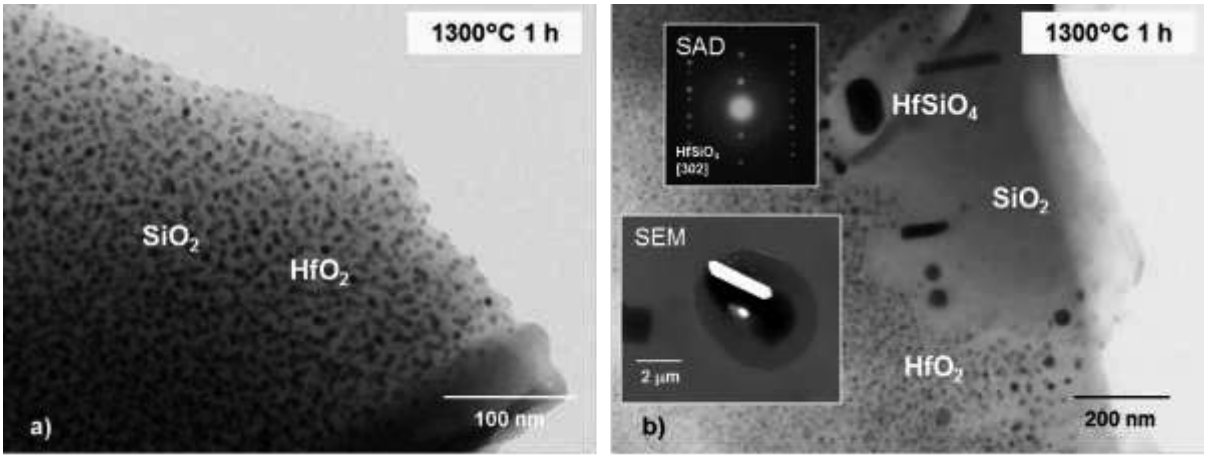

Figure 24: TEM bright-field images of the microstructure observed in the outer surface layer of the SiHfCNO sample annealed at 1300°C for 1 h. The outer layer is depleted in carbon and nitrogen, respectively, which is also evident by its transparency in the light microscope. Numerous precipitates of hafnia are shown. (b) A single hafnon crystal (see SAD inset in (b)) grown at the rim of a pure silica inclusion is shown. The SEM (BSE) image (inset in (b)) of a fracture surface of a SiHfCNO sample annealed at 1300°C shows a single euhedral hafnon crystal at the rim of a silica inclusion.

In Figure 25, backscattered scanning electron images of the silica-rich outer surface layer of the sample annealed for 1 h are shown revealing at higher magnification numerous silica droplets on the outer surface (see Figure 25 (b)). This pure silica phase on the surface may have been formed during the decomposition of the precursor during pyrolysis and may have condensed as droplets upon cooling, driven by surface tension (silica flows viscously at 1300°C [29]). However, whether the observed SiO_2 inclusions on the outer surface layer of the SiHfCNO samples (1300°C) sometimes inheriting hafnon crystals (see Figure 24 (b)) were related to such silica (melt) spheres is still unclear.

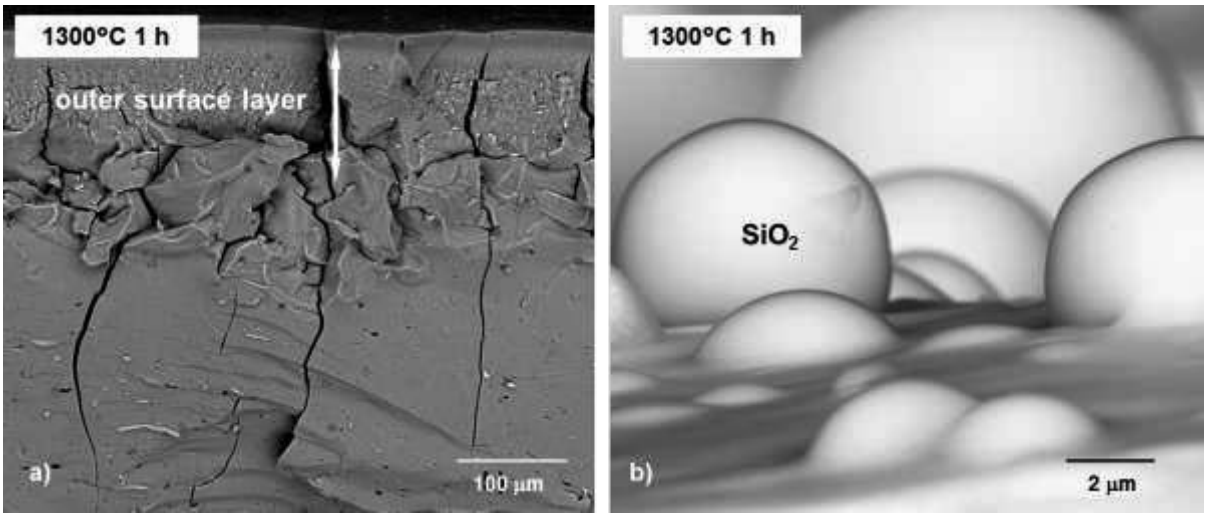

Figure 25: Backscattered scanning electron images of the outer surface layer of the sample annealed for 1 h at 1300°C. The sample reveals a SiO_2 enriched outer layer of approximately 60 µm depth (see also the corresponding TEM images shown in Figure 24).

6.6 Crystallization in the Closed System

In the following, special attention is given to the sample annealed for 100 h with a different microstructure near internal surfaces, as compared to the samples annealed for 1, 3, 10, 50, and 200 h. In the scanning electron image shown in Figure 26, micrometer-sized closed pores can be distinguished, while no indication for open pore channels or microcracks monitored for the other samples (1, 3, 10, 50, and 200 h) is seen. Such residual (closed) porosity has, however, also been observed in unmodified polymer-derived SiCN ceramics [30].

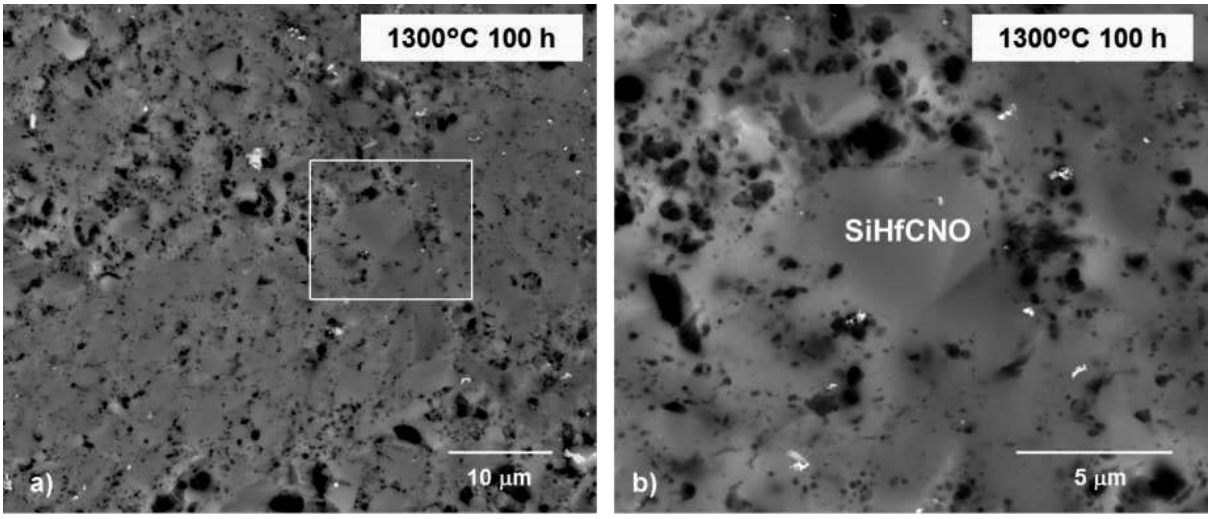

Figure 26: Backscatter scanning electron images of a fracture surface of the monolith annealed at 1300°C for 100 h. Note that the bulk microstructure of this sample is markedly different from that of the other SiHfCNO samples investigated in that this sample reveals a high fraction of voids apart from the homogeneous microstructure of the rather dense regions also observed for the other samples.

Apart from the local (closed) porosity, the central region of the monolith reveals a network of micrometer-sized particles that reveal a homogeneous dense microstructure.

TEM imaging is consistent with the SEM observation of a glass-like microstructure of the dense regions, as depicted in Figure 27. EDS analysis reveals a homogeneous dispersion of hafnium throughout the matrix that is composed of SiHfCNO. The high-resolution TEM image shown in Figure 27 (b) does not allow for an indication of the phase separation within the overall amorphous matrix, as indicated by the ^{29}Si NMR data of as-pyrolyzed samples (1100°C) [2].

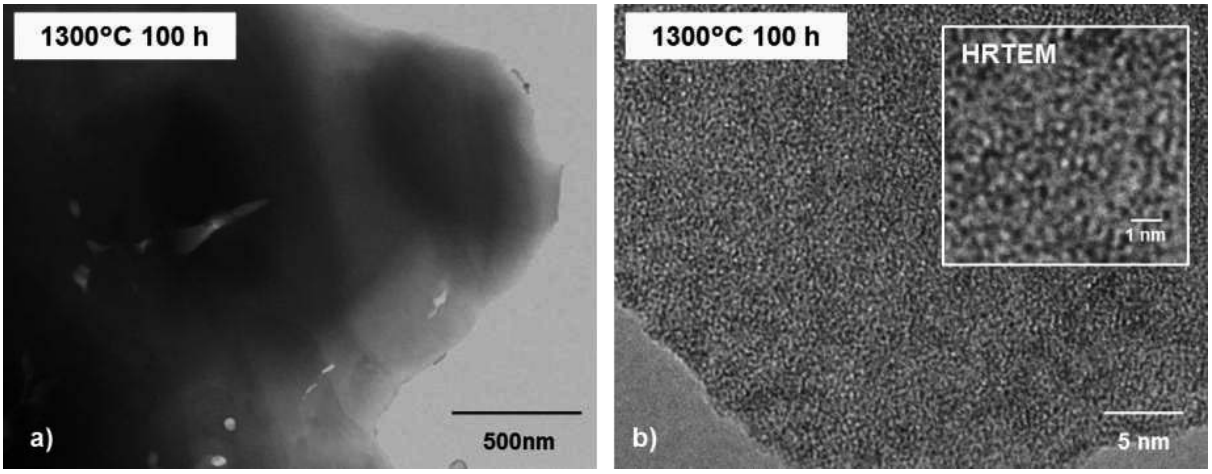

Figure 27: TEM bright-field image and (b) high-resolution TEM image of the overall amorphous microstructure of a rather dense region of the sample annealed for 100 h. As can be seen in the inset in (b), no evidence for a phase separated matrix is observed at high resolution.

However, the internal surfaces of the sample are coated with a matrix that reveals a different contrast as compared to the homogeneous dense regions, as depicted in the TEM bright-field images given in Figure 28. Coalescence between dense regions and the coating onto the internal surfaces is observed, although the coating reveals a high degree of crystallization. The contrast difference between coating and dense regions is attributed to the high degree of crystallization and the residual porosity due to the density change accompanying crystallization (see Figure 29 (a)). Apart from β-Si_3N_4 crystallites, a small fraction of a residual amorphous phase is also observed in the crystallized coating (see Figure 29 (b)). Preliminary EDX analysis did not allow to unequivocally relate the high degree of crystallization to any chemical variation.

Recent ^{29}Si NMR studies of as-pyrolyzed SiHfCNO monoliths derived from Hf-alkoxide modified HTT indicated predominantly a N-rich environment of silicon after pyrolysis at 1100°C [2], which could lead to the nucleation-crystallization of Si_3N_4.

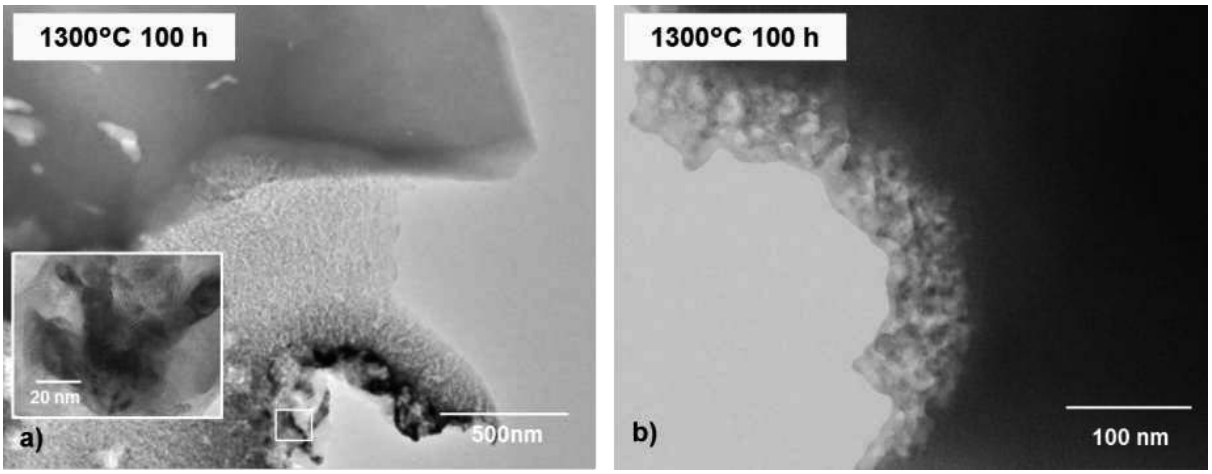

Figure 28: TEM bright-field images of the microstructure of the sample annealed for 100 h. The internal surfaces of dense regions (pore walls) are coated with a partly crystallized matrix. Coalescence between dense regions and coating is observed. Beside small crystallites in the matrix of the coating, a small fraction of whiskers grown at the rims of the coating is also observed (inset in (a)).

This indication for a phase separation to predominantly Si-N environments, beside a minor fraction of Si-O enriched environments, was associated with the formation of hafnia enriched regions in the amorphous matrix [2]. Please note that TEM confirmed the presence of hafnia only for regions near internal surfaces (see chapter 6.1 and 6.2). On the other hand, the high fraction of N-rich silicon environments, as indicated by NMR [2], is in agreement with the high degree of Si_3N_4 crystallization observed in the sample annealed for 100 h. One main open question is, however, why only the matrix near the internal surfaces of this sample reveals a high degree of Si_3N_4 crystallization, while the dense regions themselves remain amorphous.

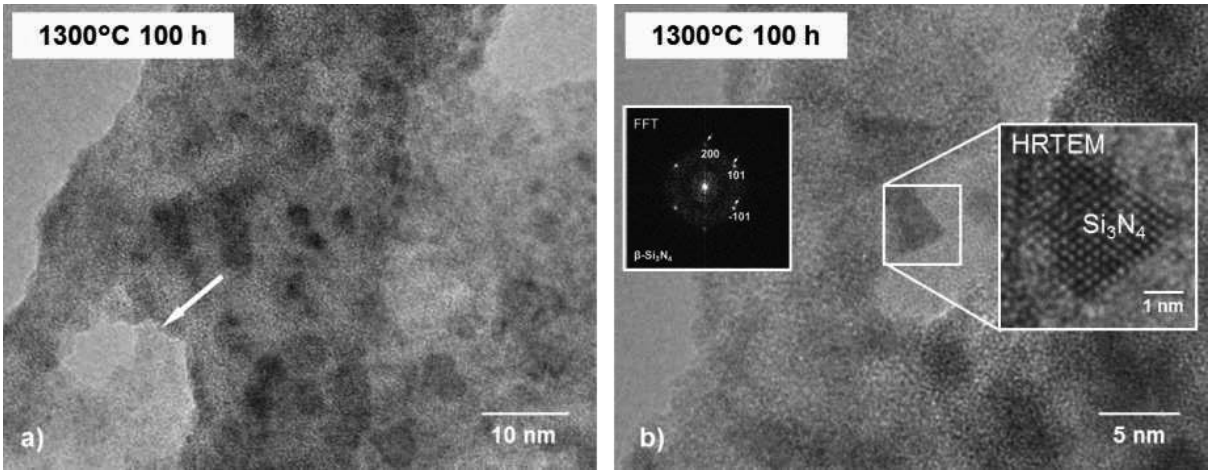

Figure 29: High-resolution TEM images of an area within the coating onto an internal surface of the sample showing nanoporosity (arrow) associated with a high degree of crystallization. In (b), a high-resolution TEM image of the boxed area of one facetted crystal identified as β-Si_3N_4 is shown together with the corresponding Fast Fourier Transform (FFT).

With respect to internal surfaces, it is well known that the high-temperature stability of SiCN ceramics in the amorphous state (above 1400°C) strongly depends on the residual porosity, because the phase separation-decomposition-crystallization process (carbothermal reduction of Si_3N_4) in the SiCN matrix is promoted by the escape of nitrogen [31]. However, the central region of the sample investigated here is considered as a closed system, since no depletion in nitrogen near the internal surfaces (pores) was observed, but instead local Si_3N_4 crystallization was observed in the interior of the pores.

6.7 References

1 B. Papendorf, K. Nonnenmacher, E. Ionescu, H.-J. Kleebe, and R. Riedel (2011). Strong influence of polymer architecture on the microstructural evolution of hafnium-alkoxide-modified silazanes upon ceramization. *Small*, 7(7), 970–978.

2 E. Ionescu, B. Papendorf, H.-J. Kleebe, H. Breitzke, K. Nonnenmacher, G. Buntkowsky, and R. Riedel (2012). Phase separation of a hafnium alkoxide-modified polysilazane upon polymer-to-ceramic transformation – A case study. *J. Eur. Ceram. Soc.*, 32(9), 1873–1881.

3 K. Terauds, D. B. Marshall, and R. Raj (2013). Oxidation of polymer-derived HfSiCNO up to 1600°C. *J. Am. Ceram. Soc.*, 96(4), 1278-1284.

4 R. Sujith and R. Kumar (2013). Indentation response of pulsed electric current sintered polymer derived HfO_2/Si–C–N(O) nanocomposites. *Ceram. Int.*, 39(8), 9743-9747.

5 M. Lifshitz and V. V. Slyozov (1961). The kinetics of precipitation from supersaturated solid solutions. *J. Phys. Chem. Solids*, 19(1-2), 35-50.

6 C. Wagner (1961). Theorie der Alterung von Niederschlägen durch Umlösen (Ostwald-Reifung). *Z. Elektrochem.*, 65, 581-591.

7 H.-J. Kleebe, K. Nonnenmacher, E. Ionescu, and R. Riedel (2012). Decomposition-coarsening model of SiOC/HfO_2 ceramic nanocomposites upon isothermal anneal at 1300 °C. *J. Am. Ceram. Soc.*, 95(7), 2290-2297.

8 B. Papendorf (2012). *Keramische Nanokomposite auf Basis von SiOC/HfO_2 und SiCN/HfO_2: Herstellung und Untersuchungen zum Hochtemperaturverhalten.* (Unpublished doctoral dissertation.) Technische Universität Darmstadt, Darmstadt, Germany.

[9] N. Ikarashi, K. Watanabe, K. Masuzaki, T. Nakagawa, and M. Miyamura (2006). The influence of incorporated nitrogen on the thermal stability of amorphous HfO_2 and Hf silicate. *J. Appl. Phys.*, 100, 063507-1-5.

[10] K. Terauds and R. Raj (2013). Limits to the stability of the amorphous nature of polymer derived HfSiCNO compounds. *J. Am. Ceram. Soc.*, 96(7), 2117-2123.

[11] M. N. Rahaman (2007). *Sintering of ceramics*. Boca Raton, FL: CRC Press.

[12] A. J. Ardell (1972). The effect of volume fraction on particle coarsening: Theoretical considerations. *Acta Metall. Mater.*, 20(1), 61-71.

[13] R. L. Withers, J. G. Thompson, and T. R. Welberry (1989). The structure and microstructure of α-cristobalite and its relationship to β-cristobalite. *Phys. Chem. Min.*, 16(6), 517-523.

[14] R. Dohmen and R. Milke (2010). Diffusion in polycrystalline materials: Grain boundaries, mathematical models, and experimental data. In Y. Zhang and D. J. Cherniak (Eds.), *Diffusion in Minerals and Melts*, (pp. 921-970). Chantilly, VA: The Mineralogical Society of America.

[15] H. Behrens (2010). Noble gas diffusion in silicate glasses and melts. In Y. Zhang and D. J. Cherniak (Eds.), *Diffusion in minerals and melts* (pp. 227-267). Chantilly, VA: The Mineralogical Society of America.

[16] H. Behrens (2010). Ar, CO_2 and H_2O diffusion in silica glasses at 2 kbar pressure. *Chem. Geol.*, 272, 40-48.

[17] R. D. Doherty (1982). Role of interfaces in kinetics of internal shape changes. *Met. Sci.*, 16(1), 1-14.

[18] M. Okrusch and S. Matthes (2009). *Mineralogie* (8th ed.). Berlin, Germany: Springer.

[19] D. J. Cherniak, J. M. Hanchar, and E. B. Watson (1997). Diffusion of tetravalent cations in zircon. *Contrib. Mineral. Petrol.*, 127, 383-390.

[20] R. Dohmen, S. Chakraborty, and H. W. Becker (2002). Si and O diffusion in olivine and implications for characterizing plastic flow in the mantle. *Geophys. Res. Lett.*, 29(21), 26-1–26-4.

[21] H. Schmidt, G. Borchardt, S. Weber, H. Scherrer, H. Baumann, A. Müller, and J. Bill (2002). Comparison of ^{30}Si diffusion in amorphous SiCN and SiBCN precursor-derived ceramics. *J. Non-Cryst. Sol.*, 298(2-3), 232-240.

[22] H. Schmidt, W. Gruber, G. Borchardt, P. Gerstel, A. Müller, and N. Bunjes (2005). Coarsening of nano-crystalline SiC in amorphous Si-B-C-N. *J. Eur. Ceram. Soc.*, 25(2-3), 227-231.

[23] G. Gregori, H.-J. Kleebe, D. W. Readey, and G. D. Sorarù (2006). Energy-filtered TEM study of Ostwald ripening of Si nanocrystals in a SiOC glass. *J. Am. Ceram. Soc.*, 89(5), 1699-1703.

[24] H. Schmidt, G. Borchardt, H. Baumann, S. Weber, S. Scherrer, A. Müller, and J. Bill (2001). Tracer self diffusion studies in amorphous Si-(B)-C-N ceramics using ion implantation and SIMS. *Defect. Diffus. Forum*, 194-199, 941-946.

[25] H. Schmidt, G. Borchardt, O. Kaitasov, and B. Lesage (2007). Atomic diffusion of boron and other constituents in amorphous SiBCN. *J. Non-Cryst. Sol.*, 353(52-54), 4801-4805.

[26] C. E. Curtis, L. M. Doney, and J. R. Johnson (1954). Some properties of hafnium oxide, hafnium silicate, calcium hafnate and hafnium carbide. *J. Am. Ceram. Soc.*, 37(10), 458-465.

[27] J. Fuhrmann and J. Pickardt (1986). Bildung von $HfSiO_4$-Einkristallen durch chemische Transportreaktion. *Z. Anorg. Allg. Chem.*, 532(1), 171–174.

[28] Y. Kanno (1993). Effect of dopants on the formation of hafnon via sol–gel route. *J. Mater. Sci. Lett.*, 12(23), 1807–1809.

[29] L. An, R. Riedel, C. Konetschny, H.-J. Kleebe, and R. Raj (1998). Newtonian viscosity of amorphous silicon carbonitride at high temperature (1090°C-1280°C). *J. Am. Ceram. Soc*., 81(5), 1349-1352.

[30] H.-J. Kleebe (1998). Microstructure and stability of polymer-derived ceramics: the Si-C-N system. *Phys. Stat. Sol. A*, 166(1), 297-312.

[31] H.-J. Kleebe, D. Suttor, H. Müller, and G. Ziegler (1998). Decomposition-crystallization of polymer-derived Si-C-N ceramics. *J. Am. Ceram. Soc.*, 81(11), 2971-2977.

7 Conclusion and Outlook

Conventional transmission electron microscopy (CTEM) in conjunction with energy-dispersive X-ray spectrometry (EDS) allowed for a detailed investigation of the microstructure of polymer-derived hafnia-modified silicon oxycarbide (HfO_2/SiHfOC) and hafnia-modified silicon oxycarbonitride (HfO_2/SiHfCNO) ceramic nanocomposites with a focus on the rather unexpected, locally enhanced coarsening of HfO_2 precipitates. This enhanced particle coarsening was observed in both materials typically in areas close to outer and internal surfaces (near microcracks and pore channels in the interior of the samples) upon isothermal annealing. Whereas integral analytical techniques such as chemical analysis and quantitative ^{29}Si solid-state NMR analysis are established routines in this field, analytical TEM namely EDS provides complementary information with regard to the local intrinsic composition, revealing a characteristic and steep gradient in the light elements nitrogen and/or carbon within surface-near areas investigated. In addition, from TEM-EDS analysis a characteristic threshold value for enhanced HfO_2 coarsening by volume diffusion could be deduced. HfO_2 precipitate growth proceeds without change of the overall precipitate volume fraction but with broadening of the size distributions with time and can be characterized as a volume diffusion-controlled Ostwald ripening. The diffusivity of hafnium in the matrix was calculated based on the LSW theory of Ostwald ripening. The calculated values for the hafnium diffusivity are consistent with literature data for silicates, covalent crystalline and amorphous solids, as well as other PDC systems. Coarsening proceeded at a higher rate in close proximity to internal surfaces, as compared to regions closer towards the bulk, and consequently the hafnium diffusivity was by three orders of magnitude higher ($7*10^{-18}$ m^2s^{-1} at 1300°C, 200 h, for HfO_2/SiHfOC; $2*10^{-19}$ m^2s^{-1} at 1300°C, 200 h, for HfO_2/SiHfCNO), as compared to the value derived from regions closer towards the bulk ($2*10^{-21}$ m^2s^{-1} at 1300°C, 200 h, for HfO_2/SiHfOC; $4*10^{-22}$ m^2s^{-1} at 1300°C, 200 h, for HfO_2/SiHfCNO), which was correlated with a variation in the local intrinsic nitrogen and/or carbon content. Thus, the local composition was investigated further utilizing EDS analysis in the TEM allowing for a correlation between composition and average HfO_2 particle size.

Modelling carbon diffusion profiles using an analytical method provided a better understanding of carbon transport in surface-near areas and yielded estimative values for the carbon diffusivity (between $5*10^{-18}$ m^2/s and $3*10^{-19}$ m^2/s for the

samples annealed for 100 and 10 h, respectively; the value obtained for the sample annealed for 1 h being much higher, $3*10^{-16}$ m^2/s). As carbon diffusion stagnates in surface-near areas after surface crystallization of cristobalite, the calculated carbon diffusivity decreased with increasing annealing time.

The samples investigated are considered as open systems owing to the high amount of open pores and microcracks within the interior of the samples. The occurrence of a carbon-(nitrogen-)depleted zone in these samples can be explained by the decomposition (organic-inorganic conversion) of the polymeric material during pyrolysis and degassing of volatile decomposition products via open pores/microcracks, as supported by chemical analysis via mass spectrometry. This finding supports the view that degassing during high-temperature annealing is driven by the initial concentration gradients of carbon (and nitrogen) in the PDC matrix in the surface-near regions which promotes diffusion of carbon and nitrogen towards the depleted areas. The EDS data showed that integral chemical analysis can be questionable with respect to the quantification of carbon and nitrogen for monolithic samples that contain open pores/microcracks, since the extent of depletion that corresponds to this weight loss near internal and outer surfaces cannot be quantified by integral measurements. Hence integral analytical techniques may provide underestimated overall bulk amounts for these elements.

No clear evidence for local HfO_2 precipitation, even not upon prolonged annealing for 200 h, was found in the bulk volume of the annealed HfO_2/SiHfCNO material showing higher local nitrogen contents, as compared to the investigated surface-near regions. The implied hindrance to precipitation of HfO_2 in the SiHfCNO matrix is seen to be a consequence of the intrinsic amount of nitrogen since the ability of hafnium to diffuse through the SiHfCNO matrix is diminished. Therefore, it can be concluded that the initial goal to produce homogeneous polymer-derived HfO_2/SiCN-based ceramic nanocomposites is not achieved. Furthermore, it could be shown here for the first time that, as long as regions near outer and internal surfaces are considered, the annealed SiHfCNO material reveals a similar microstructure as the annealed HfO_2/SiHfOC material investigated, owing to the simultaneous depletion in carbon and nitrogen towards the internal surfaces in close proximity to microcracks and pore channels. A compositional variation for the light elements carbon and nitrogen in the HfO_2/SiHfCNO samples was, however, expected, since the samples investigated can

also be considered as open systems due to the presence of internal microcracks and pore channels.

Close to the surface, the hafnium volume diffusivity is about one order of magnitude lower ($2*10^{-19}$ m^2s^{-1} at 1300°C, 200 h) than the value for the HfO_2/SiHfOC material. This difference in the diffusion coefficient is attributed to the presence of additional residual nitrogen within the surface-near matrix in the HfO_2/SiHfCNO material, not present in the HfO_2/SiHfOC material, affecting the diffusion of hafnium.

Both systems investigated show stagnation of the outward diffusion of carbon and nitrogen after the onset of cristobalite surface crystallization.

The observed local compositional variation related to open porosity (microcracks) is not restricted to the alkoxide-modified materials studied here and has to be taken into account, in particular, when applications at high temperatures are envisioned, especially as thin films, such as thermal or environmental barrier coatings (TBC/EBC), since surface-near compositional variations certainly will influence the overall material performance in oxidation and corrosion environments as well as during mechanical testing. With regard to coating applications, future work may address a quantitative description of the pyrolytic decomposition and the related carbon and nitrogen mobility in thin ceramic coatings, as well as strategies to reduce outward diffusion of carbon and nitrogen.

8 Appendix

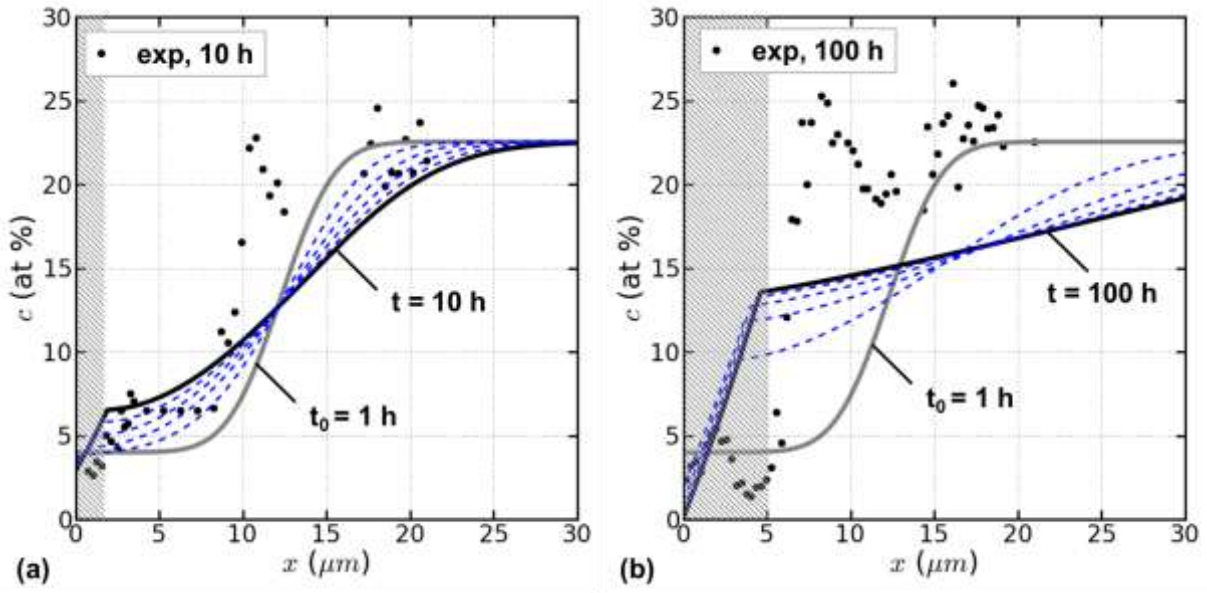

Figure 30: Numerical solutions for carbon profiles of annealed SiHfOC samples according to eq. 6 (chapter 4.2.4) for annealing times, t, between (a) 1 h - 10 h and (b) 50 h - 100 h. The concentration profile measured after 1 h (t_0) used as initial function is also shown (solid gray line). The shaded region to the left in both graphs indicates the thickness of the cristobalite layer taken into account in terms of D(x), the spatially dependent diffusion coefficient of carbon. The experimental data after (a) 10 h and (b) 100 h annealing, as measured by EDS/TEM, are also given for comparison.

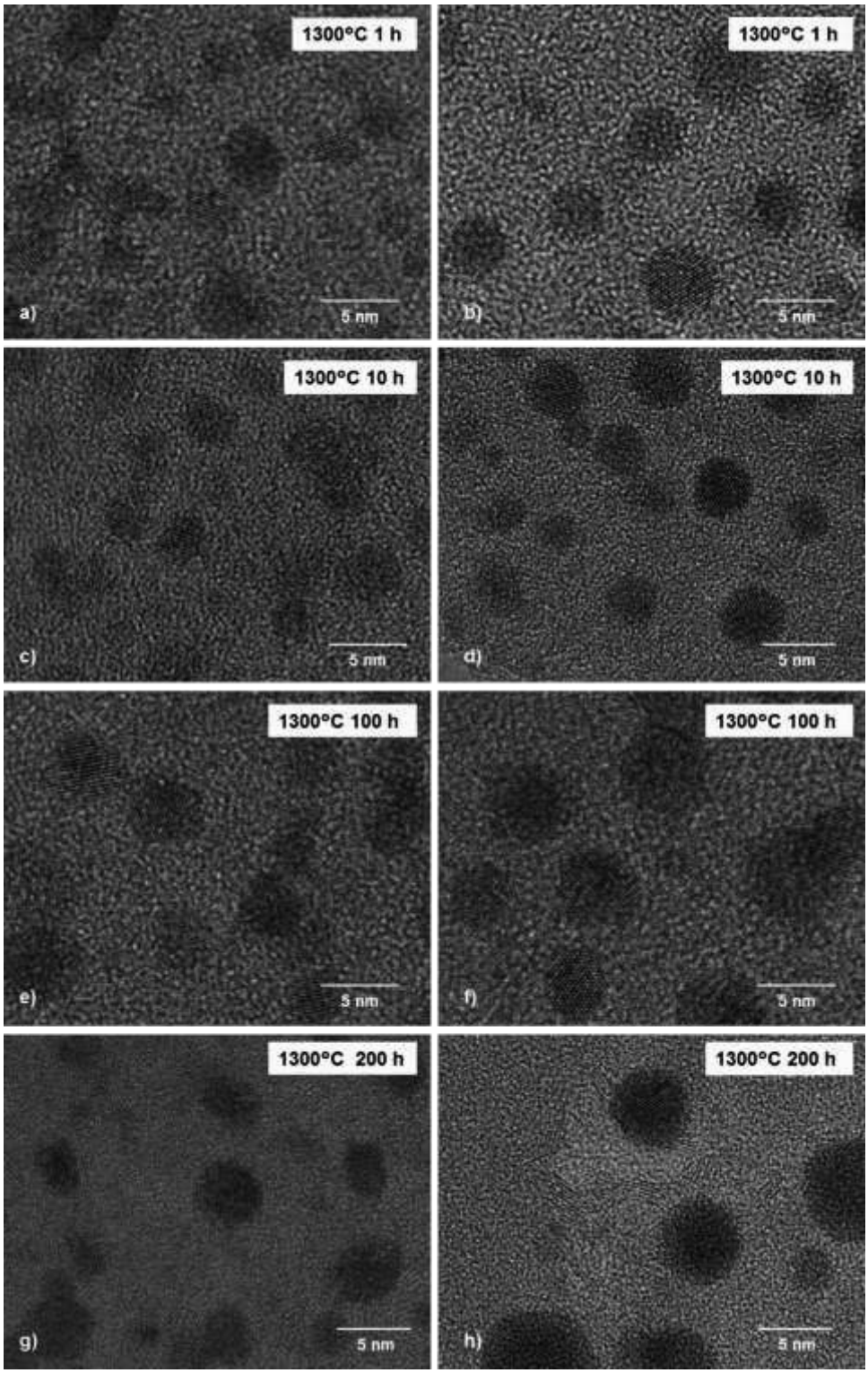

Figure 31: High-resolution TEM (HRTEM) images of HfO_2 crystallites in (a), (c), (e) and (g) corresponding to bulk regions of the annealed SiHfOC samples (1300°C) with the annealing times indicated in the upper right corners. (b), (d), (f), and (h) show HRTEM images of HfO_2 particles in areas corresponding to the inflection point, x_0, indicated in the corresponding carbon profile (see Figure 14). At x_0, the local carbon content decreases to approximately half the local amount measured in the bulk. For each annealed sample, a slight coarsening of the HfO_2 precipitates is observed in the right images relative to bulk areas, owing to a somewhat faster volume diffusion of hafnium in the matrix, merely depending on the local carbon content. The major fraction of carbon is present as a turbostratic graphite like phase dispersed in the matrix.

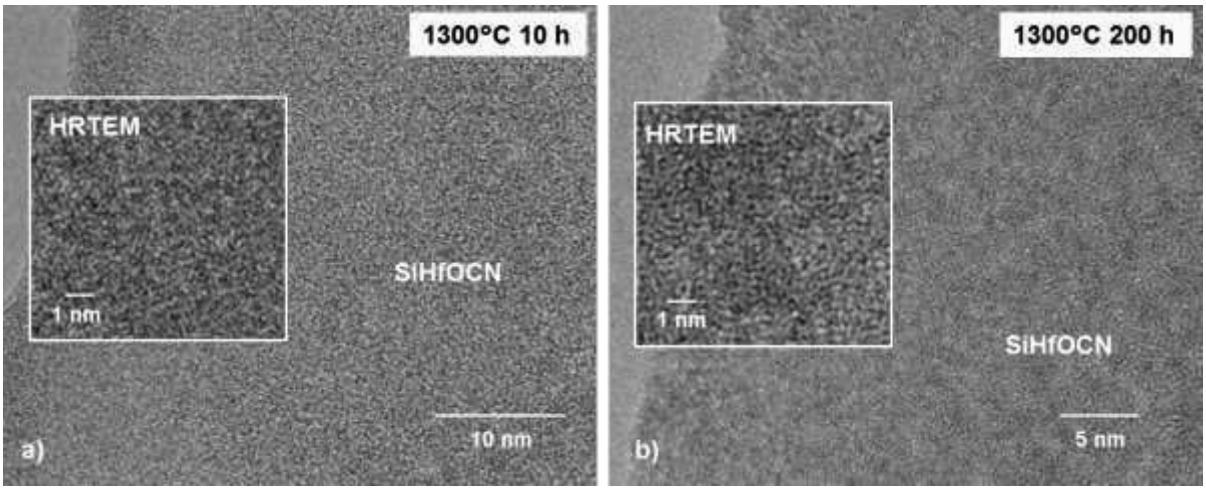

Figure 32: High-resolution TEM images of HfO_2/SiHfCNO samples annealed for (a) 10 h and (b) 200 h at 1300°C. At all stages of isothermal annealing, the amorphous nature of the bulk of the samples is preserved.

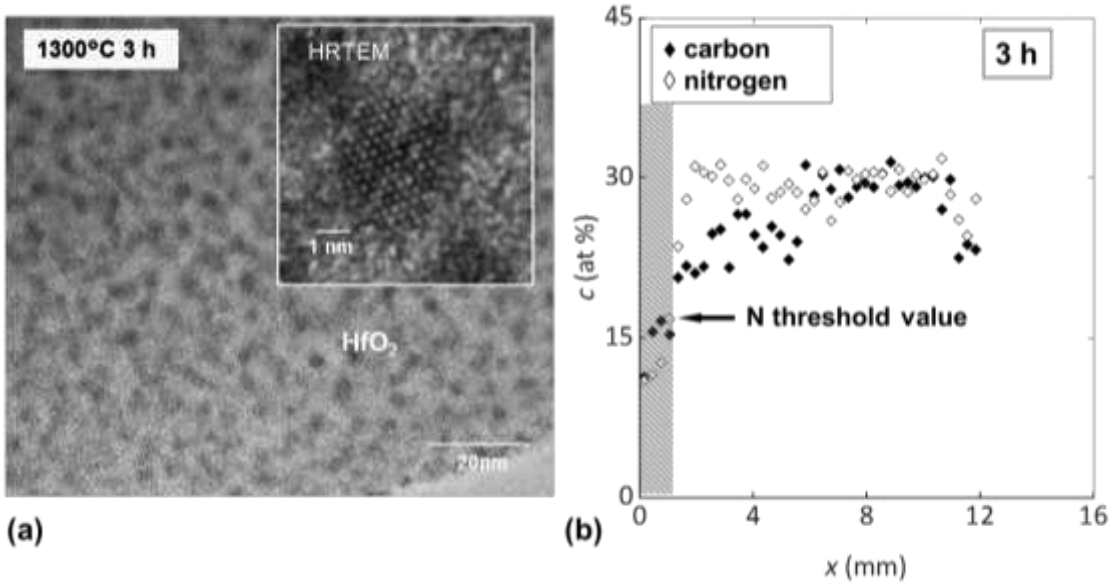

Figure 33: (a) High-resolution TEM image of an area in close proximity to an internal surface (microcrack) of the HfO_2/SiHfCNO sample annealed for 3 h at 1300°C. A homogeneous HfO_2 dispersion is observed in close proximity to the surface, as long as the local nitrogen content is below the threshold value with respect to HfO_2 precipitation (at appr.16 at%, marked with arrow in the corresponding nitrogen profile shown in (b)). The precipitates are monosized (mean of the particle diameter: 2.5 nm) in the area shown in (a), owing to the rather slow volume diffusion of hafnium in the matrix, which merely depends on the residual amount of carbon and nitrogen in the matrix; therefore, in (b), the corresponding carbon and nitrogen profiles measured by TEM-EDS are depicted.

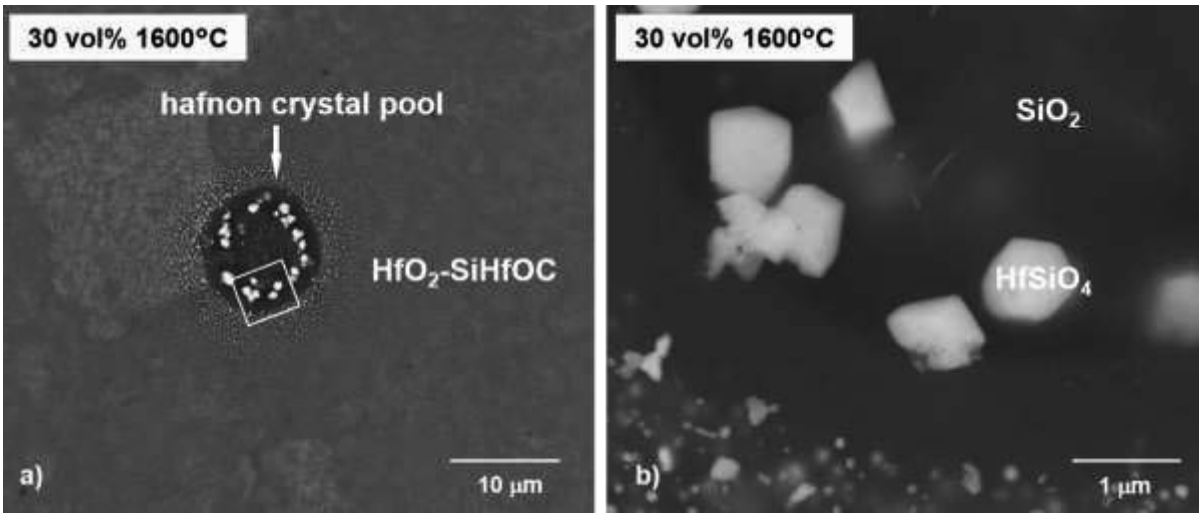

Figure 34: Backscatter scanning electron images of a fracture surface of a monolithic HfO_2/SiHfOC sample annealed at 1600°C for 5 h under argon. (a) Apart from a rather homogeneous bulk microstructure (HfO_2 nanocrystals are hardly discernable at this magnification), a SiO_2-rich spherical inclusion inheriting relatively large hafnon crystals is shown. (b) Hafnon crystals are well facetted exhibiting an idiomorphic habit toward the center of the SiO_2 inclusion.

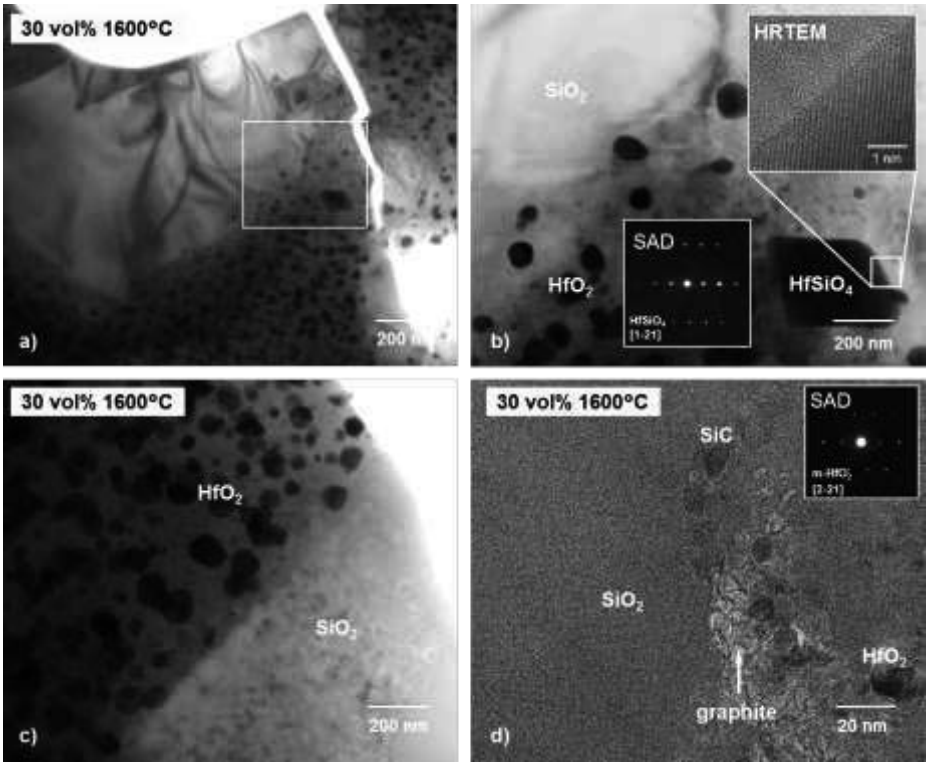

Figure 35: TEM bright-field images (a-c) of a region adjacent to a crystallized SiO_2 inclusion within the bulk of a SiHfOC sample annealed at 1600°C (5 h, under argon). A single hafnon crystal is observed at the rim of the inclusion. In (b), a magnified image of the single euhedral $HfSiO_4$ crystal observed in the boxed region in (a) is shown, as well as a high-resolution TEM image of the $HfSiO_4/SiO_2$ interface and a SAD pattern taken from the $HfSiO_4$ crystal (insets). In (c), an area of the sharp interface between the SiO_2 inclusion and the SiHfOC matrix hosting HfO_2 precipitates is shown. (d) Turbostratic carbon segregates at the SiO_2 grain boundary. Turbostratic carbon is thought to hinder the solid state reaction between SiO_2 and HfO_2 to $HfSiO_4$. Instead, carbothermal reduction of SiO_2 results in an extended crystallization of SiC, embedded in a carbon-rich amorphous residual phase.

Acknowledgements

My gratitude is expressed to many people at the TU Darmstadt; to Prof. Dr. Hans-Joachim Kleebe for his profound and compelling scientific advice, mentoring and trust, to Dr. Margarete Schloßer for her stimulating advice and encouragement, to Mathis Müller and Dr. Stefan Lauterbach for hands-on instruction at the TEM lab, to Prof. Dr. Ralf Riedel and his colleagues Dr. Emanuel Ionescu and Dr. Benjamin Papendorf for sample preparation and an successful collaboration, to Stefania Hapis, Marina Zakhozheva, Dr. Horst Purwin, and Dr. Stefanie Schultheiß, for an enjoyable and congenial company and for practical support, to Prof. Dr. Stefan Weinbruch for making my work at the SEM lab possible and for his contributing discussion, to Thomas Dirsch and Prof. Dr. Martin Ebert for hands-on instruction at the SEM lab, to Dr. Jochen Rohrer, a welcoming and thorough researcher from the working group of Prof. Dr. Karsten Albe at the Materials Modelling Division, to Janith Loewen from the Language Resource Center for enjoyable English lessons, to Angelika Willführ and Astrid Zilz for support in the office, to Petra Kraft for support in the library, to Dr. Hermann Nonnenmacher for proofreading and unreserved practical support.

Curriculum Vitae

Zur Person

Name	Katharina Nonnenmacher
Geburtsdatum/ -ort	16. April 1981, Berlin
Nationalität	Deutsch

Bildungsweg

2002 – 2005	Universität Leipzig Bachelorstudium Chemie an der Fakultät für Chemie und Mineralogie
03/2006	Bachelor of Science (Note: 2,1)
2005 – 2008	Universität Leipzig Masterstudium: Mineralogie und Materialwissenschaft an der Fakultät für Chemie und Mineralogie
12/2008	Master of Science (Note: 1,6) Masterarbeit am Leibniz-Institut für Oberflächenmodifizierung, Leipzig „Abscheidung photoaktiver Titanoxid-Dünnschichten durch Metall-Plasma-Ionen-Immersions-Implantation“
2009 – 2012	Technische Universität Darmstadt Promotionsstudium am Lehrstuhl für Geomaterialwissenschaft

Publikationsliste

K. Nonnenmacher, H.-J. Kleebe, J. Rohrer, E. Ionescu, and R. Riedel (2013). Carbon mobility in SiOC/HfO_2 ceramic nanocomposites. *J. Am. Ceram. Soc.*, 96(7), 2058–2060.

E. Ionescu, B. Papendorf, H.-J. Kleebe, H. Breitzke, K. Nonnenmacher, G. Buntkowsky, and R. Riedel (2012). Phase separation of a hafnium alkoxide-modified polysilazane upon polymer-to-ceramic transformation – a case study. *J. Eur. Ceram. Soc.*, 32(9), 1873–1881.

H.-J. Kleebe, K. Nonnenmacher, E. Ionescu, and R. Riedel (2012). Decomposition-coarsening model of SiOC/HfO_2 ceramic nanocomposites upon isothermal anneal at 1300 °C. *J. Am. Ceram. Soc.*, 95(7), 2290–2297.

B. Papendorf, K. Nonnenmacher, E. Ionescu, H.-J. Kleebe, and R. Riedel (2011). Strong influence of polymer architecture on the microstructural evolution of hafnium-alkoxide-modified silazanes upon ceramization. *Small*, 7(7), 970–978.